

To appear in *The Astrophysical Journal*

Dust Masses, PAH Abundances, and Starlight Intensities in the SINGS Galaxy Sample

B. T. Draine¹, D. A. Dale², G. Bendo³, K. D. Gordon⁴, J. D. T. Smith⁴, L. Armus⁵,
C. W. Engelbracht⁴, G. Helou⁶, R. C. Kennicutt^{4,7}, A. Li⁸, H. Roussel⁹, F. Walter⁹, D. Calzetti¹⁰,
J. Moustakas^{4,11}, E. J. Murphy¹², G. H. Rieke⁴, C. Bot⁶, D. J. Hollenbach¹³, K. Sheth⁶, and
H. I. Teplitz⁵

ABSTRACT

Physical dust models are presented for 65 galaxies in the SINGS survey that are strongly detected in the four IRAC bands and three MIPS bands. For each galaxy we estimate (1) the total dust mass, (2) the fraction of the dust mass contributed by PAHs, and (3) the intensity of the starlight heating the dust grains. We find that spiral galaxies have dust properties resembling the dust in the local region of the Milky Way, with similar dust-to-gas ratio, and similar PAH abundance. The observed SEDs, including galaxies with SCUBA photometry, can be reproduced by dust models that do not require “cold” ($T \lesssim 10$ K) dust.

The dust-to-gas ratio is observed to be dependent on metallicity. In the interstellar media of galaxies with $A_O \equiv 12 + \log_{10}(\text{O}/\text{H}) > 8.1$, grains contain a substantial

¹Princeton University Observatory, Peyton Hall, Princeton, NJ 08544-1001; draine@astro.princeton.edu

²Dept. of Physics & Astronomy, University of Wyoming, Laramie, WY 82071; ddale@uwyo.edu

³Astrophysics Group, Imperial College, Blackett Laboratory, Prince Consort Road, London SW7 2AZ, UK; g.bendo@imperial.ac.uk

⁴Steward Observatory, University of Arizona, Tucson, AZ 85721; kgordon@as.arizona.edu, cengelbracht@as.arizona.edu, jdsmith@as.arizona.edu

⁵Spitzer Science Center, MS 220-6, Caltech, Pasadena CA 91125; lee@ipac.caltech.edu, hit@ipac.caltech.edu

⁶Caltech, MC 314-6, Pasadena, CA 91125; gxh@ipac.caltech.edu, bot@caltech.edu

⁷Institute of Astronomy, University of Cambridge, Madingley Road, Cambridge CB3 0HA, UK; robk@ast.cam.ac.uk

⁸Department of Physics & Astronomy, University of Missouri, Columbia, MO 65211; LiA@missouri.edu

⁹Max-Planck-Institut für Astronomie, Königstuhl 17, D-69117, Heidelberg, Germany; roussel@mpia-hd.mpg.de, walter@mpia.de

¹⁰Space Telescope Science Institute, 3700 San Martin Drive, Baltimore, MD 21218; calzetti@stsci.edu

¹¹Dept. of Physics, New York University, 4 Washington Place, New York, NY 10003; john.moustakas@nyu.edu

¹²Dept. of Astronomy, Yale University, P.O. Box 208101, New Haven, CT 06520-8101; murphy@astro.yale.edu

¹³NASA/Ames Research Center, MS 256-6, Moffett Field, CA 94035; hollenba@ism.arc.nasa.gov

fraction of interstellar Mg, Si and Fe. Galaxies with $A_O < 8.1$ and extended H I envelopes in some cases appear to have global dust-to-gas ratios that are low for their measured oxygen abundance, but the dust-to-gas ratio *in the regions where infrared emission is detected* generally appears to be consistent with a substantial fraction of interstellar Mg, Si, and Fe being contained in dust. The PAH index q_{PAH} – the fraction of the dust mass in the form of PAHs – correlates with metallicity. The nine galaxies in our sample with $A_O < 8.1$ have a median $q_{\text{PAH}} = 1.0\%$, whereas galaxies with $A_O > 8.1$ have a median $q_{\text{PAH}} = 3.55\%$. The derived dust masses favor a value $X_{\text{CO}} \approx 4 \times 10^{20} \text{ cm}^{-2} (\text{K km s}^{-1})^{-1}$ for the CO to H_2 conversion factor. Except for some starbursting systems (Mrk 33, Tolo 89, NGC 3049), dust in the diffuse ISM dominates the IR power.

Subject headings: ISM: dust, extinction — ISM: general — galaxies: abundances — galaxies: general — galaxies: ISM — infrared: galaxies

1. Introduction

Interstellar dust affects the appearance of galaxies, by attenuating short wavelength radiation from stars and ionized gas, and contributing infrared (IR), far-infrared (FIR), submm, mm, and microwave emission [for a recent review, see Draine (2003)]. Dust also is an important agent in the fluid dynamics, chemistry, heating, cooling, and even ionization balance in some interstellar regions, with a major role in the process of star formation. Despite the importance of dust, determination of the physical properties of interstellar dust grains has been a challenging task – even the overall amount of dust in other galaxies has often been very uncertain.

The SINGS galaxy sample (Kennicutt et al. 2003) comprises 75 galaxies with a wide range of morphological types, all at distances allowing the galaxies to be resolved even at $160\mu\text{m}$. Observations of this sample with all instruments on *Spitzer Space Telescope* (Werner et al. 2004) are providing a new perspective on the dust abundances and dust properties in a diverse set of galaxies.

For 67 of the SINGS galaxies we have positive detections in the 4 bands of the *Infrared Array Camera* (IRAC; Fazio et al. (2004)) and the three bands of the *Multiband Imaging Photometer for Spitzer* (MIPS; Rieke et al. (2004)), spanning wavelengths from $3.6\mu\text{m}$ to $160\mu\text{m}$, the wavelength range within which dust radiates most of its power, including the PAH emission features that are prominent in many galaxies; 65 of these galaxies are used in the present study. For 11 galaxies we have global fluxes measured with the IRS $16\mu\text{m}$ peak-up filter. For 17 of the 65 galaxies, global $850\mu\text{m}$ flux measurements are also available from the SCUBA camera on the *JCMT*.

The IR emission from dust depends not only on the amount of dust present, but also on the rate at which it is heated by starlight. We develop a technique for estimation of dust masses and starlight intensities in galaxies, and apply it to estimate the total dust mass M_{dust} in each of the 65

galaxies in this study. For 61 galaxies we are also able to estimate a “PAH index” q_{PAH} – defined here to be the mass fraction of the dust that is contributed by polycyclic aromatic hydrocarbon (PAH) particles containing $< 10^3$ C atoms. In addition, we obtain information on the starlight intensity distribution – the mean starlight intensity scale factor $\langle U \rangle$, and the fraction of the dust heating that takes place in regions of high starlight intensities, including photodissociation regions.

The paper is organized as follows. The sample selection and observational data are summarized in §2, the physical dust models that are used are described in §3, and the model-fitting procedure is given in §4. In order to validate the model-fitting procedure, we first limit attention to the subset of SINGS galaxies for which SCUBA data are available (we will refer to these as the SINGS-SCUBA galaxies). In §5 we demonstrate that the dust modeling procedure works well for most of the SINGS-SCUBA galaxies, and we present dust masses, dust-to-gas mass ratios, PAH index values, and starlight intensity parameters obtained from these model fits. For the SINGS-SCUBA galaxies, our models do not require any contribution from the very cold (< 10 K) dust that has been reported by Krugel et al. (1998) for the spiral galaxies NGC 6156 and NGC 6918, or the 5 – 9 K dust that Galliano et al. (2003, 2005) reported for low metallicity dwarf galaxies, or the 4–6 K dust that Dumke et al. (2004) reported for the edge-on-spiral NGC 4631. The global SEDs do not show evidence for the submillimeter excess seen in the faint outer regions of NGC 4631 (Bendo et al. 2006b).

Submillimeter measurements are valuable to help constrain the dust models, but are unfortunately not available for most galaxies. In §6 we use the SINGS-SCUBA galaxies to develop a “restricted” fitting procedure that can be applied to galaxies for which submillimeter fluxes are unavailable. For the 17 galaxies with global $850\mu\text{m}$ fluxes from SCUBA, we show that the restricted fitting procedure, without employing SCUBA data, recovers dust masses and starlight intensities that are usually within a factor of two of the values obtained when the SCUBA data are used.

The restricted fitting technique is then applied to the remaining 48 galaxies to estimate dust masses and starlight intensities. Dust-to-gas mass ratios for the overall sample are presented in §7.1, where it is found that some of the SINGS galaxies have very low dust-to-gas ratios, and that the dust-to-gas ratios are correlated with both gas-phase metallicity and galaxy type. The dust-to-gas ratios depend on the assumed value of X_{CO} , the ratio of H_2 column density to CO line intensity; in §9.4 we argue that the distribution of derived dust-to-gas ratios supports $X_{\text{CO}} \approx 4 \times 10^{20} \text{ cm}^{-2} (\text{K km s}^{-1})^{-1}$.

Values of the PAH index q_{PAH} are estimated for 61 galaxies in §7.4. Many galaxies are found to have low values of q_{PAH} , and q_{PAH} is found to be strongly correlated with gas-phase metallicity. The starlight parameters for the 65 galaxy sample are presented and discussed in §8. The results are discussed in §9, and summarized in §10.

2. Data

2.1. IRAC and MIPS

Spitzer Space Telescope was used to observe all 75 galaxies in the SINGS sample, following the observing strategy described in Kennicutt et al. (2003). The observations in the 4 IRAC bands (3.6, 4.5, 5.7, 7.9 μ m) and 3 MIPS bands (24, 71, 160 μ m) have been reduced following the procedures described in Dale et al. (2005). The extended source aperture corrections found in Reach et al. (2005) were applied to the IRAC data. Global IRAC and MIPS photometry for these galaxies is taken from Dale et al. (2007), which included (usually modest) corrections for aperture size and nonlinearity of the 71 μ m detectors.

Ten of the SINGS galaxies were excluded from the present study:

- NGC 584 (E4) may be contaminated by a background source, and also has low surface brightness in the MIPS bands compared to the foreground cirrus.
- NGC 3034 = M 82 (I0, starburst): Saturation of the bright core of this galaxy precludes global photometry.
- NGC 1404 (E1): An off-center IR source contributes a significant fraction of the MIPS flux, but it is not known whether or not it is a foreground/background object.
- NGC 4552 (E0) has low surface brightness compared to the foreground cirrus emission, and the MIPS 160 μ m photometry is very uncertain.
- The dwarf galaxies M81dwA and Ho IX are not detected at $\lambda \geq 5.8\mu$ m.
- The dwarf galaxies DDO 154 and DDO 165 are only marginally ($< 3\sigma$) detected at 71 and 160 μ m, and M81dwB is a $< 2\sigma$ detection at 160 μ m.
- The dwarf starburst galaxy NGC 1377 shows strong silicate absorption at 9.8 μ m and 18 μ m (Roussel et al. 2006). The objective of the present study is to model the IR spectra using a simple model that assumes the galaxy to be optically-thin at $\lambda > 3.5\mu$ m; because NGC 1377 is clearly not optically thin, it has been removed from the sample.

The sample studied here therefore consists of 65 galaxies. MIPS 71 μ m photometry for NGC 7552 is not usable because of detector saturation, but NGC 7552 is retained in the sample because it is well-observed at other wavelengths and with other instruments.

Most of the dust mass in galaxies is relatively cool, radiating primarily at wavelengths in the MIPS 71 μ m and 160 μ m bands. Dust grains that are warmer, either because they are in regions with intense starlight, or because they are very small grains immediately following absorption of a stellar photon, may radiate strongly in the MIPS 24 μ m band and shortward. The variety of dust

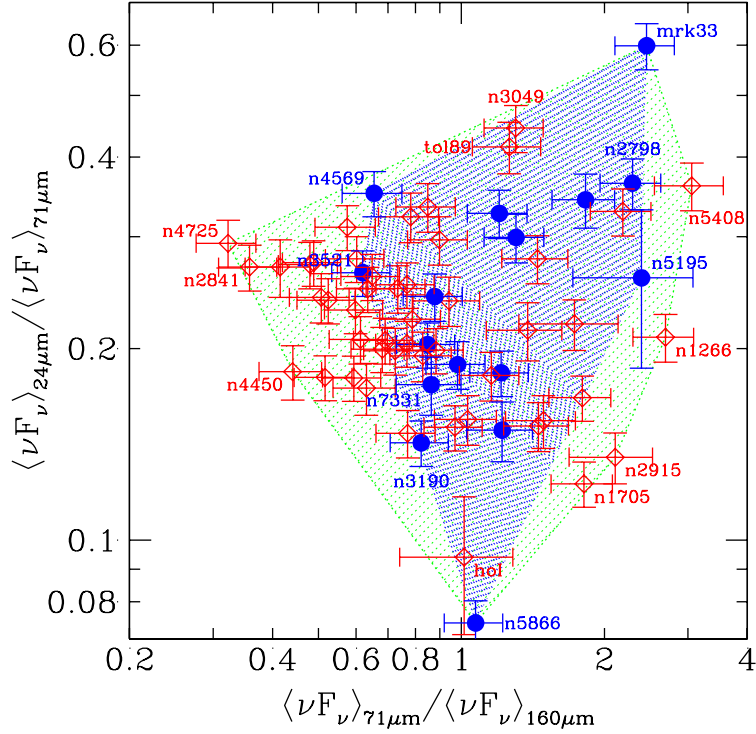


Fig. 1.— MIPS color-color plot for the 65 galaxies. The blue shaded area shows the region sampled by the 17 galaxies for which global SCUBA fluxes are known (plotted as blue solid symbols) – these only partially cover the color-color space populated by the SINGS sample (green shaded area). Galaxies without SCUBA fluxes are shown in red. Galaxies with relatively extreme flux ratios are labelled.

conditions found in the SINGS sample is evident from the distribution of the 64 galaxies in MIPS color-color space, shown in Figure 1: $\langle \nu F_\nu \rangle_{71\mu\text{m}} / \langle \nu F_\nu \rangle_{160\mu\text{m}}$ varies by over a factor of 10 within our sample, and $\langle \nu F_\nu \rangle_{24\mu\text{m}} / \langle \nu F_\nu \rangle_{71\mu\text{m}}$ varies by a factor of 8. These variations in MIPS colors presumably reflect galaxy-to-galaxy differences in the intensity of the starlight heating the dust grains, although galaxy-to-galaxy differences in dust composition may also play a role. It is evident from the scatter in Figure 1 that the MIPS 24/71 color is not simply a function of the 71/160 color: the MIPS colors cannot be described by a one-parameter sequence of, e.g., “dust temperature”. Realistic dust models will therefore need to vary at least two parameters to account for the range in observed MIPS colors.

The SINGS sample does not include any powerful AGN, and in all SINGS galaxies the global flux in the IRAC 3.6 μm band is starlight-dominated. Neglecting extinction, we can estimate the “nonstellar” flux in longer-wavelength bands by subtracting the estimated stellar contribution, assuming a 5000 K blackbody. For IRAC band 4, the IRS 16 μm Pickup band (see §2.2 below) and

the MIPS $24\mu\text{m}$ band, the nonstellar fluxes are:

$$\langle F_\nu^{\text{ns}} \rangle_{7.9} = \langle F_\nu \rangle_{7.9} - 0.260 \langle F_\nu \rangle_{3.6} \quad , \quad (1)$$

$$\langle F_\nu^{\text{ns}} \rangle_{16} = \langle F_\nu \rangle_{16} - 0.0693 \langle F_\nu \rangle_{3.6} \quad , \quad (2)$$

$$\langle F_\nu^{\text{ns}} \rangle_{24} = \langle F_\nu \rangle_{24} - 0.0326 \langle F_\nu \rangle_{3.6} \quad . \quad (3)$$

The coefficients 0.260 and 0.0326 in eq. (1) and (3) are close to the values 0.232 and 0.032 estimated by Helou et al. (2004). Some stars (e.g., cool red giants, and AGB stars) have circumstellar dust that is in many cases warm enough to radiate strongly at wavelengths from $8\text{--}30\mu\text{m}$. If such stars are sufficiently numerous, the result will be a “stellar” contribution to the 8, 16, and $24\mu\text{m}$ fluxes that will be larger than assumed in eq. (1–3). In the absence of extinction at $3.6\mu\text{m}$, equations (1–3) will therefore *overestimate* the flux contributed by interstellar dust.

2.2. IRS $16\mu\text{m}$

In addition to IRAC and MIPS photometry, nine of the SINGS galaxies have been imaged using the IRS “blue peak-up” detector array, with nominal wavelength $\lambda = 16\mu\text{m}$. The IRS blue peak-up observations were taken as part of the IRS instrument calibration program and consist of a grid of pickup images covering the full extent of each galaxy. The reduced images, processed by IRS pipeline version S14, were mosaicked using the MOPEX program (ver. 030106) to remove cosmic rays after subtraction of a custom dark image. This custom dark image was created using images taken beyond the visible extent of the galaxy. In some cases, the best dark subtraction was found to require allowing the dark image to vary with time. “Sky” (zodiacal light and Galactic cirrus) contributions were also removed by this custom dark subtraction step. The total $16\mu\text{m}$ flux was measured using the same methods used for the IRAC and MIPS fluxes (Dale et al. 2005). The measured global fluxes were then scaled down by $\sim 15\%$, to account for a recent SSC calibration update ($\sim 10\%$), and the appropriate aperture correction factor ($\sim 5\%$). Fluxes for these 11 galaxies at $16\mu\text{m}$ and $24\mu\text{m}$ are given in Table 1. The flux density ratio $\langle F_\nu \rangle_{16} / \langle F_\nu \rangle_{24}$ varies considerably among these galaxies, from a low of 0.376 ± 0.033 for NGC 7552 to a high of 1.21 ± 0.12 for NGC 3190.

Figure 2a shows $P_{16} \equiv \langle \nu F_\nu^{\text{ns}} \rangle_{16} / (\langle \nu F_\nu \rangle_{71} + \langle \nu F_\nu \rangle_{160})$ vs. $P_{24} \equiv \langle \nu F_\nu^{\text{ns}} \rangle_{24} / (\langle \nu F_\nu \rangle_{71} + \langle \nu F_\nu \rangle_{160})$ for the ten galaxies for which we have 16, 24, 71, and $160\mu\text{m}$ photometry, where F_ν^{ns} is the nonstellar contribution from eq. (1–3). The flux ratio P_{16} remains essentially constant at $P_{16} \approx 0.112 \pm 0.017$ while P_{24} varies by almost a factor of 3, from 0.06 to 0.18. This suggests that the $16\mu\text{m}$ flux is not emitted by the same grains as the $24\mu\text{m}$ flux. In the dust model of Draine & Li (2007, hereafter DL07), a minimum level of $24\mu\text{m}$ emission is produced by single-photon heating of PAHs or ultrasmall grains (with $\langle \nu L_\nu \rangle_{24} / L_{\text{TIR}} \approx 0.03 - 0.06$, depending on q_{PAH} – see Fig. 15 of DL07), but P_{24} increases as the starlight intensity increases. Figure 2a suggests that the $16\mu\text{m}$ emission may be dominated by single-photon heating of PAHs, remaining relatively constant even as P_{24} rises due to increased starlight heating. This is supported by Figure 2b, which shows that the ratio

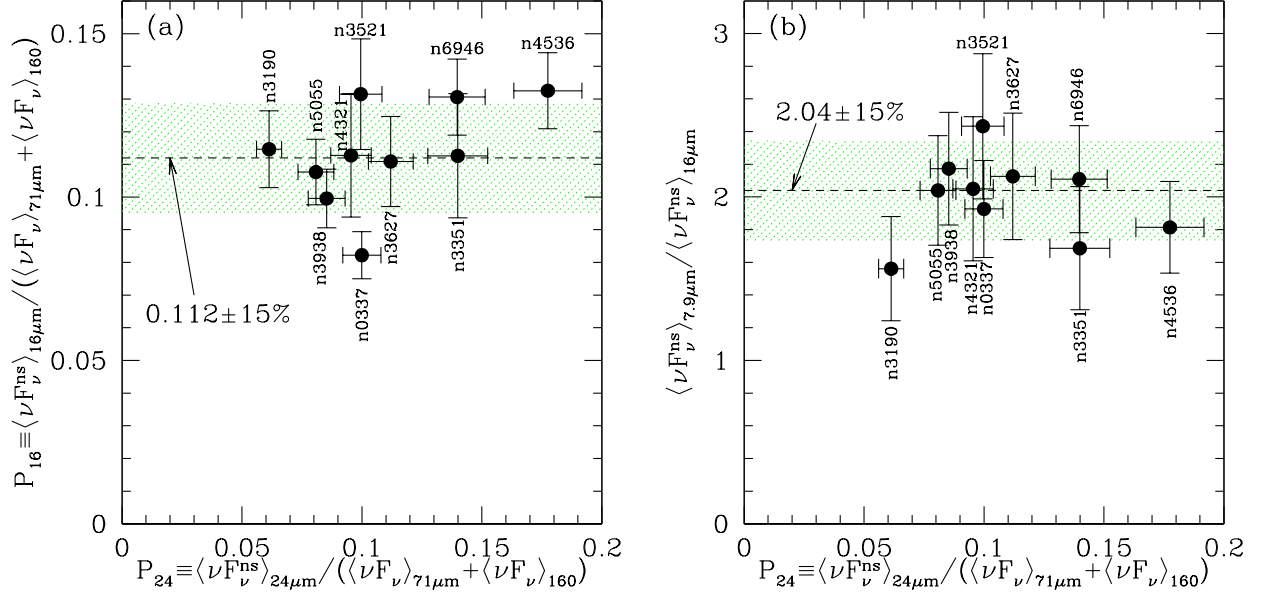


Fig. 2.— (a) $P_{16} \equiv \langle \nu F_{\nu}^{\text{ns}} \rangle_{16\mu\text{m}} / (\langle \nu F_{\nu} \rangle_{71\mu\text{m}} + \langle \nu F_{\nu} \rangle_{160})$ versus $P_{24} \equiv \langle \nu F_{\nu}^{\text{ns}} \rangle_{24\mu\text{m}} / (\langle \nu F_{\nu} \rangle_{71\mu\text{m}} + \langle \nu F_{\nu} \rangle_{160})$ for the 10 galaxies imaged with the IRS 16 μm peak-up filter for which we also have global MIPS fluxes (NGC 7552 is excluded). (b) $\langle \nu F_{\nu}^{\text{ns}} \rangle_{7.9\mu\text{m}} / \langle \nu F_{\nu}^{\text{ns}} \rangle_{16\mu\text{m}}$ vs P_{24} . Both the ratio of nonstellar 16 μm emission to total IR power and the ratio of nonstellar 7.9 μm emission to nonstellar 16 μm emission remain constant to within $\sim 15\%$, even as P_{24} varies by a factor of 3.

of 7.9 μm emission to 16 μm emission is nearly constant for this sample, varying by only $\sim \pm 15\%$ over the eight galaxies, consistent with the idea that both are primarily the result of single-photon heating of PAHs. This is consistent with the finding by Förster Schreiber et al. (2004) that, when averaged over disks of spiral galaxies, the 15 μm continuum intensity is proportional to the PAH intensity in the 5–8 μm region.

Table 1. Global Fluxes (Jy) in IRS 16 μm Peak-Up Band

galaxy	$\langle F_{\nu} \rangle_{16}$ Jy	$\langle F_{\nu} \rangle_{24}$ Jy	$\langle F_{\nu} \rangle_{16} / \langle F_{\nu} \rangle_{24}$
NGC 0337	0.375 ± 0.029	0.678 ± 0.028	0.553 ± 0.049
NGC 3190	0.322 ± 0.030	0.267 ± 0.011	1.21 ± 0.12
NGC 3351	1.39 ± 0.23	2.583 ± 0.12	0.538 ± 0.091
NGC 3521	4.86 ± 0.59	5.51 ± 0.22	0.88 ± 0.11
NGC 3627	4.92 ± 0.58	7.42 ± 0.30	0.663 ± 0.082
NGC 3938	0.849 ± 0.068	1.087 ± 0.045	0.781 ± 0.070
NGC 4321	2.64 ± 0.43	3.34 ± 0.13	0.79 ± 0.13
NGC 4536	1.74 ± 0.14	3.46 ± 0.14	0.503 ± 0.044
NGC 5055	5.09 ± 0.43	5.73 ± 0.23	0.888 ± 0.083
NGC 6946	12.8 ± 1.02	20.37 ± 0.81	0.628 ± 0.056
NGC 7552	4.01 ± 0.31	10.66 ± 0.44	$0.376 \pm .033$

2.3. SCUBA

The dust properties in a galaxy will be best determined if submillimeter photometry is available to constrain the quantity of cool dust present. SCUBA observations at $450\mu\text{m}$ and/or $850\mu\text{m}$ are available for 26 of the 65 galaxies,¹ but not all of these are usable in the present study:

1. NGC 4254, NGC 4579, NGC 5194, and NGC 6946 were scan-mapped, and the data processing removes an unknown amount of extended emission. Thus global $850\mu\text{m}$ (or $450\mu\text{m}$) fluxes are not available for these galaxies. We restrict ourselves to data obtained in “jiggle map” mode, except for the scan-map observations of NGC 5195, for which background subtraction is thought to be more reliable because of the smaller angular extent of NGC 5195.
2. For some galaxies the SCUBA map did not fully cover the region where $160\mu\text{m}$ emission is detected. Dale et al. (2005) multiplied the observed SCUBA fluxes by a correction factor based on the fraction of the $160\mu\text{m}$ emission coming from the region mapped by SCUBA. Because the $850\mu\text{m}/160\mu\text{m}$ flux ratio may be spatially variable, we choose here to not use the $850\mu\text{m}$ flux estimates for galaxies where the correction factor exceeds 1.6 (NGC 1097, NGC 4321, NGC 4736, and NGC 5033).
3. For the Sombrero galaxy, NGC 4594, the $850\mu\text{m}$ flux is dominated by the AGN (Bendo et al. 2006a), and the extranuclear $850\mu\text{m}$ flux is not reliably measured, so we cannot use the SCUBA data to constrain the dust model for this galaxy.

We thus have 17 galaxies where the dust models are constrained by $850\mu\text{m}$ SCUBA data (with $450\mu\text{m}$ fluxes for 3 of the 17) in addition to IRAC and MIPS data. The global fluxes $F_{\text{obs},b}$ and $1\text{-}\sigma$ uncertainties for each band b are taken from Dale et al. (2007).

The 16^2 galaxies for which we have global SCUBA and MIPS photometry are indicated in Figure 1. While the galaxies with SCUBA photometry span a considerable portion of the populated region in MIPS color-color space, a number of the SINGS galaxies have MIPS colors that are outside of the range seen among the galaxies for which SCUBA data are available. For example, NGC 4725 or NGC 5408, with $\langle\nu F_\nu\rangle_{71\mu\text{m}}/\langle\nu F_\nu\rangle_{160\mu\text{m}} = 0.33$ and 3.1 , respectively, fall outside the range $0.6\text{--}2.4$ observed for this ratio among the SINGS-SCUBA galaxies. The dust models discussed below are able to reproduce the IRAC and MIPS fluxes for all of the SINGS galaxies. Galaxies such as NGC 4725 or NGC 2841, with the lowest values of $\langle\nu F_\nu\rangle_{71\mu\text{m}}/\langle\nu F_\nu\rangle_{160\mu\text{m}}$, require cooler dust (i.e., lower starlight intensities) than any of the SINGS-SCUBA galaxies. NGC 5408, with a very high value of $\langle\nu F_\nu\rangle_{71\mu\text{m}}/\langle\nu F_\nu\rangle_{160\mu\text{m}}$, requires hotter dust (higher starlight intensities). Submillimeter observations would be of great value to test the predicted submm fluxes from these extreme cases.

¹The 25 galaxies in Table 3 of Dale et al. (2005), plus NGC 1482

²NGC 7552 is absent from Fig. 1 because of detector saturation at $71\mu\text{m}$.

2.4. IRAS and ISO

IRAS photometry is obtained from the latest SCANPI data for most SINGS sources, and from HiReS maps for the largest SINGS targets (optical diameters $\gtrsim 10'$), except in some bands (e.g., no IRAS $12\mu\text{m}$ flux for NGC 0024). A 20% calibration uncertainty estimate was applied. In the case of NGC 5195 (=M51b), the proximity of NCG 5194 (=M51a) made flux determination more difficult, and 50% uncertainty estimates were adopted.

The IRAS $25\mu\text{m}$ flux densities are not used, as they are superseded by the MIPS $24\mu\text{m}$ photometry at essentially the same wavelength, but we employ the IRAS $12\mu\text{m}$, $60\mu\text{m}$, and $100\mu\text{m}$ photometry in our model-fitting.

When available, we show ISOCAM $6.75\mu\text{m}$ and $15\mu\text{m}$ photometry in the figures showing the spectral energy distributions (SEDs), but they are not used in the model-fitting.

3. Physical Dust Models

A direct estimate for the dust-to-hydrogen mass ratio $M_{\text{dust}}/M_{\text{H}}$ in the local Milky Way can be obtained from the difference between total interstellar abundances – taken to be equal to current estimates for solar abundances – and observed gas phase abundances in diffuse interstellar clouds, where the intensively studied diffuse cloud on the line-of-sight to ζOph is taken to be representative. Using current estimates of solar abundances, this mass inventory results in $M_{\text{dust}}/M_{\text{H}} \approx 0.0073$ (see Table 2).

We will apply (and thereby also test) the dust models developed by Weingartner & Draine (2001a, hereafter WD01) and Li & Draine (2001, hereafter LD01), and updated by DL07. These dust models consist of specified mixtures of carbonaceous grains and amorphous silicate grains, with the smallest carbonaceous grains having the physical properties of polycyclic aromatic hydrocarbon (PAH) particles; the size distributions are chosen to reproduce the observed wavelength-dependent extinction in the local Milky Way, in the Large Magellanic Cloud, and the Small Magellanic Cloud bar region (Weingartner & Draine 2001a). Li & Draine (2001, 2002) showed that these grain models appeared to be consistent with the observed IR emission from diffuse clouds in the Milky Way and the Small Magellanic Cloud.

The DL07 dust models used here adopt PAH optical properties that are slightly different from those adopted by LD01. As discussed by DL07, the changes are in part to better conform to recent theoretical estimates for band strengths, and in part to improve agreement with band profiles determined observationally by Smith et al. (2007).

The PAH emission features at $3.3\mu\text{m}$, $6.2\mu\text{m}$, $7.7\mu\text{m}$, $8.6\mu\text{m}$, $11.3\mu\text{m}$, $12.0\mu\text{m}$, $12.7\mu\text{m}$, $16.4\mu\text{m}$, and $17\mu\text{m}$ are prominent in many galaxy spectra, and the dust models considered here include various abundances of PAHs; in each model the PAHs have a wide range of sizes. Because PAH

Table 2. Dust Mass per H from Milky Way Abundances

X	$(N_X/N_H)_\odot(\text{ppm})^a$	$(N_X/N_H)_{\text{gas}}/(N_X/N_H)_\odot^a$	$M_{X,\text{dust}}/M_H$
C	247	0.57	0.0013
N	85	0.72	0.0003
O	490	0.73	0.0021
Mg	38	0.08	0.0008
Al	3^b	$\lesssim 0.1^c$	0.0001
Si	32	0.05	0.0009
Ca	2^b	0.0002^d	0.0001
Fe	29	0.007	0.0016
Ni	2	0.004	0.0001
total			0.0073

^a Jenkins (2004) except as noted.
^b $(N_X/N_H)_\odot$ from Grevesse & Sauval (1998)
^c assumed
^d Savage & Sembach (1996)

Table 3. Physical Dust Models

j_M	Model	q_{PAH} %	$M_{\text{dust}}/M_H^{a,b}$	A_V/N_H $\text{mag cm}^2/\text{H}$
1	MW3.1_00	0.47	0.0100	5.3×10^{-22}
2	MW3.1_10	1.12	0.0100	5.3×10^{-22}
3	MW3.1_20	1.77	0.0101	5.3×10^{-22}
4	MW3.1_30	2.50	0.0102	5.3×10^{-22}
5	MW3.1_40	3.19	0.0102	5.3×10^{-22}
6	MW3.1_50	3.90	0.0103	5.3×10^{-22}
7	MW3.1_60	4.58	0.0104	5.3×10^{-22}
8	LMC2_00	0.75	0.00343	1.2×10^{-22}
9	LMC2_05	1.51	0.00344	1.2×10^{-22}
10	LMC2_10	2.40	0.00359	1.2×10^{-22}
11	SMCbar	0.010	0.00206	6.2×10^{-23}

^a $M_H \equiv M(\text{HI} + \text{H}_2)$
^b $M_{\text{dust}}/M_{\text{gas}} = [M_{\text{dust}}/M_H]/1.36$

emission is mainly the result of single-photon heating, the PAH emission spectrum depends on the size (heat capacity) of the PAH. The prominent $6.2\mu\text{m}$, $7.7\mu\text{m}$, and $8.6\mu\text{m}$ emission features are primarily due to PAHs with $\lesssim 10^3$ C atoms [see Fig. 7 of Draine & Li (2007)]. Following DL07, we characterize the PAH abundance by a “PAH index” q_{PAH} , defined to be the percentage of the total grain mass contributed by PAHs containing less than 10^3 C atoms:

$$q_{\text{PAH}} \equiv \frac{M(\text{PAHs with } N_{\text{C}} < 10^3)}{M_{\text{dust}}} , \quad (4)$$

where M_{dust} includes the mass of all silicate and carbonaceous dust, including the PAHs.

WD01 put forward seven different size distributions for dust in the diffuse ISM of the Milky Way. The models are all consistent with the average interstellar extinction law, but have different PAH abundances, ranging from $q_{\text{PAH}} = 0.47\%$ to 4.6% . Some properties for these seven models are given in Table 3, where the dust masses are calculated assuming densities of 3.5 g cm^{-3} for silicates, 2.24 g cm^{-3} for carbonaceous grains (WD01). The WD01 Milky Way dust models have $M_{\text{dust}}/M_{\text{H}} \approx 0.010$, about 40% larger than the value 0.0073 estimated from observed depletions (see Table 2), assuming solar abundances of C, Mg, Si, and Fe in the local interstellar medium. It is possible that current estimates of solar abundances of C, Mg, Si, and Fe may be lower than the actual elemental abundances in the interstellar medium today; a $\sim 25\%$ increase in the solar abundances would bring $M_{\text{dust}}/M_{\text{H}}$ estimated from depletions into accord with the WD01 model. Alternately, it is possible that the WD01 model overestimates the mass of interstellar dust by a factor 1.4 or so.

The PAHs constitute the small size end of the carbonaceous grain population; the varying PAH abundances are the result of varying the grain size distribution, while holding the overall extinction constant. The model with the largest PAH abundance appears to reproduce the observed IR-submm emission from dust in the local interstellar medium (LD01, DL07). Because it is likely that the PAH abundance varies from galaxy-to-galaxy, here we take linear combinations of these models to produce a sequence of 43 MW models with $q_{\text{PAH}} = 0.4\%$ to 4.6% in steps of 0.1% .

Similarly, we take linear combinations of the 3 WD01 models (as modified by DL07) for dust in the LMC2 region (with $q_{\text{PAH}} = 0.75, 1.49$, and 2.37%) to produce a sequence of 18 LMC models with $q_{\text{PAH}} = 0.7\%$ to 2.4% .

The dust models include amorphous silicate grains. We assume optically-thin dust when modeling the global SEDs, and therefore the models presented here do not include silicate absorption at $9.8\mu\text{m}$. Such absorption is in fact seen in observed spectra of the nuclei of a few of the galaxies in this sample – e.g., NGC 3198 (Smith et al. 2007) – but we neglect dust absorption in modeling the global emission.

The dust models employed here do not include H_2O and other ices. H_2O ice is known to be present in dark clouds in the Milky Way, in regions where $A_V \gtrsim 3.3\text{ mag}$ (Whittet et al. 1988). In these regions, ices will modify the optical properties of the dust. However, it appears that such dark regions contain at most a modest fraction of the total dust in a galaxy; furthermore, the weak

starlight in such regions implies that the dust grains located there radiate only a very small fraction of the total IR power. As will be seen below, an ice-free dust model appears to be satisfactory for modeling the IR emission from normal galaxies.

4. Constraining the Dust Model and Starlight Intensities

In addition to choosing a physical dust mixture (relative numbers of carbonaceous grains and silicate grains of different sizes, including the fraction q_{PAH} of the dust mass that is in PAHs), we must specify the intensity of the radiation that is heating the dust grains. Almost all of the heating of dust grains in a normal galaxy is from absorption of $h\nu < 13.6 \text{ eV}$ photons. In a normal star-forming galaxy a significant (but sub-dominant) fraction of the stellar luminosity may be at $h\nu > 13.6 \text{ eV}$, but most of these photons end up photoionizing hydrogen or helium rather than being absorbed by dust. The $h\nu < 13.6 \text{ eV}$ recombination radiation – especially Lyman α – may be largely absorbed by dust. However, the total power in ionizing photons is a minor fraction of the total stellar luminosity in a galaxy with a more-or-less steady rate of star formation. Only in galaxies that have undergone an extreme burst of star formation within the last $\sim 10^7$ yrs will the dust heating be dominated by Lyman α and Lyman continuum radiation. Only in rare cases, e.g., NGC 1377 (Roussel et al. 2006), where the massive stars formed in a starburst are surrounded by dense, dusty H II regions, will the dust grains directly absorb a major fraction of the $h\nu > 13.6 \text{ eV}$ radiation.

The IR emission from dust is relatively insensitive to the detailed spectrum of the $h\nu < 13.6 \text{ eV}$ photons, and the DL07 models simply adopt the spectrum of the local interstellar radiation field as a reasonable representation for the average spectrum of the interstellar radiation in a normal spiral galaxy. The specific energy density of starlight is therefore taken to be

$$u_\nu = U \times u_\nu^{(\text{MMP83})} \quad , \quad (5)$$

where $u_\nu^{(\text{MMP83})}$ is the specific energy density estimated by Mathis et al. (1983) (hereafter MMP83) for the local Galactic interstellar radiation field, and U is a dimensionless scale factor. The intensity of interstellar UV radiation is often characterized by G_0 , the ratio of the 6–13.6 eV energy density relative to the value $5.288 \times 10^{-14} \text{ ergs cm}^{-3}$ for the radiation field estimated by Habing (1968). The MMP83 ISRF has $u(0 - 13.6 \text{ eV starlight}) = 8.65 \times 10^{-13} \text{ ergs cm}^{-3}$, and $u(6 - 13.6 \text{ eV}) = 6.01 \times 10^{-14} \text{ ergs cm}^{-3}$. Thus $U = 0.88 G_0$.

Dust at different locations in the galaxy will be exposed to different radiation intensities. A physically correct model would specify the locations of the stellar sources and the absorbing dust, and would solve the radiative transfer problem [e.g., Tuffs et al. (2004)], but this would require many uncertain assumptions about the relative distributions of stars and dust, as well as massive numerical computations.

Following DL07, we suppose that a large fraction of the dust in a galaxy is located in the

diffuse interstellar medium, exposed to starlight with an intensity that does not vary much within the galaxy. This “diffuse ISM” dust is idealized as being heated by a single radiation field, with intensity factor $U = U_{\min}$. In addition, DL07 suppose that a small fraction of the dust is located in regions where the radiation field is more intense, with a wide range of intensities ranging from $U = U_{\min}$ to $U = U_{\max} \gg U_{\min}$. This would include dust in photodissociation regions, so we refer to this as the “PDR” component, and we use the power-law distribution function used by DL07. Although this “PDR” component contains only a small fraction of the total dust mass, in some galaxies it contributes a substantial fraction of the total power radiated by the dust. The models do not include a component corresponding to cold dust in dark clouds; as discussed in §9.1, such cold dust appears to account for a minor fraction of the dust mass, and a very small fraction of the total dust luminosity. Thus, following DL07, we take the dust mass dM_{dust} exposed to radiation intensities in $[U, U + dU]$ to be a combination of a δ function and a power-law,

$$\frac{dM_{\text{dust}}}{dU} = (1 - \gamma)M_{\text{dust}}\delta(U - U_{\min}) + \gamma M_{\text{dust}} \frac{(\alpha - 1)}{U_{\min}^{1-\alpha} - U_{\max}^{1-\alpha}} U^{-\alpha} \quad \text{for } U_{\min} \leq U \leq U_{\max}, \alpha \neq 1 \quad (6)$$

where δ is the Dirac δ function. This distribution function has five parameters: the total dust mass M_{dust} , the fraction γ of the dust mass that is associated with the power-law part of the starlight intensity distribution, and 3 parameters (U_{\min} , U_{\max} , α) characterizing the distribution of starlight intensities in the high intensity regions. The δ -function term represents the fraction $(1 - \gamma)$ of the dust that is heated by a general diffuse interstellar radiation field with approximately uniform intensity $\sim U_{\min}$. The power-law part of the distribution function, introduced by Dale et al. (2001) and used by Li & Draine (2002), represents the fraction γ of the dust mass that is close to OB associations and is exposed to radiation with intensity $U > U_{\min}$; this includes the dust in “photodissociation regions” (PDRs), where radiation intensities can be orders of magnitude higher than the “average” dust grain is exposed to. Equation (6) is a very simplistic description of the distribution of dust grain environments; it neglects the possibility that the dust properties (composition, size distribution) might be variable and correlated with U , and also neglects regional variations in the spectrum of the starlight irradiating the dust. Despite its simplicity, we will see here that eq. (6) appears to capture the essential elements of the distribution of starlight intensities found in galaxies, yielding models with SEDs that approximate what is observed.

Very small particles cool almost completely between photon absorptions, and therefore the shape of the emission spectrum from these grains is almost independent of U . The larger grains, that account for more than half of the total absorption of starlight in the Milky Way, do not cool significantly between photon absorptions, and their temperature depends on the intensity U . The observed FIR emission spectrum is sensitive to the temperature of these larger grains, and therefore allows us to constrain the distribution function for U . While *Spitzer Space Telescope* provides unprecedented sensitivity to FIR emission, the spectral coverage is somewhat sparse, with a factor of 3 gap in wavelength between IRAC 7.9 μm and the MIPS 24 μm bands, and a factor of 2.9 gap between the MIPS 24 μm and 71 μm bands. The IRS “Peak-Up” mode observations can be used for imaging at 16 μm and 26 μm , but these observations are not generally available. The large

gaps in wavelength coverage leave considerable uncertainty in the spectral energy distribution at wavelengths between the bands.³ Furthermore, the longest wavelength band, at $160\mu\text{m}$, falls on the short wavelength side of the emission peak for dust temperatures $T_d \lesssim (1/6)hc/(160\mu\text{m}) = 15\text{ K}$. As a result, *Spitzer* photometry does not strongly constrain the abundance of dust with temperatures $T_d \lesssim 15\text{ K}$. To determine the amount of cool dust, global submillimeter observations are required. Fortunately, such data exist for 17 of the 65 galaxies for which we have complete *Spitzer* photometry (or near-complete in the case of NGC 7552), and this subsample will be analyzed first, in §5.

We select a model for the IR emission from a galaxy as follows. For each size and composition of dust, we precompute and tabulate the temperature distribution function for the dust grain illuminated by the radiation field of eq. (5) for selected values of U (with $0.1 \leq U \leq 10^7$), using heat capacities, absorption cross sections, and numerical methods described by Draine & Li (2001), LD01, and DL07. Neutral and ionized PAHs are assumed to have different absorption cross sections. The ionized fraction $\phi_i(N_C)$ (a function of the number N_C of carbon atoms in the PAH) will depend primarily on the ratio $U\sqrt{T_e}/n_e$, where n_e and T_e are the electron density and temperature (Bakes & Tielens 1994; Weingartner & Draine 2001b). Here we take the ionized fraction $\phi_i(N_C)$ estimated by LD01 for the local diffuse ISM⁴ (we are therefore implicitly assuming that other galaxies have the same mix of $U\sqrt{T_e}/n_e$ as the Milky Way). Our model-fitting procedure assumes that all galaxies have the same shape for the PAH size distribution, the same PAH ionized fraction $\phi_i(N_C)$, and the same spectral shape of the illuminating starlight. As a result, our model fits have fixed ratios of PAH emission band strengths. Observations do reveal variations in PAH band ratios from one galaxy to the next – for example, $L(7.7\mu\text{m})/L(11.3\mu\text{m})$ varies from $\sim 4\text{--}5$ to $\lesssim 0.7$ as we progress from H II-dominated nuclei to AGN-dominated nuclei (Smith et al. 2007), and low values of $L(7.7\mu\text{m})/L(11.3\mu\text{m})$ are also seen in some AGN-free galactic and extragalactic regions (e.g., Reach et al. 2000; Hony et al. 2001; Pagani et al. 1999) – but most spiral galaxies have global PAH feature ratios that are near-average and characteristic of star-forming regions.

With these temperature distribution functions for the dust, and the dust absorption cross section $C_{\text{abs}}(\lambda)$, we can calculate the time-averaged IR emission for a given grain type and size for each of the discrete values of U considered; we then sum over the grain types and sizes for a dust model j_M (see Table 3) to find the power radiated per unit frequency per unit mass of dust mixture j_M exposed to starlight intensity U :

$$p_\nu^{(0)}(j_M, U) = \frac{1}{M(j_M)} \sum_k \int da \left(\frac{dn_k}{da} \right)_{j_M} \int dT \frac{dP(k, a)}{dT} 4\pi B_\nu(T) C_{\text{abs}}(a, \lambda) \quad (7)$$

³ In principle, the IRS instrument can provide 6–36 μm photometry, and the MIPS SED mode covers 55–95 μm , but observing time considerations preclude using these observing modes for large areas.

⁴ Following LD01, we assume 43% of the dust to be in the “cold neutral medium” (CNM; $n_e/U \approx 0.045\text{ cm}^{-3}$, $T \approx 100\text{ K}$), 43% to be in the “warm neutral medium” (WNM; $n_e/U \approx 0.04\text{ cm}^{-3}$, $T \approx 6000\text{ K}$), and 14% to be in the “warm ionized medium” (WIM; $n_e/U \approx 0.1\text{ cm}^{-3}$, $T \approx 8000\text{ K}$). The resulting $\phi_i(N_C)$ is shown in Fig. 7 of LD01 and Fig. 8 of DL07.

$$M(j_M) \equiv \sum_k \int da \left(\frac{dn_k}{da} \right)_{j_M} \frac{4\pi a^3}{3} \rho_k, \quad (8)$$

where the sum runs over the different grain types k (amorphous silicate, graphite, PAH⁰, PAH⁺) in the DL07 dust model, with ρ_k the density of material k , and $n_k(a)$ being the number of dust grains of type k per H nucleon, with radii $\leq a$.

We also calculate the specific power per unit dust mass

$$p_\nu(j_M, U_{\min}, U_{\max}, \alpha) \equiv \frac{(\alpha - 1)}{U_{\min}^{1-\alpha} - U_{\max}^{1-\alpha}} \int_{U_{\min}}^{U_{\max}} p_\nu^{(0)}(j_M, U) U^{-\alpha} dU \quad (9)$$

for a power-law distribution of starlight intensities, $dM_{\text{dust}}/dU \propto U^{-\alpha}$. For each dust model j_M we consider a range of values of U_{\min} and U_{\max} .

At wavelengths $\lambda \lesssim 5 \mu\text{m}$, the emission from a galaxy is dominated by starlight. For $\lambda \geq 3.6 \mu\text{m}$ we neglect reddening, and approximate the stellar contribution by a dilute blackbody with color temperature $T_\star = 5000 \text{ K}$, which Smith et al. (2007) found to provide a suitable approximation to the stellar continuum at $\lambda > 5 \mu\text{m}$. The model emission spectrum is then

$$F_{\nu, \text{model}} = \Omega_\star B_\nu(T_\star) + \frac{M_{\text{dust}}}{4\pi D^2} \left[(1 - \gamma) p_\nu^{(0)}(j_M, U_{\min}) + \gamma p_\nu(j_M, U_{\min}, U_{\max}, \alpha) \right], \quad (10)$$

where Ω_\star is the solid angle subtended by the stars. For each $(j_M, U_{\min}, U_{\max}, \alpha)$, we obtain Ω_\star , M_{dust} , and γ by minimizing

$$\chi^2 \equiv \sum_b \frac{[F_{\text{obs}, b} - \langle F_{\nu, \text{model}} \rangle_b]^2}{\sigma_{\text{obs}, b}^2 + \sigma_{\text{model}, b}^2}, \quad (11)$$

where the sum is over observed bands b , $\langle F_{\nu, \text{model}} \rangle_b$ is the model spectrum convolved with the response function for band b , and $\sigma_{\text{obs}, b}$ is the observational uncertainty in the observed flux density $F_{\text{obs}, b}$ for band b . The *ad-hoc* insertion of the $\sigma_{\text{model}, b}^2$ term in the denominator in eq. (11) is to allow for the approximate nature of our models and is motivated by the very high photometric accuracy achieved for the MIPS $24 \mu\text{m}$ photometry, with $\sigma_{\text{obs}, 24 \mu\text{m}}/F_{\text{obs}, 24 \mu\text{m}} = 0.040$ achieved for many of the SINGS galaxies. We do not want the fitting procedure to give extreme weight to one or two bands where $F_{\text{obs}, b}$ may have been measured with very high precision (*i.e.*, small $\sigma_{\text{obs}, b}/F_{\text{obs}, b}$) because we do not expect our models to fit perfectly in the limit of perfect observations. Our subjective sense is that the present models should be regarded as satisfactory if they are able to reproduce the actual fluxes (*i.e.*, perfect data, with $\sigma_{\text{obs}, b} = 0$) to within, say, $\pm 10\%$. We therefore arbitrarily set $\sigma_{\text{model}, b} = 0.1 \langle F_{\nu, \text{model}} \rangle_b$ for each band b . It is important to recognize that eq. (11) differs from the usual χ^2 used for testing models, and the numerical values of χ^2 found here are not rigorous measures of the goodness-of-fit. Nevertheless, these χ^2 values do appear to provide a practical guide to distinguish between good fits and poor fits.

The model components must be nonnegative: we require $\Omega_\star \geq 0$, $M_{\text{dust}} \geq 0$, and $0 \leq \gamma \leq 1$. We select the dust model j_M , and intensity model $(\gamma, U_{\min}, U_{\max}, \alpha)$ giving the best fit (smallest χ^2) subject to these constraints.

For the MW dust models, there are effectively 7 adjustable parameters: Ω_\star , M_{dust} , q_{PAH} (via j_M), γ , U_{min} , U_{max} , and α . However, we will fix one of these parameters from the outset, by setting $\alpha = 2$. This choice is based on experimentation that indicated that the quality of the fit is not very sensitive to the precise value of α , with $\alpha \approx 2$ providing satisfactory fits for diverse galaxies. Therefore we start with 6 parameters to be adjusted. For the galaxies with SCUBA data, we will examine the effects of varying U_{max} , but we will see in §5.4.2 that setting $U_{\text{max}} = 10^6$ works well; therefore, the number of adjustable parameters is, effectively, 5: Ω_\star , M_{dust} , q_{PAH} , U_{min} , and γ . If the number of observed bands is N_b , the number of degrees of freedom = $(N_b - 5)$ where N_b ranges from $N_b = 9$ (e.g., NGC 0024, with 4 IRAC bands, 3 MIPS bands, and IRAS 60, 100 μm) to $N_b = 12$ (e.g., NGC 3190 with 4 IRAC bands, 3 MIPS bands, IRS 16 μm , IRAS 12,60,100 μm , and SCUBA 850 μm). To assess the goodness of fit, we calculate χ^2 per degree of freedom:

$$\chi_r^2 \equiv \frac{\chi^2}{N_b - 5} \quad . \quad (12)$$

5. SCUBA-Constrained Dust Models

5.1. Spectral Energy Distributions

The distribution of grain temperatures in a dust cloud or a galaxy is never determined precisely. At wavelength λ the thermal emission per unit dust mass $\propto [e^{hc/\lambda k T_d} - 1]^{-1}$. For $\lambda \lesssim 360 \mu\text{m} (20 \text{ K}/T_d)$, small errors in the adopted T_d lead to large errors in the dust mass inferred from the observed F_ν . For example, varying the adopted T_d from 22 to 18K produces a 150% increase in the mass of dust required to produce a given 160 μm flux, but only a 35% increase in the mass required to produce a given 850 μm flux. Observations at $\lambda \gtrsim 450 \mu\text{m}$ provide dust masses with the least sensitivity to dust temperature (for dust temperatures $T_d \gtrsim 15 \text{ K}$). Therefore, the subset of 17 SINGS-SCUBA galaxies will be those for which we can best determine the dust mass.

For each galaxy Table 4 lists the best-fit model for $10^3 \leq U_{\text{max}} \leq 10^7$, for fixed $\alpha = 2$. If the best-fit model has either LMC or SMC dust models (see NGC 5195) then we also list the parameters for the best-fit model using MW dust. Finally, if the best-fit MW dust model has $U_{\text{max}} \neq 10^6$ we also list the parameters for the best-fit MW dust model with $U_{\text{max}} = 10^6$.

Table 4. 17 SINGS Galaxies with IRAC, MIPS, and SCUBA global fluxes

galaxy	morph type	D^a Mpc	$\log[M(\text{HI})]^a$ M_\odot	$\log[M(\text{H}_2)]^a$ M_\odot	$\log(M_{\text{dust}})^b$ M_\odot	$\log(L_{\text{dust}})^b$ L_\odot	q_{PAH}^c %	$\langle U \rangle^d$	dust type	U_{min}^e	U_{max}^e	γ^f %	$f(U > 10^2)^g$ %	χ_r^{2h}
ngc0337	Sd	24.70	—	—	7.65	10.31	2.7	3.41	MW	2.5	10^4	4.96	16.8	0.21
					7.63	10.29	2.5	3.43	MW	3.0	10^6	1.23	9.9	0.43
ngc1482	S0	22.00	<8.88	9.77	7.47	10.68	2.9	11.82	MW	8.0	10^7	3.66	28.5	0.25
					7.48	10.67	3.5	11.57	MW	8.0	10^6	4.15	26.5	0.55
ngc2798	Sa	24.70	9.29	9.77	7.29	10.58	2.4	14.26	MW	8.0	10^5	9.28	36.0	0.45
					7.25	10.57	2.0	15.51	MW	10.0	10^6	5.24	31.1	0.46
ngc2976	Sc	3.56	8.12 ⁱ	8.08 ^j	6.34	8.93	3.4	2.82	MW	2.5	10^7	0.90	9.2	0.30
					6.35	8.93	3.6	2.79	MW	2.5	10^6	0.99	8.2	0.33
ngc3190	Sa	17.40	8.65	—	7.19	9.73	3.8	2.55	MW	2.5	10^7	0.15	1.7	0.38
					7.19	9.73	4.6	2.54	MW	2.5	10^6	0.14	1.3	0.39
Mark33	Im	21.70	8.77	—	6.54	9.83	1.9	14.33	MW	4.0	10^5	28.3	54.6	0.37
					6.47	9.81	1.3	15.96	MW	7.0	10^6	11.8	47.6	0.58
ngc3521	Sbc	9.00	9.75	9.79	7.83	10.32	4.5	2.26	MW	2.0	10^7	0.90	9.2	1.00
					7.84	10.32	4.5	2.24	MW	2.0	10^6	1.00	8.2	1.15
ngc3627	Sb	8.90	8.88	9.76	7.69	10.38	4.3	3.62	MW	3.0	10^5	2.20	12.6	0.74
					7.58	10.37	4.3	4.58	MW	4.0	10^6	1.28	10.3	0.77
ngc4536	Sbc	25.00	9.71	10.01	7.80	10.80	3.8	7.38	MW	5.0	10^5	5.35	25.0	0.68
					7.82	10.79	3.5	6.85	MW	5.0	10^6	3.31	22.2	0.79
ngc4569	Sab	20.00	8.80	9.97 ^j	7.75	10.30	4.0	2.60	MW	2.0	10^7	2.09	18.5	0.75
					7.76	10.30	4.4	2.55	MW	2.0	10^6	2.27	16.4	0.79
ngc4631	Sd	9.00	10.09	9.49	8.11	10.55	3.7	2.02	MW	1.0	10^3	17.2	19.7	0.33
					7.95	10.53	3.6	2.76	MW	2.5	10^6	0.89	7.4	0.48
ngc4826	Sab	5.60	8.49 ⁱ	9.03 ^j	6.89	9.66	3.0	4.35	MW	4.0	10^7	0.63	6.7	0.16
					6.89	9.66	3.1	4.32	MW	4.0	10^6	0.70	5.9	0.17
ngc5195	Im	8.20	—	8.55	6.61	9.47	2.5	5.35	MW	1.2	10^4	43.1	44.5	0.33
					6.45	9.43	2.4	7.16	MW	5.0	10^6	3.85	24.8	0.70

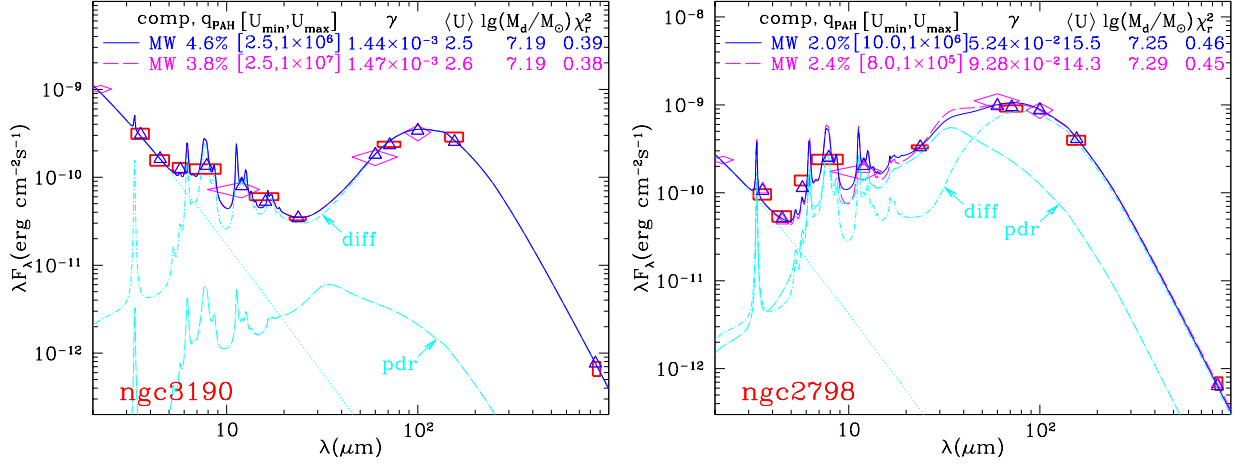


Fig. 3.— (a) SED for the SAap galaxy NGC 3190. Rectangles show observed fluxes in the IRAC, MIPS, SCUBA bands, and the IRS 16 μm band; diamonds show 2MASS 2.2 μm , and IRAS 12, 60, and 100 μm , fluxes. Vertical extent of rectangles and diamonds corresponds to $\pm 1\sigma$ range, and width corresponds to nominal width of band. Solid line shows best-fit model $U_{\text{max}} = 10^6$ model, with IRAC, MIPS, IRS 16 μm , IRAS, and SCUBA data used to constrain the fit; $N_b = 12$ for NGC 3190. Triangles show model convolved with the IRAC, MIPS, IRS 16 μm , IRAS, and SCUBA bands. Dot-dashed curves show separate contributions of starlight and emission from dust heated by $U = U_{\text{min}}$ (labelled “diff”), and dust heated by $U_{\text{min}} < U < U_{\text{max}}$ (labelled “pdr”). Long-dashed curve shows best-fit model when U_{max} is unconstrained – for this case the model spectrum is nearly indistinguishable for the simple reason that there is relatively little dust ($\gamma \approx 0.0015$), and therefore relatively little power, in the “pdr” component. (b) As for (a), but for the SBa galaxy NGC 2798, with $N_b = 11$ (global imaging in the IRS 16 μm band is unavailable).

The models are generally very successful in fitting the observed SEDs. The SED of NGC 3190, together with a model fit, appears in Figure 3a. This is an example where the model (with $U_{\text{min}} = 2.5$, $U_{\text{max}} = 10^7$, $\gamma = 1.5 \times 10^{-3}$) provides an excellent fit to the observations, with $\chi_r^2 = 0.38$. The inferred dust mass is $M_{\text{dust}} = 10^{7.19} M_\odot$, and the mean starlight intensity is estimated to be $\langle U \rangle = 2.6$. Only a small fraction $\gamma \approx 0.0015$ of the dust is in regions with starlight intensities $U > U_{\text{min}}$. Also shown in Figure 3a (solid line) is a fit with the upper cutoff fixed at $U_{\text{max}} = 10^6$. The model SED is nearly identical (the solid curve and dash-dot curves coincide in the plot) and the derived dust mass is unchanged.

Figure 3b shows the SED of NGC 2798, a galaxy where the dust is considerably warmer than in NGC 3190. The best-fit dust model ($U_{\text{min}} = 8$, $U_{\text{max}} = 10^5$, $\gamma = 0.09$) provides a good fit ($\chi_r^2 = 0.45$) to the observations, but the model with $U_{\text{max}} = 10^6$ provides nearly as good a fit ($\chi_r^2 = 0.46$), a derived dust mass differing by only 0.04 dex, and similar q_{PAH} (2.0% vs. 2.5%).

The model fits to NGC 2798 both have a noticeable “bump” near $\sim 33 \mu\text{m}$, produced by the warm graphite grains in the DL07 model. The small but nonzero conductivity for $\vec{E} \parallel c$ in graphite⁵ causes the absorption cross section C_{abs} to rise to a broad local maximum near $\sim 33 \mu\text{m}$

⁵The c -axis is normal to the sheets of hexagonally-organized C atoms.

Table 4—Continued

galaxy	morph type	D^a Mpc	$\log[M(\text{HI})]^a$ M_\odot	$\log[M(\text{H}_2)]^a$ M_\odot	$\log(M_{\text{dust}})^b$ M_\odot	$\log(L_{\text{dust}})^b$ L_\odot	q_{PAH}^c %	$\langle U \rangle^d$	dust type	U_{min}^e	U_{max}^e	γ^f %	$f(U > 10^2)^g$ %	χ_r^{2h}
ngc5713	Sbc	26.60	9.93	10.02	7.95	10.72	2.2	6.63	LMC	4.0	10^4	9.62	26.8	0.41
					7.94	10.72	3.1	4.46	MW	3.0	10^5	5.17	24.0	0.49
					7.96	10.71	2.8	4.19	MW	3.0	10^6	3.39	22.4	0.55
ngc5866	S0	12.50	<8.28	8.93	6.65	9.48	2.0	5.00	MW	5.0	10^3	0	0.0	0.97
					6.65	9.48	2.0	5.00	MW	5.0	10^6	0	0.0	0.97
ngc7331	Sb	14.72 ^k	9.96 ⁱ	10.14 ^j	8.05	10.69	4.2	3.22	MW	3.0	10^7	0.53	5.6	0.54
					8.06	10.69	4.3	3.20	MW	3.0	10^6	0.57	4.9	0.55
ngc7552	Sab	22.30	9.68	—	7.84	11.07	1.5	12.43	MW	8.0	10^7	4.24	31.5	0.50
					7.84	11.07	2.2	12.55	MW	8.0	10^6	5.30	31.1	0.63

^a D , 21 cm flux, and CO 1-0 flux from Kennicutt et al. (2003) unless otherwise noted.

^bEstimated from dust model.

^cFraction of dust mass contributed by PAHs with $N_C < 10^3$ C atoms.

^dDust-weighted mean starlight intensity.

^e U_{min} , U_{max} = lower, upper cutoff for starlight intensity scale factor U .

^fFraction of dust mass in regions with $U > U_{\text{min}}$.

^gfraction of dust luminosity from regions with $U > 10^2$

^h $\chi^2/(N_b - 5)$, where N_b = number of bands used for fitting.

ⁱ21 cm flux from Walter (2005).

^jCO 1-0 flux from Sheth et al. (2005).

^kFreedman et al. (2001).

(Draine & Lee 1984, DL07). When exposed to starlight with $U \gtrsim 10^4$, graphite grains produce a broad emission bump peaking in the 30–35 μm region, depending on U . Unfortunately, the MIPS 24 μm and 71 μm bands straddle this feature, and do not constrain it. Implications of the model 33 μm feature are discussed below in §9.3.

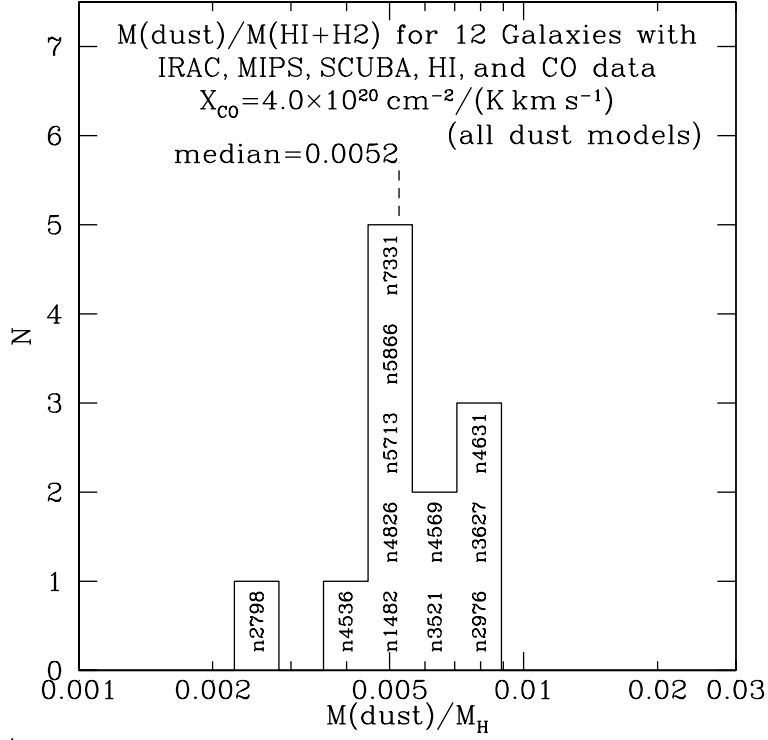


Fig. 4.— Histograms of $M_{\text{dust}}/M(\text{H I} + \text{H}_2)$ for the 12 galaxies in the sample for which both H I 21 cm and CO 1-0 have been measured, using $X_{\text{CO}} = 4 \times 10^{20} \text{ cm}^{-2} (\text{K km s}^{-1})^{-1}$ to estimate $M(\text{H}_2)$.

5.2. Dust-to-Gas Ratio

If the interstellar abundances of carbon and all heavier elements were proportional to the gas-phase oxygen abundance, and if the same fraction of the major condensible elements (C, O, Mg, Si, Fe) were in solid form as in the Milky Way, then all galaxies would be expected to conform to

$$\frac{M_{\text{dust}}}{M_{\text{H}}} \approx 0.010 \times \frac{(\text{O}/\text{H})}{(\text{O}/\text{H})_{\text{MW}}}, \quad (13)$$

where $(\text{O}/\text{H})_{\text{MW}}$ is the oxygen abundance in the local Milky Way, and the factor 0.010 is from the MW dust models in Table 3.

Table 4 gives the estimated dust mass M_{dust} for the 17 galaxies. For many of the galaxies there are measurements of 21 cm emission and CO emission from which the masses of H I and H₂

can be estimated (see Table 4). The usual assumption is made that the H_2 mass is proportional to the CO 1-0 luminosity:

$$M(\text{H}_2) = 1.57 \times 10^4 M_\odot \left(\frac{X_{\text{CO}}}{4 \times 10^{20} \text{ cm}^{-2} (\text{K km s}^{-1})^{-1}} \right) \left(\frac{D}{\text{Mpc}} \right)^2 \left(\frac{S_{\text{CO}}}{\text{Jy km s}^{-1}} \right) \quad (14)$$

where X_{CO} is the ratio of H_2 column density to antenna temperature integrated over the CO 1-0 line, and $S_{\text{CO}} \equiv \lambda_{1-0} \int F_\nu(1-0) d\nu$, where $\int F_\nu(1-0) d\nu$ is the CO 1-0 line flux. Use of the so-called CO 1-0 luminosity to estimate H_2 masses remains suspect, and the value to use for the proportionality constant X_{CO} is uncertain, with estimates for the Milky Way ranging from $3.0 \times 10^{20} \text{ cm}^{-2} (\text{K km s}^{-1})^{-1}$ (Young & Scoville 1991) to $1.56 \times 10^{20} \text{ cm}^{-2} (\text{K km s}^{-1})^{-1}$ (Hunter et al. 1997). Here we use the value $X_{\text{CO}} = 4 \times 10^{20} \text{ cm}^{-2} (\text{K km s}^{-1})^{-1}$, the value recommended by Blitz et al. (2006) for giant molecular clouds in Local Group galaxies. We discuss the value of X_{CO} in §9.4, where we argue that dust mass estimates for the SINGS galaxies favor $X_{\text{CO}} = 4 \times 10^{20} \text{ cm}^{-2} (\text{K km s}^{-1})^{-1}$.

Figure 4 shows the dust/hydrogen mass ratio for the 12 SINGS-SCUBA galaxies for which the total (atomic and molecular) gas masses are known. The derived dust-to-gas ratios are tightly clustered, with median $M_{\text{dust}}/M_{\text{H}} \approx 0.005$. The lowest dust-to-gas ratio is for NGC 2798, with $M_{\text{dust}}/M_{\text{H}} \approx 0.0023$; the highest is for NGC 2976, with $M_{\text{dust}}/M_{\text{H}} \approx 0.0089$.

The dust to gas mass ratios in Figure 4 are broadly comparable to the value ~ 0.007 estimated from gas phase abundances in the local Milky Way (Table 2) or 0.010 estimated from models for the observed Milky Way extinction (Table 3). The observed range $0.003 \lesssim M_{\text{dust}}/M_{\text{H}} \lesssim 0.01$ is consistent with galactic metallicities between $\sim 0.3\times$ and $\sim 1\times$ solar, if a similar fraction of the heavy elements is in the form of dust as in the Milky Way.

Based on Figure 4, we conclude that the model-fitting procedure provides dust mass estimates for this sample of galaxies that are in reasonable agreement with the dust masses expected if depletions are similar to depletions in the Milky Way. Furthermore, the model appears to be able to reproduce the observed emission spectrum (see, eg., Fig. 3). The metallicity dependence of the dust-to-gas ratio will be examined in §7.1.

5.3. Role of LMC and SMC Dust Models

We now ask whether it is necessary to use the LMC and SMC dust models in the determination of dust masses – do the dust models developed for the LMC and SMC lead to improved fits to the observed spectra and, if so, how different are the inferred dust masses and PAH abundances? For each galaxy in the SINGS-SCUBA subset, we searched for the model that minimized χ_r^2 ; for 16 of the 17 galaxies, a MW dust model was preferred, for NGC 5713 an LMC dust model was favored, but in no case did the SMC bar dust model give the best fit. For NGC 5713, where an LMC dust model gave the smallest χ_r^2 , we also give in Table 4 the parameters for the best-fit MW model; the

derived M_{dust} differs from that obtained using the LMC model by only 0.01 dex, and $q_{\text{PAH}} = 3.1\%$, vs. 2.2% for the LMC model; when the MW model fit is constrained to have $U_{\text{max}} = 10^6$, the derived $q_{\text{PAH}} = 2.8\%$. Therefore, at least for the 17 galaxies with SCUBA photometry, the model fitting can be limited to MW-type dust models with minimal impact on the inferred dust masses or PAH index.

In §6 below we demonstrate that we can obtain good estimates for M_{dust} and q_{PAH} even for galaxies lacking submm photometry, by limiting the search to models with $U_{\text{min}} \geq 0.7$. Here we compare estimates for q_{PAH} and M_{dust} obtained using LMC and SMC dust models with those obtained using MW dust models.

5.3.1. PAH Abundance q_{PAH}

Let $q_{\text{PAH}}(\text{MW})$ be the best-fit estimates for q_{PAH} when fitting with only MW dust models, and let $q_{\text{PAH}}(x\text{MC})$ be the estimate obtained using only LMC+SMC dust models. As discussed below (see §7.4) we exclude 4 galaxies for which q_{PAH} cannot be reliably estimated. Because the LMC and SMC dust models are limited to $q_{\text{PAH}} \leq 2.4\%$, we further limit consideration to galaxies for which $q_{\text{PAH}}(\text{MW}) \leq 2.4\%$. The MW models have $q_{\text{PAH}}(\text{MW}) \geq 0.4\%$. Therefore for the 7 galaxies where the best-fit MW model has $q_{\text{PAH}} = 0.4\%$, we can conclude only that the actual $q_{\text{PAH}} \leq 0.4\%$.

As seen in Figure 5, the best-fit MW models and the best-fit LMC+SMC models generally have similar values of q_{PAH} – 16/19 galaxies have $|q_{\text{PAH}}(\text{MW}) - q_{\text{PAH}}(x\text{MC})| \leq 0.4\%$. There is one extreme outlier: the S0 galaxy NGC 5866. NGC 5866 has relatively little dust – the flux in IRAC band 3 is consistent with starlight alone, and there is only a modest excess due to dust in IRAC band 4. As a result, q_{PAH} is not very securely determined for NGC 5866. When the fitting is limited to LMC and SMC dust models, the best fit is produced by the SMC model, with $q_{\text{PAH}} = 0.1\%$. However, this fit, with $\chi_r^2 = 1.92$, is poor compared to $\chi_r^2 = 0.97$ for the MW dust model, so the MW fit would be strongly-favored over the SMC model. Spectroscopy of the center of NGC 5866 (Smith et al. 2007) shows strong PAH emission features, consistent with the value $q_{\text{PAH}}(\text{MW}) \approx 2.0\%$.

NGC 6822 is another case of a large discrepancy between $q_{\text{PAH}} = 0.7\%$ obtained from MW models versus the value $q_{\text{PAH}} = 0.1\%$ obtained when fitting is limited to LMC,SMC dust models. Once again, the MW dust model produces a significantly better fit ($\chi_r^2 = 1.13$) than the SMC model ($\chi_r^2 = 2.04$).

For Tololo 89 (=NGC 5398), on the other hand, $q_{\text{PAH}} \leq 0.4\%$ is obtained using the MW dust models, but the best-fit LMC,SMC model is an LMC dust model with $q_{\text{PAH}} = 1.1\%$. In this case the fitting is confused by the apparent lack of dust emission in IRAC band 3, despite a strong dust excess in IRAC band 4. The MW fit has $\chi_r^2 = 2.50$, and the LMC fit has $\chi_r^2 = 2.47$ – an indication that there is something wrong with either the data or the dust model.

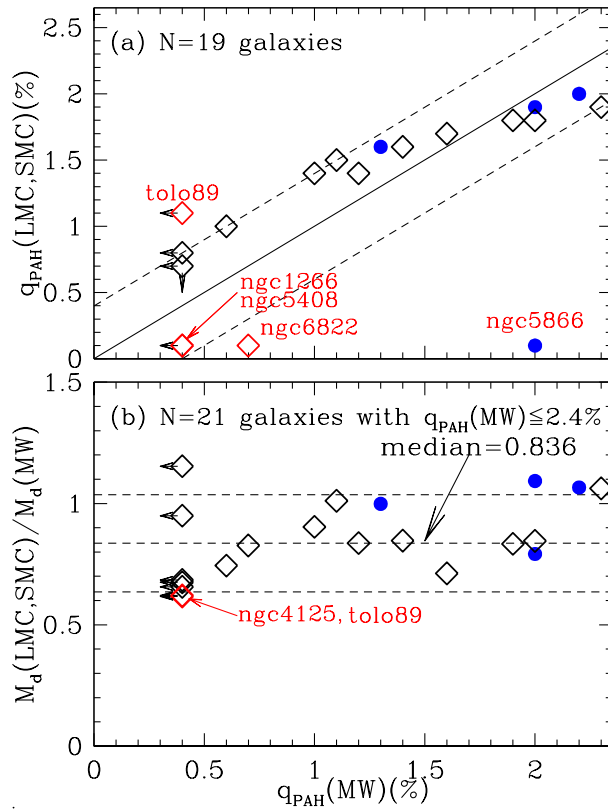


Fig. 5.— (a) q_{PAH} determined by fitting LMC or SMC models vs. q_{PAH} determined by fitting MW models, for galaxies with $q_{\text{PAH}}(\text{MW}) \leq 2.4\%$. The estimates of q_{PAH} are in good agreement: 16/19 galaxies have $|q_{\text{PAH}}(\text{MW}) - q_{\text{PAH}}(\text{xMC})| \leq 0.4\%$ (region bounded by broken lines). (b) Ratio of dust masses for best-fit LMC, SMC model and best-fit MW dust model, for galaxies with $q_{\text{PAH}}(\text{MW}) \leq 2.4\%$. The dust masses are in good agreement: the median ratio is 0.836, and 15/21 galaxies are within ± 0.20 of the median.

Since 16 of the 19 galaxies have $|q_{\text{PAH}}(\text{MW}) - q_{\text{PAH}}(\text{xMC})| \leq 0.4\%$, we conclude that the estimates for q_{PAH} are generally not sensitive to the details of the trial dust models, and restricting the fitting to the MW dust models will give reasonable results for q_{PAH} .

5.3.2. Dust Mass

Figure 5b shows, for the 21 galaxies with $q_{\text{PAH}}(\text{MW}) < 2.4\%$, the ratio of dust masses obtained using the two different dust models. The median ratio is 0.84, with 15/21 falling within the interval $M_{\text{dust}}(\text{LMC, SMC}) / M_{\text{dust}}(\text{MW}) = 0.85 \pm 0.20$. It is clear that the inferred dust mass is relatively insensitive to the details of the model dust mixture used in the modeling.

Given that we obtain similar values for the dust mass M_{dust} and the PAH abundance q_{PAH} using either the MW or the LMC+SMC dust models, we will henceforth limit the modeling to the

MW dust models. This has the advantage of providing a set of models with q_{PAH} ranging from 0.4% to 4.6% (see Table 3) allowing systematic comparisons of the level of PAH emission among different galaxies. The resulting estimates for dust masses, starlight intensity distributions should be relatively robust, and even the PAH abundances appear to also reliable to within $\Delta q_{\text{PAH}} = 0.004$. From this point on we will limit the model-fitting to the MW dust models.

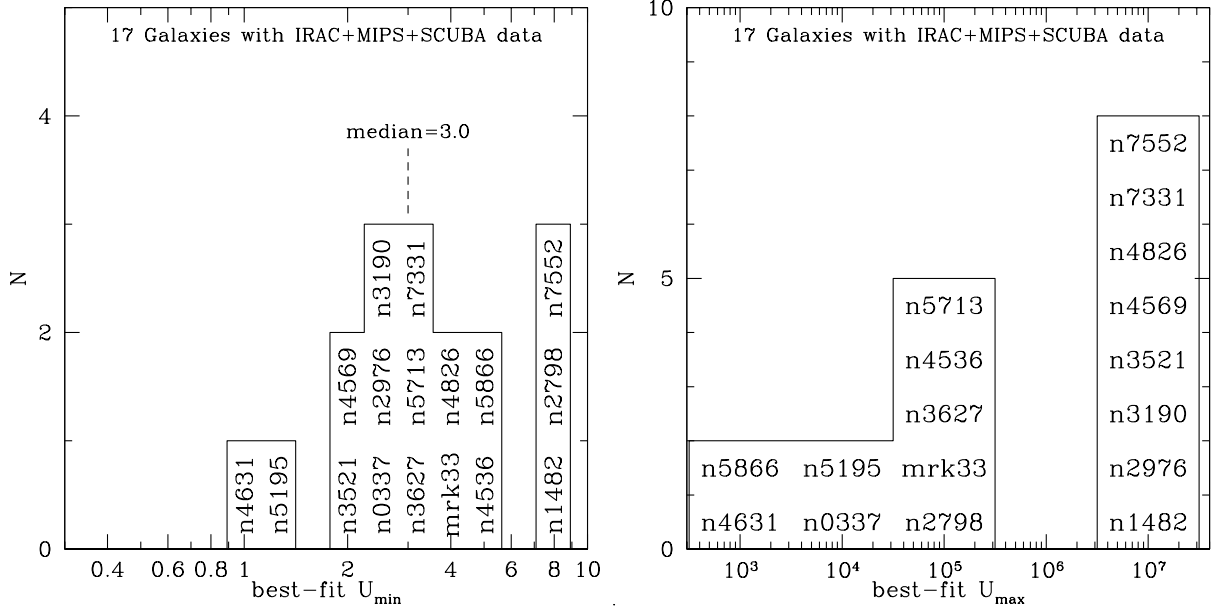


Fig. 6.— (a) Distribution of minimum starlight intensity scale factor U_{\min} . (b) Distribution of maximum starlight intensity scale factor U_{\max} . The fits were limited to MW dust models.

5.4. Radiation Field Parameters

5.4.1. Lower Cutoff U_{\min}

Figure 6a shows the distribution of the best-fit lower cutoff U_{\min} for the SINGS-SCUBA galaxies. In no case did the best-fit model have $U_{\min} < 1$, even though the model-fitting procedure considered values as small as 0.1. We therefore conclude that – at least in the SINGS-SCUBA sample – only a very small fraction of the overall FIR emission is produced by cool grains within dark clouds (grains inside dark clouds, shielded from external starlight, will have $U \ll 1$ and will be cool, unless embedded star formation is present). The $160\mu\text{m}$ and $850\mu\text{m}$ emission appears to be produced primarily by dust in diffuse regions with $U \gtrsim 1$. Cool grains in dark clouds could, in principle, contain a substantial fraction of the dust mass while contributing only a minor fraction of the total IR luminosity. However, we will see below (§9.1) that the derived mass of dust heated by starlight with $U \gtrsim 0.7$ is generally close to the value expected based on the observed total (atomic

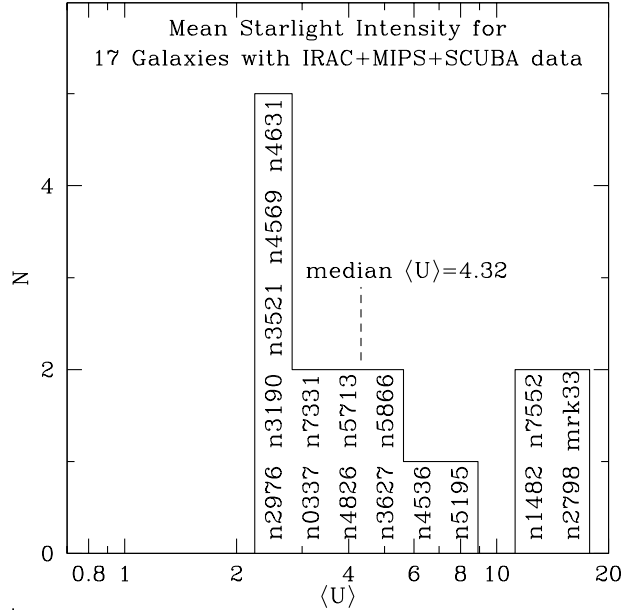


Fig. 7.— Distribution of $\langle U \rangle$ for 17 galaxies with SCUBA data (fits limited to MW dust with $U_{\max} = 10^6$, with adjustable γ and U_{\min} .)

and molecular) gas mass, indicating that the model-fitting procedure is not overlooking substantial amounts of cooler dust in dark regions.

5.4.2. Upper Cutoff U_{\max}

Figure 6b also shows that the model-fitting procedure does not strongly favor any particular value of U_{\max} . We have experimented with fixing U_{\max} , and we find that fixing $U_{\max} = 10^5$ results in only an increase in χ^2 per galaxy of 0.47, while the number of degrees of freedom per galaxy is increased by 1. Fixing $U_{\max} = 10^6$ works almost as well – the mean increase in χ^2 per galaxy is 0.70 – but fixing U_{\max} at 10^4 or 10^7 results in larger increases in average χ^2 per galaxy (in both cases > 1) relative to the fits where U_{\max} is allowed to vary.

Because of the insensitivity of the results to the precise value of U_{\max} , we will simply set $U_{\max} = 10^6$ and reduce the number of adjustable parameters from 6 to 5: Ω_* , M_{dust} , q_{PAH} , U_{\min} , and γ . Having U_{\max} as large as 10^6 is not surprising. The ultraviolet intensity in the Orion Bar photodissociation region, for example, is $\sim 3 \times 10^4$ times stronger than the local starlight background (Marconi et al. 1998; Allers et al. 2005), and the dust within compact and ultracompact H II regions, and in the surrounding PDRs, is expected to be heated by radiation fields as large as $\sim 10^6$. We therefore expect the IR spectrum of a star-forming galaxy to have a noticeable contribution from dust heated by $U \approx 10^6$. From this point onward, we will discuss only MW dust

models restricted to $U_{\max} = 10^6$.

5.4.3. Mean Intensity $\langle U \rangle$ and Fraction of Power from High-Intensity Regions

Let P_0 be the power absorbed per unit dust mass in a radiation field $U = 1$. For the intensity distribution (6) with $\alpha = 2$, the dust luminosity L_{dust} is obtained by integrating

$$dL_{\text{dust}} = U P_0 dM_{\text{dust}} = P_0 M_{\text{dust}} \left[(1 - \gamma)U \delta(U - U_{\min}) + \frac{\gamma}{U_{\min}^{-1} - U_{\max}^{-1}} U^{-1} \right] dU \quad . \quad (15)$$

Thus the total dust luminosity is

$$L_{\text{dust}} = \langle U \rangle P_0 M_{\text{dust}} \quad , \quad (16)$$

where the dust-weighted mean starlight intensity scale factor is

$$\langle U \rangle = \left[(1 - \gamma)U_{\min} + \frac{\gamma \ln(U_{\max}/U_{\min})}{U_{\min}^{-1} - U_{\max}^{-1}} \right] \quad . \quad (17)$$

Figure 7 shows the distribution of $\langle U \rangle$ for the 17 SINGS-SCUBA galaxies, fitted with MW dust models with $U_{\max} = 10^6$. These galaxies are clearly not all alike: $\langle U \rangle$ varies by a factor of 6 over the sample, from $\langle U \rangle = 2.6$ (for NGC 4569) to $\langle U \rangle = 16$ (for Mrk 33), with median $\langle U \rangle = 4.3$.

The fraction of the dust luminosity radiated from regions with $U > U_c$ (for $U_{\min} < U_c < U_{\max}$) is

$$f(L_{\text{dust}}; U > U_c) = \frac{\gamma \ln(U_{\max}/U_c)}{(1 - \gamma)(1 - U_{\min}/U_{\max}) + \gamma \ln(U_{\max}/U_{\min})} \quad . \quad (18)$$

Figure 8 shows the distribution of $f(L_{\text{dust}}; U > U_c)$ for $U_c = 10^2$ and 10^3 for the 17 galaxies with SCUBA data. The median galaxy in the SINGS-SCUBA sample has $\sim 10\%$ of the dust power originating in regions with $U > 10^2$. In extreme cases, this fraction can be considerably larger, e.g., Mrk 33, with $f(L_{\text{dust}}; U > 10^2) \approx 48\%$, and $> 30\%$ for NGC 2798 and NGC 7552. At the other extreme, the best-fit model for NGC 5866 (see §5.6.1 below) has $\gamma = 0$ and $f(L_{\text{dust}}; U > 10^2) = 0$. Values of $U \gtrsim 10^2$ are expected to arise primarily in star-forming regions where dust is found near luminous stars. The values of $f(L_{\text{dust}}; U > U_c)$ estimated from this fitting procedure are only approximate, but values of $f(L_{\text{dust}}; U > 10^2) \gtrsim 0.03$ should be indicative of significant star formation rates.

5.5. PAH Abundances

Observations with *ISO* showed that normal star-forming galaxies routinely have strong 6–9 μm PAH emission (Dale et al. 2001). This is confirmed for the present sample of 17 SINGS-SCUBA

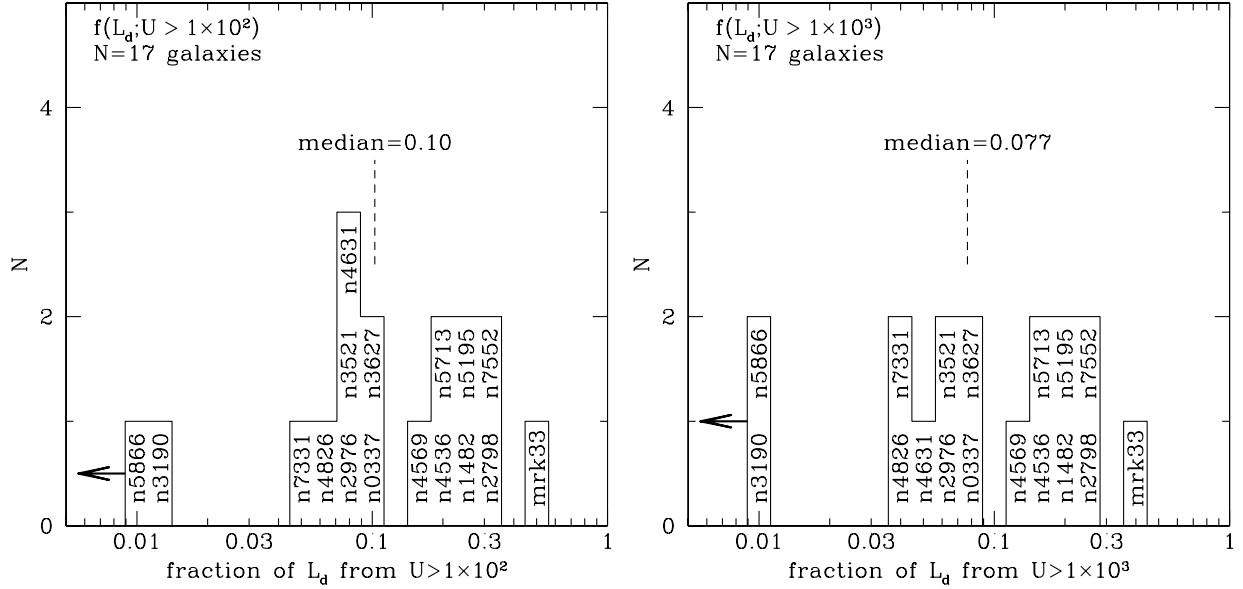


Fig. 8.— Distribution of the fraction of the dust luminosity radiated by dust exposed to starlight intensities $U > 10^2$ and $U > 10^3$. MW dust models are used for the fits, with fixed $U_{\max} = 10^6$, and adjustable γ , U_{\min} . Galaxies with $f \leq 0.01$ have been grouped in a bin at 0.01.

galaxies. Figure 9 shows a histogram of q_{PAH} for these galaxies. All of the galaxies show PAH emission, with median $q_{\text{PAH}} = 3.5\%$. None of these galaxies have $q_{\text{PAH}} < 1.3\%$. The distribution of PAH abundances over a total of 61 SINGS galaxies will be discussed in §7.4 below.

5.6. Discussion of Selected Galaxies

5.6.1. Discrepant Cases: NGC 3521 and NGC 5866

Most of the 17 galaxies in the SINGS-SCUBA sample have SEDs that are satisfactorily reproduced by the adopted dust model (see Fig. 3). If we consider only MW dust models, with fixed $U_{\max} = 10^6$, the 17 galaxies have median $\chi_r^2 = 0.55$; 16/17 of the galaxies have $\chi_r^2 < 1$. The SINGS-SCUBA galaxies with the worst fits (largest χ_r^2) are NGC 3521 ($\chi_r^2 = 1.37$), and NGC 5866 ($\chi_r^2 = 0.97$). Here we consider why the model has difficulty fitting these two galaxies.

In the case of NGC 3521, the best-fit model underpredicts the $7.9\mu\text{m}$ emission, but the more significant discrepancies are at long wavelengths, where the model is high at $71\mu\text{m}$, low at $160\mu\text{m}$ and high at $850\mu\text{m}$. To illustrate the difficulty with reproducing these three fluxes, Figure 10 also shows a single-temperature component with a ν^2 opacity with the temperature and power chosen to fit the 71 and $160\mu\text{m}$ data. Note that even this single-temperature component is too “broad” – it exceeds the $850\mu\text{m}$ datum. If a range of dust temperatures is present, it will broaden the spectrum,

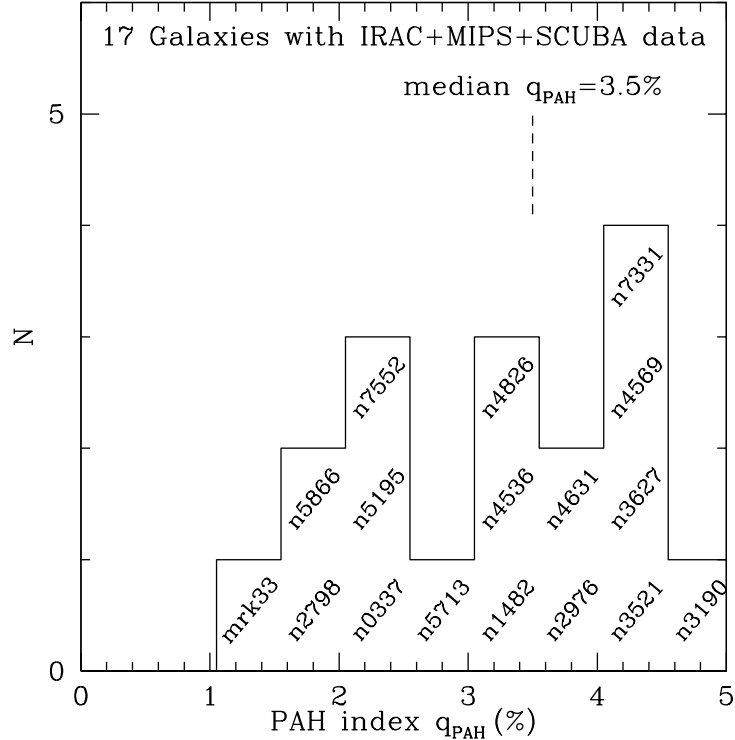


Fig. 9.— PAH index for 17 galaxies with SCUBA data, estimated by fitting MW dust models, with U_{max} allowed to vary.

and worsen the fit. Either there is a problem with some of the photometric data, or the dust in this galaxy has an opacity that is steeper than ν^2 .

The second-worst fit is for NGC 5866, an S0 galaxy with a substantial edge-on disk, and the lowest value of $\langle \nu F_\nu \rangle_{24} / \langle \nu L_\nu \rangle_{71}$ among the SINGS-SCUBA galaxies (see Fig. 1). The best-fit model has $\gamma = 0$ – all of the dust is exposed to starlight with intensity $U = U_{\text{min}} = 5$. The small value of γ is presumably because the illumination of the dusty disk is dominated by the distributed old stellar population, with little contribution from star formation in the disk. This is consistent with nondetection of $\text{H}\alpha$, with $\text{SFR} < 0.1 M_\odot \text{ yr}^{-1}$ (Kennicutt et al. 2003) (although dust extinction may also be important). The nuclear spectrum of NGC 5866 (Smith et al. 2007) includes ionic emission lines (e.g., [Ne II], [Si II], [S III]) but they are relatively weak, consistent with only low levels of star formation; the low ratio [S III]/[Si II] flux ratio also suggests a deficiency of massive stars.

Roberts et al. (1991) estimated the dust mass to be $1.4 \times 10^6 M_\odot$ (for our adopted distance of 12.5 Mpc). Here we estimate the dust mass to be $4.5 \times 10^6 M_\odot$ – larger by a factor three. Our estimate for M_{dust} results in $M_{\text{dust}}/M_{\text{H}} \approx 0.005$, consistent with $A_{\text{O}} \equiv \log_{10}(\text{O}/\text{H}) + 12 = 8.43 \pm 0.18$ (Moustakas et al. 2007), $\sim 55\%$ of solar ($(A_{\text{O}})_{\odot} = 8.69$ from Table 2).

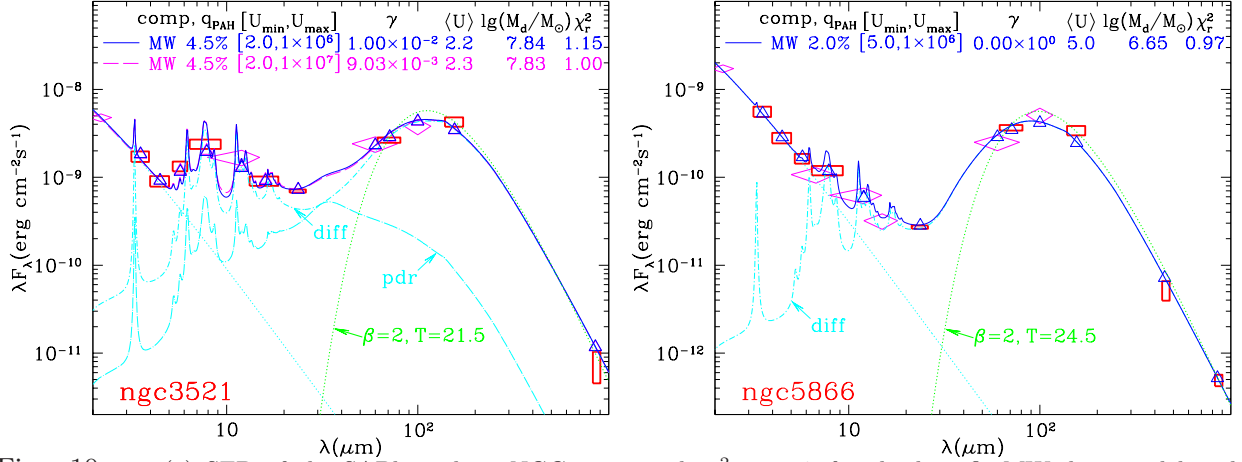


Fig. 10.— (a) SED of the SABbc galaxy NGC 3521, with $\chi_r^2 = 1.37$ for the best-fit MW dust model with $U_{\text{max}} = 10^6$. The dotted curve shows emission from hypothetical $T = 21.5 \text{ K}$ dust with $\kappa_\nu \propto \nu^2$, showing that dust with $\kappa_\nu \propto \nu^2$ cannot reproduce the observed $160 \mu\text{m}$ emission without exceeding either the $71 \mu\text{m}$ flux (if $T > 21.5 \text{ K}$) or the $850 \mu\text{m}$ flux (if $T < 21.5 \text{ K}$). Curves labelled “diff” and “pdr” show contributions of dust heated by $U = U_{\text{min}}$ and $U > U_{\text{min}}$, respectively, for the MW model with $U_{\text{max}} = 10^6$. (b) SED for the S0 galaxy NGC 5866. The best-fit MW dust model – with a single starlight intensity $U = 5$ – has $\chi_r^2 = 0.97$. The model has difficulty reproducing the sharpness of the peak in λF_λ near $100 \mu\text{m}$ and overestimates the flux at $450 \mu\text{m}$.

Once again, the difficulty is in fitting the long-wavelength data. In this case, a single-temperature $T = 24.5 \text{ K}$ component with a ν^2 opacity can fit the 71 , 160 , and $850 \mu\text{m}$ photometry, but exceeds the $450 \mu\text{m}$ datum. Once again, a distribution of temperatures would exacerbate this problem, indicating either problems with the photometry or requiring an opacity substantially steeper than ν^2 between 160 and $450 \mu\text{m}$.

5.6.2. Markarian 33

The dwarf starburst galaxy Mrk 33 (see Fig. 11) has the highest value of $\langle \nu F_\nu \rangle_{24} / \langle \nu F_\nu \rangle_{71}$ among the SINGS-SCUBA galaxies (see Fig. 1). $\text{H}\alpha$ observations of Mrk 33 indicate a $\text{SFR} \approx 1.5 M_\odot \text{ yr}^{-1}$, giving it the third-highest $\text{SFR}/L_{\text{opt}}$ ratio in the SINGS sample (Kennicutt et al. 2003). The best-fit $U_{\text{max}} = 10^6$ model has a very high mean starlight intensity $\langle U \rangle \approx 16$, and $f(L_{\text{dust}}; U > 10^2) \approx 48\%$, the highest value in the sample.

6. Estimating Dust Masses Without Submm Data

Thus far we have been fitting dust models constrained by IRAC, MIPS, IRAS, and at least one submm flux measured by SCUBA. Unfortunately, submillimeter observations are unavailable at this time for most of the SINGS galaxies. How well can dust masses be estimated in the absence of submm constraints?

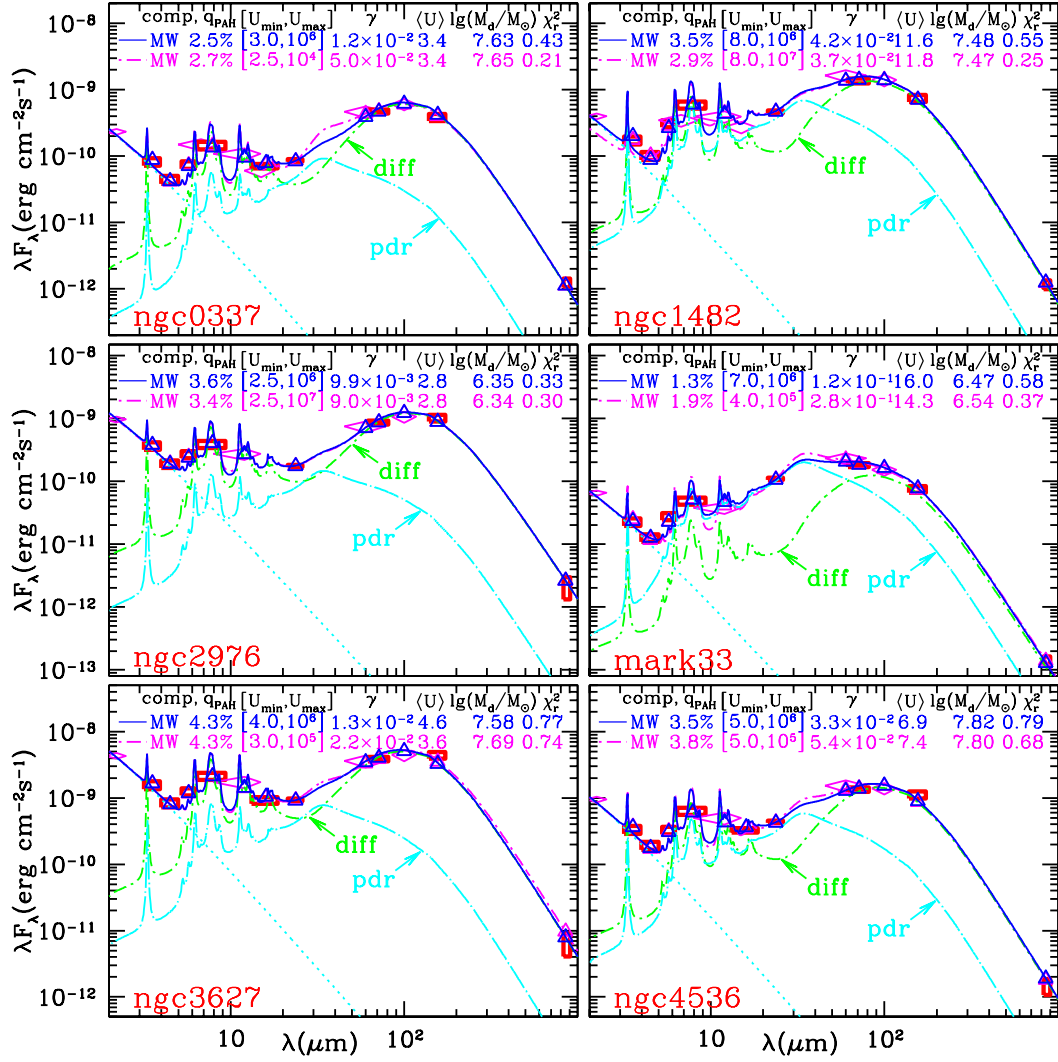


Fig. 11.— Observed fluxes and model emission spectra for galaxies with IRAC, MIPS, and IRAS data, and at least one submm flux measured by SCUBA. Some galaxies (e.g., NGC 3627) have also been measured in the IRS 16 μ m pickup filter. Rectangles and diamonds show observed fluxes; vertical extent is $\pm 1\sigma$. Curves show models fitted to IRAC, MIPS, SCUBA, and IRAS 12, 60, and 100 μ m data; triangles are models convolved with bandpass used for observations. Solid curves are models with MW dust and $U_{\max} = 10^6$; broken curves are used for other models that for some galaxies give smaller χ_r^2 (see text). Dashed-dotted curves show separate contributions of stars, dust with $U = U_{\min}$ (labeled “diff”) and dust with $U > U_{\min}$ (labeled “pdr”). See Fig. 3 for NGC 2798 and 3190, and Fig. 10 for NGC 3521 and NGC 5866.

To address this question, we first repeat the dust modeling procedure used in §5 for the 17 SINGS-SCUBA galaxies, *but with the SCUBA data omitted*. The dust masses so obtained are shown in Figure 12, where they are plotted versus the dust masses estimated when SCUBA data are also used to constrain the models.

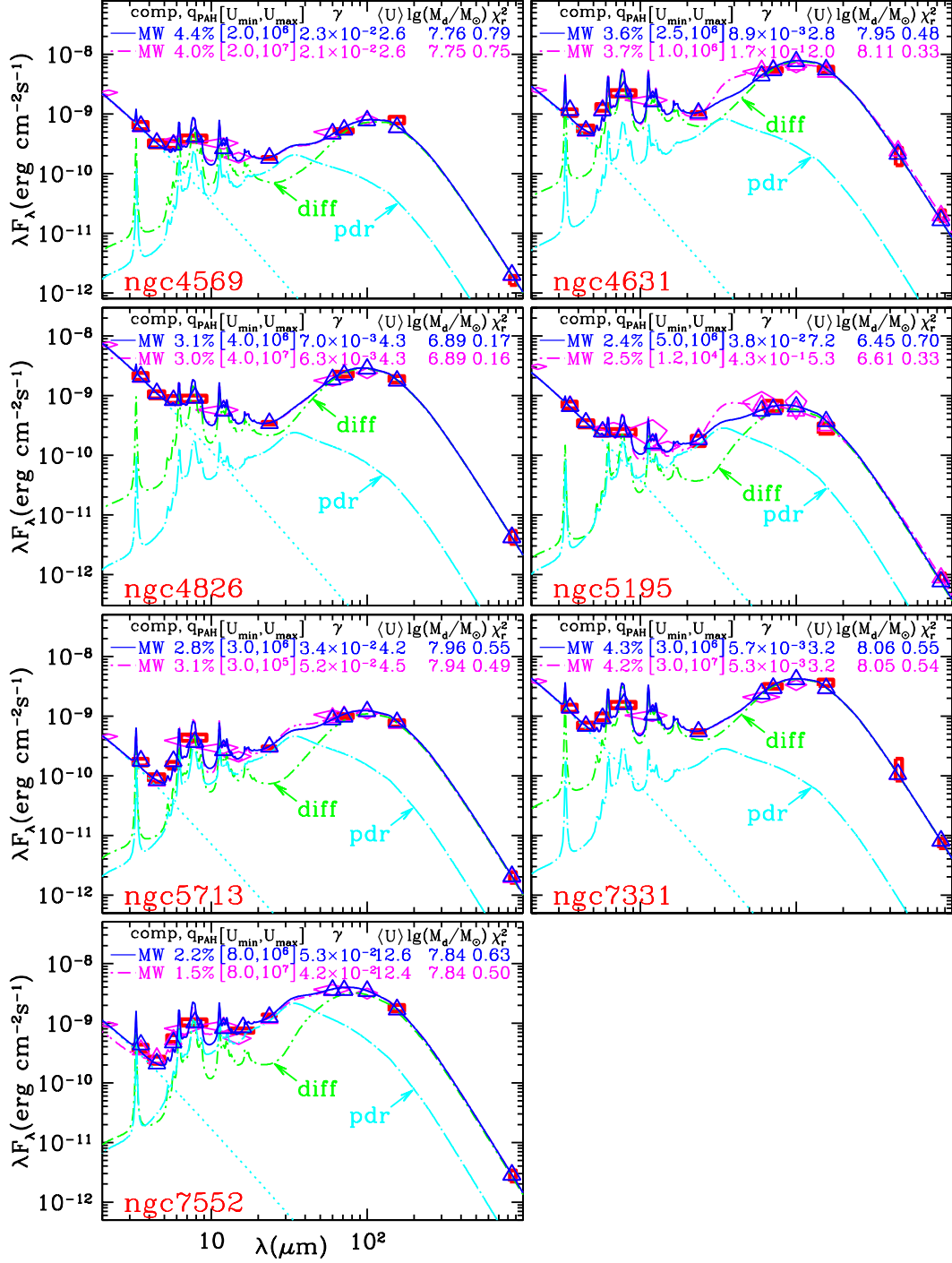


Fig. 11, continued.

If the dust masses obtained with the SCUBA fluxes included are regarded as our “gold standard”, it is clear that dropping the SCUBA data from the fitting procedure leads to substantial

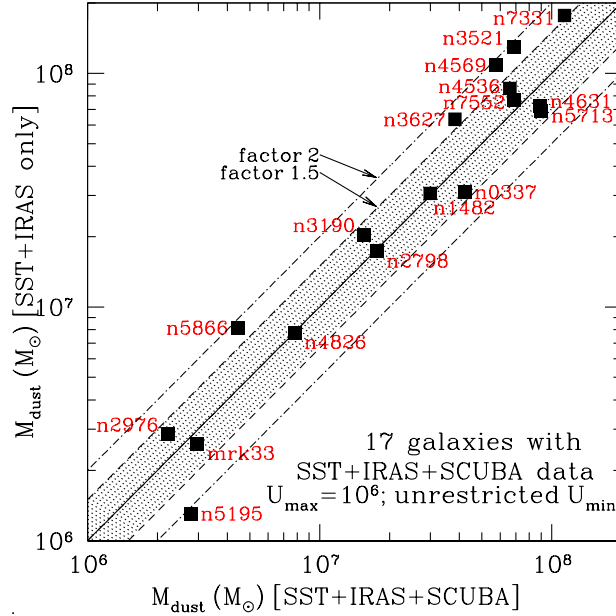


Fig. 12.— Dust mass M_{dust} determined for 17 galaxies using IRAS and SST data only, vs. the masses derived using IRAS, SST, and SCUBA data combined. Data are fit by MW dust models with $U_{\text{max}} = 10^6$ but no restriction on U_{min} . Without SCUBA data, cool dust is not strongly constrained. Nevertheless, 11/17 of the galaxies fall within a factor 1.5 of the value obtained when SCUBA data are employed, and all 17 galaxies are within a factor of 2.2.

uncertainties in the model fitting. Five of the 17 galaxies have estimated dust masses that exceed the “gold standard” estimate by more than a factor of 1.5 (NGC 3521, NGC 3627, NGC 4536, NGC 4569, and NGC 7331). In five cases the dust mass estimate is lowered when the SCUBA data are not used, in one case by a factor of more than 1.5 (NGC 5195).

Figure 13 shows estimated dust-to-gas mass ratios for the 17 galaxies with SCUBA data for which the gas mass is known. Figure 13a shows the dust/gas ratios estimated when the SCUBA fluxes are used in the fitting: the median dust/hydrogen mass ratio is 0.0053 for this sample, comparable to the value ~ 0.007 expected for solar-metallicity material with $\sim 2/3$ of the C, and most of the Mg, Si, and Fe incorporated into carbonaceous and silicate material (see Table 2). Figure 13b shows the effect of fitting the SED without using the SCUBA data – for most of the galaxies, the estimated dust/hydrogen ratio rises modestly, with a median value of only 0.0077.

Because these models reproduce the SED fairly well, and the IR power is mainly shortward of $200\,\mu\text{m}$, the total IR power is relatively unaffected when the SCUBA data are removed. What is changing is the estimated mean dust-weighted starlight intensity, with $\langle U \rangle$ often falling a factor ~ 1.5 or more below the value obtained when the SCUBA data are employed. In the absence of submm measurements to constrain the mass of cool dust, there is a risk that the model-fitting procedure may invoke a large mass of cool dust, heated by weak starlight. To prevent this, when submm data are unavailable we will restrict the model-fitting to use radiation fields with $U_{\text{min}} \geq 0.7$.

This of course runs the risk of underestimating the dust mass if there are galaxies without submm (e.g., SCUBA) observations which actually contain large amounts of cool dust heated by starlight with $U \lesssim 0.5$. However, we note that all the galaxies with SCUBA data had $U_{\min} \geq 1$ for the best-fit model (see Fig. 6a).

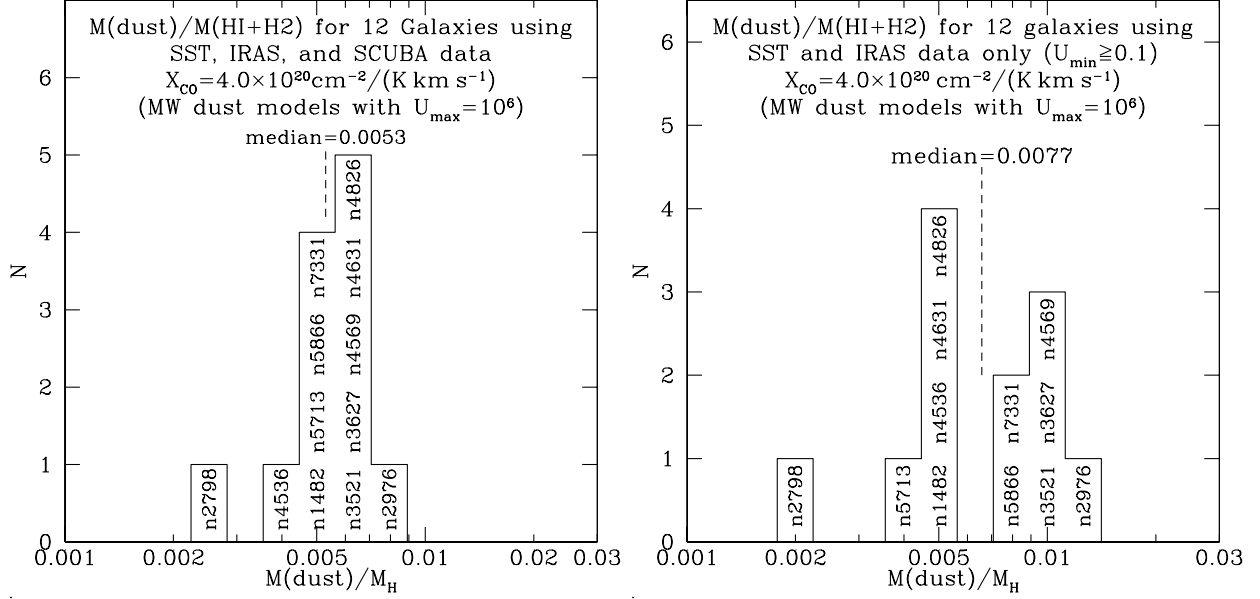


Fig. 13.— (a) Histogram of $M_{\text{dust}}/M_{\text{H}}$ obtained using IRAC+MIPS+SCUBA data for 12 galaxies for which H I 21cm and CO 1-0 fluxes have been measured. (b) Same as (a), but estimated without using SCUBA data, with $U_{\max} = 10^6$ but no restrictions on U_{\min} .

Based on the above discussion, we adopt the following “restricted” fitting procedure when submm data are unavailable:

1. Models limited to MW dust models only, with $0.4 \leq q_{\text{PAH}} \leq 4.6\%$;
2. $U_{\max} = 10^6$;
3. $\alpha = 2$;
4. $0.7 \leq U_{\min} \leq 25$.

This restricted fitting procedure (with $U_{\min} \geq 0.7$) of course implies that the resulting fits will necessarily have $\langle U \rangle \geq 0.7$. This is generally consistent with what we observe for the sample of 17 galaxies with SCUBA data – as seen in Figure 7, these galaxies tend to have $\langle U \rangle \gtrsim 2$. However, the SINGS-SCUBA galaxy sample may be biased in favor of increased dust mass and associated star formation. If other galaxies have very low mean starlight intensities $\langle U \rangle$, the restricted fitting procedure adopted here would *underestimate* the dust mass (because it would overestimate $\langle U \rangle$) To study the dust in such galaxies, submm observations are essential.

7. Dust Properties for 65 SINGS Galaxies

7.1. Dust to Gas Mass Ratio

For 48 galaxies in the SINGS sample we have complete IRAC and MIPS data, but no SCUBA fluxes. Dust masses have been estimated for these galaxies using the restricted fitting procedure described above. The SEDs for these galaxies, together with the best-fit models, are given in Appendix A (Fig. 24). The results for the dust mass M_{dust} are given in Table 5.

For 20 of these galaxies both H I 21cm and CO 2.6mm fluxes have been detected (or there is a strong upper limit on the CO flux), and we are able to estimate the total gas mass. For another 24 galaxies H I 21cm has been measured, but the CO 2.6mm flux is unknown, so we have only a lower limit on the gas mass. For 4 galaxies (the E galaxies NGC 0855 and NGC 4125, and the S0 galaxies NGC 1266 and NGC 1316) neither H I nor CO have been detected.

Figure 14 shows the distribution of $M_{\text{dust}}/M_{\text{H}}$ for the 20 galaxies lacking SCUBA data for which M_{H} is known. The distribution looks similar to the distribution in Figure 13b, except for two galaxies – IC 2574 and NGC 4236 – with $M_{\text{dust}}/M_{\text{H}} \approx 0.0005$. Note, however, that many of the sample galaxies do not appear on the histogram because M_{H} is not known.

The dust-to-gas mass ratio reflects the enrichment of the gas by heavy elements (C, O, Mg, Si, Fe) produced in stars, the production and growth of solid grains from these elements in supernovae, stellar winds, and in the interstellar medium, and destruction of grains by supernova blastwaves and other violent events in the interstellar medium.

If the same fraction of the condensible elements (C, Mg, Si, Fe, ...) is in grains as in the local Milky Way, then $M_{\text{dust}}/M_{\text{H}}$ should conform to eq.(13). However, it is possible that in some other galaxies, the balance between grain formation and destruction may be such that most interstellar C, Mg, Si and Fe is in the gas rather than in grains. We therefore expect eq. (13) to define an upper envelope to the dust-to-gas mass ratio.

Table 5. 48 SINGS Galaxies with IRAC and MIPS global fluxes, but no SCUBA data^a

galaxy	morph type	D^b Mpc	$\log[M(\text{HI})]^b$ M_\odot	$\log[M(\text{H}_2)]^{b,c}$ M_\odot	$\log(M_{\text{dust}})^o$ M_\odot	$\log(L_{\text{dust}})^o$ L_\odot	q_{PAH}^p %	$\langle U \rangle^q$	dust type	U_{min}^r	γ^s %	$f(U > 10^2)^t$ %	χ_r^{2u}
ngc0024	Sc	8.20	9.07	—	6.54	8.78	3.1	1.26	MW	1.2	0.40	3.5	0.43
ngc0628	Sc	11.40	9.97 ^d	9.64 ^e	8.02	10.29	4.3	1.36	MW	1.2	1.04	8.4	0.37
ngc0855	E	9.60	—	—	5.69	8.58	1.6	5.70	MW	5.0	1.25	10.1	1.29
ngc0925	Sd	10.10	9.75 ^d	9.18	7.35	9.71	2.9	1.67	MW	1.5	0.94	7.7	0.76
ngc1097	Sb	16.90	10.03	—	8.37	10.81	3.1	2.01	MW	1.5	2.72	18.7	0.24
ngc1266	S0	31.30	—	—	7.05	10.44	0.4	18.17	MW	15.0	2.09	15.9	0.76
ngc1291	S0/a	9.70	9.19	—	7.34	9.38	2.5 ^k	0.81	MW	0.7	1.17	9.4	1.76
ngc1316	S0	26.30	<8.87	—	7.63	10.03	0.4 ^k	1.82	MW	1.5	1.71	13.0	0.77
ngc1512	Sa	10.40	9.77	—	7.21	9.45	3.8	1.28	MW	1.2	0.55	4.7	0.57
ngc1566	Sbc	18.00	10.01	—	8.25	10.62	4.0	1.72	MW	1.5	1.20	9.6	0.54
ngc1705	Im	5.10 ^f	8.02 ^{d,f}	—	4.86	7.89	0.6	7.72	MW	7.0	0.94	7.9	0.91
ngc2403	Scd	3.50	9.48 ^d	8.01	7.08	9.56	3.5	2.22	MW	2.0	0.90	7.5	0.62
holmbII	Im	3.39 ^l	8.77 ^d	—	5.07	7.90	0.4	4.92	MW	4.0	2.01	15.1	4.13
ddo053	Im	3.56	7.78 ^d	—	4.00	7.08	1.1	8.95	MW	7.0	2.56	18.4	0.48
ngc2841	Sb	9.80	9.62 ^d	9.45	7.74	9.73	4.3	0.72	MW	0.7	0.21	1.8	0.66
ngc2915	Im	2.70	8.25	—	4.14	7.33	1.4	11.22	MW	10.0	1.16	9.6	0.37
holmbI	Im	3.84 ^l	8.15 ^d	—	4.83	7.16	1.2	1.58	MW	1.5	0.40	3.5	0.76
ngc3049	Sab	19.60	9.10	—	6.74	9.58	2.9	5.13	MW	3.0	6.06	32.6	0.38
ngc3031	Sab	3.50	9.53 ^d	—	7.53	9.66	4.0	1.00	MW	1.0	0	0.0	0.33
ngc3184	Scd	8.60	9.26 ^d	9.11	7.70	9.76	4.5	0.86	MW	0.8	0.53	4.6	0.47
ngc3198	Sc	9.80	9.71 ^d	—	7.42	9.63	3.7	1.20	MW	1.0	1.58	12.1	0.48
ic2574	Sm	4.02 ^l	9.17 ^d	6.85 ^j	5.86	8.36	0.4	2.30	MW	2.0	1.22	9.8	0.60
ngc3265	E	20.00	8.24	—	6.17	9.47	2.8	14.81	MW	10.0	4.58	28.5	0.14
ngc3351	Sb	9.30	9.01 ^d	8.98	7.46	9.89	3.2	1.95	MW	1.5	2.42	17.1	0.56
ngc3621	Sd	6.20	9.79 ^d	—	7.38	9.85	4.5	2.19	MW	2.0	0.78	6.5	0.68
ngc3773	S0	12.90	7.99	—	5.90	8.86	2.3	6.82	MW	5.0	3.25	22.0	0.40
ngc3938	Sc	12.20	9.57	9.61	7.69	9.94	4.6	1.30	MW	1.2	0.67	5.7	0.44
ngc4125	E	21.40	—	—	6.38	9.07	0.4 ^k	3.59	MW	3.0	1.69	13.0	0.38

Table 5—Continued

galaxy	morph type	D^b Mpc	$\log[M(\text{HI})]^b$ M_\odot	$\log[M(\text{H}_2)]^{b,c}$ M_\odot	$\log(M_{\text{dust}})^o$ M_\odot	$\log(L_{\text{dust}})^o$ L_\odot	q_{PAH}^p %	$\langle U \rangle^q$	dust type	U_{min}^r	γ^s %	$f(U > 10^2)^t$ %	χ_r^{2u}
ngc4236	Sdm	4.45 ^l	9.44	<8.65	6.15	8.67	1.0	2.41	MW	2.0	1.68	12.9	1.71
ngc4254	Sc	20.00	9.86	10.42	8.55	10.91	4.5	1.68	MW	1.5	0.96	7.9	0.72
ngc4321	Sbc	20.00	9.67	10.32	8.57	10.82	4.2	1.33	MW	1.2	0.85	7.1	0.39
ngc4450	Sab	20.00	8.61	9.45	7.78	9.78	2.4	0.73	MW	0.7	0.36	3.1	0.30
ngc4559	Scd	11.60	10.05	—	7.57	9.92	3.4	1.64	MW	1.5	0.73	6.1	0.69
ngc4579	Sb	20.00	8.91	9.75	8.18	10.25	3.5	0.86	MW	0.8	0.58	5.0	1.37
ngc4594	Sa	9.25 ^g	8.43	8.65 ^h	7.56	9.55	3.7 ^k	0.72	MW	0.7	0.24	2.1	1.00
ngc4625	Sm	9.50	9.02	—	6.35	8.81	4.4	2.13	MW	2.0	0.53	4.6	0.22
ngc4725	Sab	17.10	9.87	9.95	8.20	10.18	4.5	0.71	MW	0.7	0.16	1.4	0.57
ngc4736	Sab	5.30	8.71 ^d	9.05	7.11	9.89	4.1	4.37	MW	4.0	0.81	6.8	0.33
ngc5033	Sc	13.30	9.97	9.66	7.95	10.28	4.1	1.61	MW	1.5	0.58	5.0	0.35
ngc5055	Sbc	8.20	9.78 ^d	9.77	8.19	10.35	4.1	1.06	MW	1.0	0.48	4.1	0.31
ngc5194	Sbc	8.20	9.43 ^d	10.03	8.26	10.61	4.5	1.66	MW	1.5	0.84	7.0	0.40
tolo89	Sdm	15.00	9.11	—	6.46	9.15	0.4	3.55	MW	2.0	6.41	33.2	2.50
ngc5408	Im	4.81 ^m	8.51	—	4.67	8.28	0.4	29.45	MW	20.0	4.81	30.1	2.12
ngc5474	Scd	6.90	9.10	—	6.39	8.74	1.9	1.63	MW	1.5	0.71	6.0	0.46
ic4710	Sm	8.50	8.51	—	5.71	8.60	2.0	5.73	MW	5.0	1.30	10.4	0.49
ngc6822	Im	0.49 ⁿ	8.13	—	5.04	7.62	0.7	2.77	MW	2.5	0.89	7.4	1.13
ngc6946	Scd	5.50	9.37 ⁱ	9.77	7.74	10.35	4.3	3.03	MW	2.5	1.77	13.5	0.51
ngc7793	Sd	3.20	8.77 ^d	—	6.92	9.14	3.6	1.25	MW	1.2	0.31	2.7	0.85

^a All models assume MW dust, with $U_{\text{max}} = 10^6$.

^b D , 21 cm flux, and CO 1-0 flux from Kennicutt et al. (2003) unless otherwise noted.

^c $M(\text{H}_2)$ calculated using $X_{\text{CO}} = 4 \times 10^{20} \text{ cm}^{-2} (\text{K km s}^{-1})^{-1}$

^d 21 cm flux from Walter (2005)

^e CO 1-0 flux from Sheth et al. (2005)

^f Tosi et al. (2001)

^g D is weighted mean of Ford et al. (1996) and Ajhar et al. (1997)

^h CO 1-0 flux from Bajaja et al. (1991)

Models have been proposed to attempt to predict the dust-to-gas ratio in galaxies as they evolve in metallicity (Dwek 1998; Lisenfeld & Ferrara 1998; Edmunds 2001; Hirashita et al. 2002). James et al. (2002) compared models to dust masses estimated from IR and submm observations, and argued that the fraction of the metals condensed into dust grains appeared to be the same in dwarf and giant galaxies – i.e., dust-to-gas mass ratios consistent with eq. (13) – for $8.1 \lesssim A_O \lesssim 9.0$.

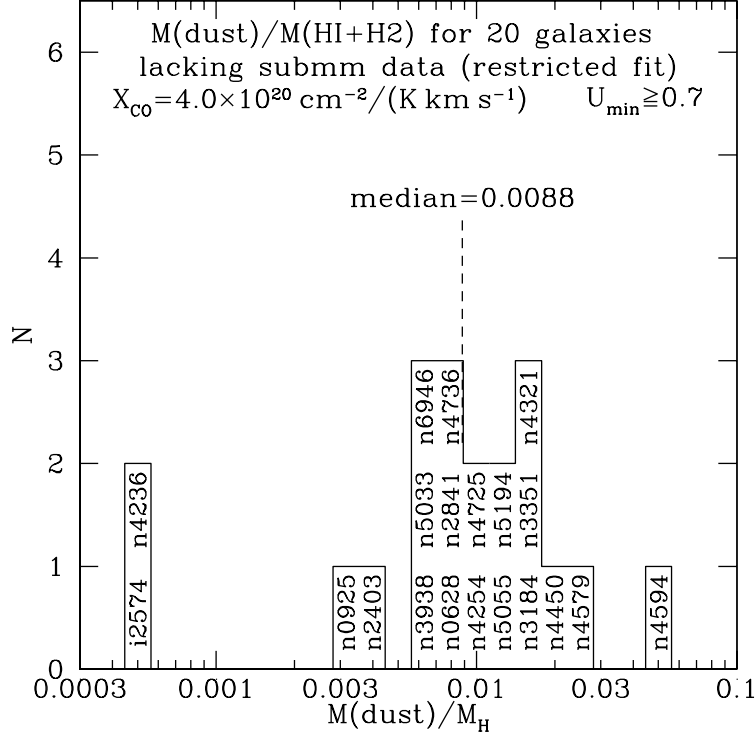


Fig. 14.— Dust to H mass ratio determined from IRAC + MIPS data only, using restricted fits with $U_{\min} \geq 0.7$, and taking $X_{\text{CO}} = 4 \times 10^{20} \text{ cm}^{-2} (\text{K km s}^{-1})^{-1}$.

Galliano et al. (2003, 2005) estimated the dust masses for 4 dwarf galaxies, and found that NGC 1569 and He 2-10 had $M_{\text{dust}}/M_{\text{H}}$ a factor of 4–7 and 2–10, respectively, below eq. (13). Hunt et al. (2005) used IR and submm observations to estimate dust masses for a sample of seven low-metallicity blue compact dwarfs. For SBS 0335-052, with metallicity $A_O = 7.29 \pm 0.01$ (Izotov & Thuan 1998), Hunt et al. (2005) found an extremely low dust-to-gas mass ratio $M_{\text{dust}}/M_{\text{H}} \approx 10^{-7}$, far below the value $\sim 2 \times 10^{-4}$ given by eq. (13). The results of Galliano et al. (2005) and Hunt et al. (2005) are clearly inconsistent with the conclusion of James et al. (2002) that dwarf galaxies have the same dust-to-metals ratio as the Milky Way.

Figure 15a,b shows how $M_{\text{dust}}/M_{\text{H}}$ correlates with oxygen abundance for the SINGS galaxy

Table 5—Continued

galaxy	morph type	D^b Mpc	$\log[M(\text{HI})]^b$ M_\odot	$\log[M(\text{H}_2)]^{b,c}$ M_\odot	$\log(M_{\text{dust}})^o$ M_\odot	$\log(L_{\text{dust}})^o$ L_\odot	q_{PAH}^p %	$\langle U \rangle^q$	dust type	U_{min}^r	γ^s %	$f(U > 10^2)^t$ %	χ_r^{2u}
ⁱ 21 cm flux for radius $< 6'$ from Boulanger & Viallefond (1992)													
^j CO 1-0 flux from Leroy et al. (2005)													
^k q_{PAH} very uncertain – see §7.4													
^l Karachentsev et al. (2002a)													
^m Karachentsev et al. (2002b)													
ⁿ Cannon et al. (2005)													
^o Estimated from dust model.													
^p Fraction of dust mass contributed by PAHs with $N_C < 10^3$ C atoms.													
^r Lower cutoff for starlight intensity scale factor U .													
^s Dust-weighted mean starlight intensity scale factor.													
^t Fraction of dust luminosity from regions with $U > 10^2$													
^u $\chi^2/(N_b - 5)$, where N_b = number of bands used for fitting.													

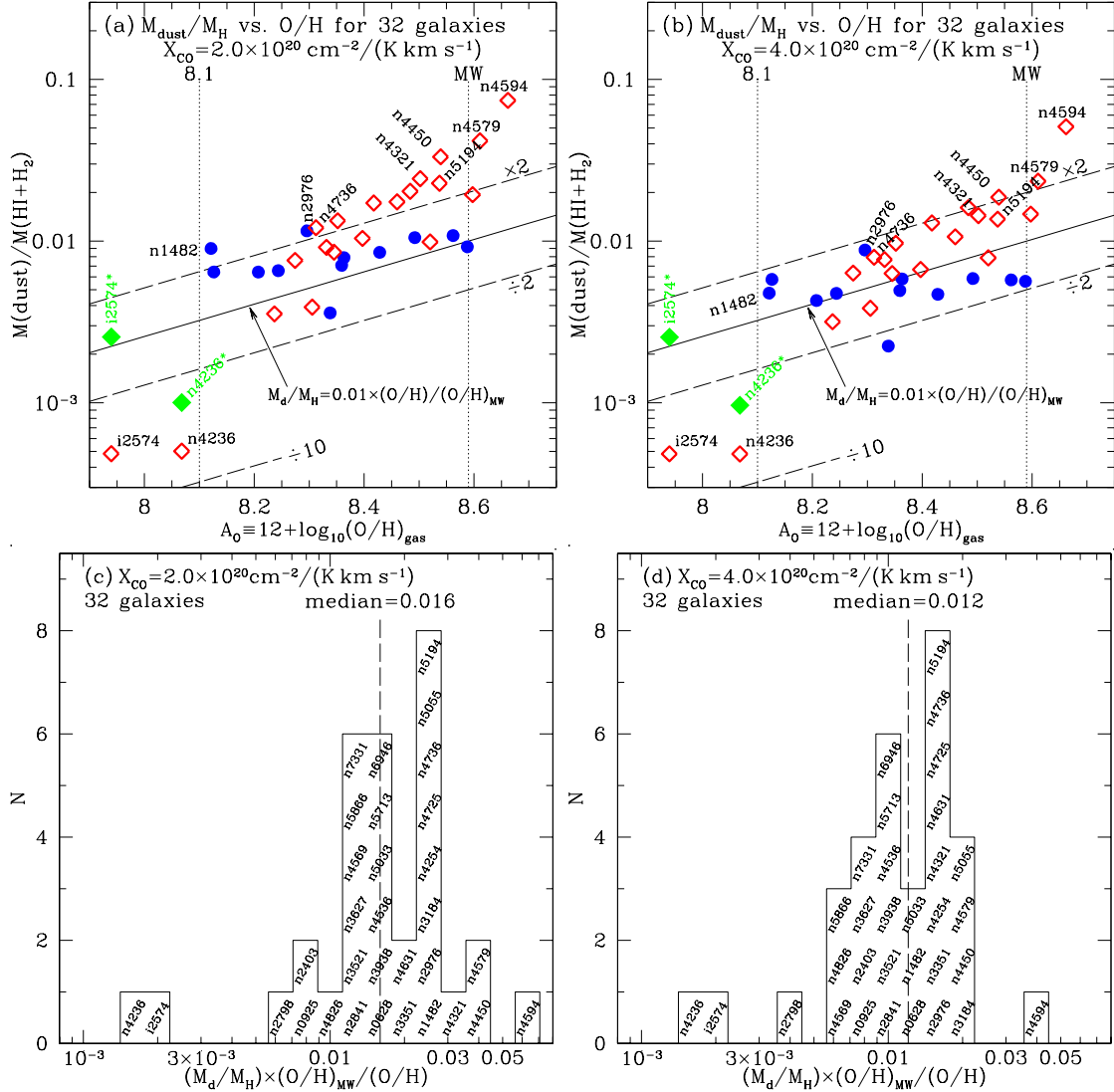


Fig. 15.— Ratio of M_{dust} to M_{H} vs. oxygen abundance (see text) for galaxies with and without SCUBA fluxes (circles and diamonds, respectively), showing 32 galaxies where gas mass is known, for two values of $X_{\text{CO}}/[\text{cm}^{-2}(\text{K km s}^{-1})^{-1}]$: (a) 2×10^{20} , and (b) 4×10^{20} . Filled diamonds: $M_{\text{dust}}/M_{\text{H}}$ for regions where IR emission is detected (see text). Solid line shows eq. (13); broken lines show factor of 2 variations around the solid line. Histogram of normalized dust-to-gas mass ratio for $X_{\text{CO}}/[\text{cm}^{-2}(\text{K km s}^{-1})^{-1}] = 2 \times 10^{20}$ (c), and 4×10^{20} (d).

sample, where we use the “characteristic” oxygen abundances⁶ from Moustakas et al. (2007), based on only strong nebular lines. Moustakas et al. (2007) show that different “strong-line” methods

⁶The characteristic abundance is intended to be representative of the luminosity-weighted ISM material. For normal spirals, it is taken to be the metallicity at $0.4R_{25}$ (Moustakas et al. 2007). The quoted uncertainties in oxygen abundances do not include systematic uncertainties in the calibrations.

NGC 4594 also has the highest dust-to-metals ratio; even for $X_{\text{CO}} = 4 \times 10^{20} \text{ cm}^{-2} (\text{K km s}^{-1})^{-1}$, $(M_{\text{dust}}/M_{\text{H}})/(\text{O}/\text{H})$ is a factor of ~ 4 above eq. (13). Although this galaxy harbors a massive AGN, the dusty disk and ring are strongly detected at 24, 71, and $160 \mu\text{m}$ (Bendo et al. 2006a). The dust-to-gas ratio estimated for the disk of this galaxy is quite high, $M_{\text{dust}}/M_{\text{H}} = 0.05$; the reason for this high value is not clear. Perhaps the dust properties in this system are significantly different from the Milky Way dust properties that have been assumed in the modeling. Alternatively, perhaps the molecular mass in the dusty ring has been underestimated. The dusty ring has only been observed at a few positions in CO; additional CO observations would be valuable. It is also possible that the ratio of CO luminosity to molecular mass in this galaxy may differ from that in spiral galaxies where the so-called “X factor” has been calibrated. Unfortunately, the dust mass estimate for NGC 4594 is not yet constrained by submm data – while NGC 4594 is strongly detected at $850 \mu\text{m}$, the flux is dominated by the AGN, and the $850 \mu\text{m}$ flux from the dusty disk has not yet been determined (Bendo et al. 2006a). We have seen above (Fig. 12) that dust mass estimates made with and without SCUBA data can differ by factors of ~ 2 . Measurement of the submm continuum emission from the dust ring in NGC 4594 would be of great value.

7.2. Dust-to-Gas Mass Ratios in Low-Metallicity Galaxies

There are many galaxies for which we have only lower limits on the gas mass, because either HI or CO has not been observed. The resulting upper limits on $M_{\text{dust}}/M_{\text{H}}$ are included in Figure 16, which now includes systems with A_{O} as low as 7.54 ± 0.35 (Ho I). For $A_{\text{O}} > 8.1$, upper limits on the global dust-to-gas ratio are generally consistent with eq. (13), to within a factor ~ 2 . However, *every* galaxy in Figure 16 with $A_{\text{O}} < 8.1$ has a global dust-to-gas ratio that falls below eq. (13), sometimes by a very large factor. IC 2574 is low by a factor of 5, and 4 galaxies (Ho II, DDO 053, NGC 5408, NGC 2915) are factors of 8 or more below eq. (13). The most extreme case is NGC 2915, below eq. (13) by a factor of 40. At face value, this might suggest that the balance between dust grain formation and destruction in low-metallicity galaxies such as NGC 2915 is much less favorable to grain formation and survival than in the Milky Way. However, we will argue here that (1) the dust-to-metals ratio in the central regions of these galaxies is in fact normal (i.e., consistent with eq. 13), and (2) the dust-to-metals ratio outside the central regions is not yet known.

Walter et al. (2007) compare the stellar, IR, and H I morphologies of the dwarf irregular (Im) galaxies Ho II, Ho I, IC 2474, and DDO 053: in each of these galaxies, most of the H I is located outside the region where IR emission is detected. For example, only a fraction $f(\text{H I}) \approx 0.19$ of the H I in IC 2574 lies within the regions where 70 and $160 \mu\text{m}$ emission is seen. Similarly, the fraction of the H I within the contours where dust emission is detected is $f(\text{H I}) \approx 0.2, 0.29$, and 0.33 for Ho II, Ho I, and DDO 053.

We have estimated the radii θ_{IR} containing the bulk of the infrared emission for four additional low-metallicity dwarfs: NGC 1705 (Cannon et al. 2006a), NGC 2915, NGC 4236, and NGC 6822 (Cannon et al. 2006b). Our estimates for θ_{IR} , and for the fraction $f(\text{H I})$ of the H I located at

$\theta < \theta_{\text{IR}}$, are given in Table 6, with f ranging from 0.028 (for NGC 2915) to 0.5 (for NGC 4236). The dust-to-gas mass ratios *for the regions where IR emission is detected* are shown in Figure 16. Six of the eight galaxies in Table 6 now have upper limits consistent with (13) to within a factor two, with only two (DDO 053 and NGC 4236) falling low by a factor ~ 2.5 . Given the uncertainties in estimation of both M_{dust} and $f(\text{H I})$, it is entirely possible that $> 50\%$ of the interstellar Mg, Si, and Fe may be in solid grains, at least in systems with $A_{\text{O}} \gtrsim 7.5$.

What can we say about the dust/metals ratio in the extended H I envelopes? Both the metal abundances and the dust masses in these regions are uncertain. The metallicities are estimated using H II regions, and therefore apply only to regions with recent star formation. The outer H I envelopes lack bright H II regions, and therefore the metallicity there is unknown. It would not be surprising if it were substantially lower than the “characteristic” metallicities used in Figure 16. For the outer regions of some spiral galaxies, oxygen has been found to be underabundant, relative to the “characteristic” metallicity of the central regions, by factors of four or more (e.g., Ferguson et al. 1998; Tüllmann et al. 2003).

In the case of NGC 1705, UV absorption line studies show that the H I envelope has $A_{\text{O}} = 7.43 \pm 0.22$ (Heckman et al. 2001): the oxygen abundance in the H I envelope is a factor 6 below the oxygen abundance determined from the H II regions (Moustakas et al. 2007). For this oxygen abundance, $M_{\text{dust}}/M_{\text{H}}$ for NGC 1705 is consistent with eq. (13).

The dust content of the envelope is often also uncertain. The stellar densities in the outer regions of these galaxies are low, and the starlight will be dominated by light coming from the central regions. Table 6 lists $(\nu L_{\nu})_{\text{B}}$, the total stellar luminosity in the B band. For each of these galaxies we give the estimated half-mass radius $\theta_{0.5}$ for the HI, and we have estimated the starlight intensity scale factor U at the H I half-mass radius,

$$U_{0.5} = \frac{1}{(1.982 \times 10^{-13} \text{ ergs cm}^{-3})} \frac{(\nu L_{\nu})_{\text{B}}}{4\pi c (D\theta_{0.5})^2} \quad , \quad (19)$$

where $1.982 \times 10^{-13} \text{ ergs cm}^{-3}$ is $(\nu u_{\nu})_{\text{B}}$ for the local interstellar radiation field (Mathis et al. 1983). Equation (19) neglects internal extinction within the dwarf galaxy [illumination of the outer envelope will suffer the same attenuation as radiation escaping the galaxy, from which $(\nu L_{\nu})_{\text{B}}$ was obtained]. Only one galaxy in Table 6 – the dwarf starburst NGC 1705 – has $U_{0.5} > 0.2$.

The $a \gtrsim 0.03 \mu\text{m}$ grains that normally dominate the $160 \mu\text{m}$ emission are expected to have temperatures $T \approx 17U^{1/6} \text{ K} = 12(U/0.1)^{1/6} \text{ K}$, with peak νp_{ν} at $\lambda \approx hc/6kT \approx 180(0.2/U)^{1/6} \mu\text{m}$. Therefore, for the seven galaxies in Table 6 with $U_{0.5} < 0.2$, even the MIPS $160 \mu\text{m}$ band (with half-response points at 140 and $174 \mu\text{m}$) is relatively insensitive to whatever dust may be present at and beyond $\theta_{0.5}$ except for a small fraction that may be close to local stellar sources. MIPS photometry for these galaxies is dominated by the dust in the luminous regions, and the SED fitting is therefore fitting the parameters for this dust. If there is dust present beyond the half-mass radius, submm observations will be required to detect it in all of the galaxies in Table 6 except NGC 1705.

In the case of SBS 0335-052, where Hunt et al. (2005) report an extraordinarily low dust-to-gas

Table 6. Parameters for Selected Dwarf Galaxies

galaxy	morph type	D Mpc	M_B	$(\nu L_\nu)_B$ L_\odot	θ_{IR} arcmin	$f(\text{H I})$ $\theta < \theta_{\text{IR}}$	$\theta_{0.5}(\text{H I})$ arcmin	$U_{0.5}(\text{H I})$
DDO 053	Im	3.56	-13.44	2.1×10^7	—	0.33 ^a	1	0.11
NGC 6822	Im	0.49	-14.03	3.7×10^7	17	0.33 ^e	33 ^e	0.034
Ho I	Im	3.84	-15.12	1.0×10^8	—	0.29 ^c	2	0.11
NGC 1705	Im	5.10	-15.76	1.8×10^8	0.33 ^g	0.15	0.69 ^f	4.0
NGC 2915	Im	2.70	-16.41	3.3×10^8	0.5	0.028 ^d	4.75 ^a	0.13
Ho II	Im	3.39	-16.69	4.2×10^8	—	0.20 ^c	4	0.15
IC 2574	Sm	4.02	-17.38	8.0×10^8	—	0.19 ^c	6	0.089
NGC 4236	Sdm	4.45	-17.94	1.3×10^9	4.25	~ 0.5	4.2 ^b	0.18

^aBecker et al. (1988)^bEstimated from Rots (1980) map, assuming FWHM=10' gaussian beam.^cWalter et al. (2007)^dEstimated from H I data in Meurer (1997)^eEstimated from H I profile in Cannon et al. (2006b)^fMeurer et al. (1998)^gCannon et al. (2006a)

mass ratio $M_{\text{dust}}/M_{\text{H}} = 1 \times 10^{-7}$, a factor 5000 below eq. (13), we note that this galaxy has not been detected at wavelengths between $100\mu\text{m}$ and 1 cm . The dust models are poorly constrained, and it is possible that they may have significantly underestimated the mass of cool dust. In addition, much of the HI mass in SBS0335-052 may be in an extended envelope, where the metallicity is unknown and where the dust temperatures would be very low. Deep submm observations would be of value to better determine the dust content of SBS 0335-052.

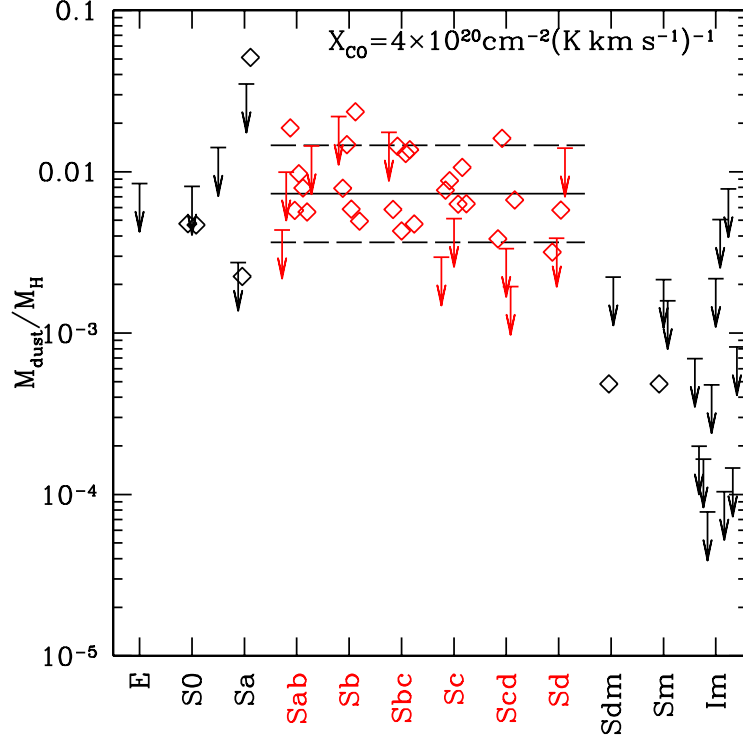


Fig. 17.— Dust-to-gas mass ratio as a function of Hubble type, assuming $X_{\text{CO}} = 4 \times 10^{20} \text{ cm}^{-2} / (\text{K km s}^{-1})$. The horizontal line corresponds to $M_{\text{dust}}/M_{\text{H}} = 0.0073$, and the broken lines to factor-of-two variations around this. Note that the upper bounds are all cases where the dust mass has been estimated, but only lower bounds are available for the gas mass because CO has not yet been observed.

7.3. Dust-to-Gas Mass Ratio and Galaxy Type

The dependence of the dust-to-gas mass ratio on galaxy type is explored in Figure 17. Spiral galaxies (Sab, Sb, Sbc, Sc, Scd, Sd) routinely have $M_{\text{dust}}/M_{\text{H}} \approx 0.007$ to within a factor of two.

We have dust mass estimates for 3 elliptical galaxies (NGC 0855, NGC 3265, and NGC 4125), but lack information on the gas content of NGC 0855 and NGC 4125. Detection of 21cm emission gives a lower bound on the gas mass in NGC 3265. If the molecular and ionized gas mass in

With the existing uncertainties in IRAC calibration and foreground/background subtraction, we do not attempt to estimate q_{PAH} unless

$$[\nu B_\nu(T_\star)]_{7.9\mu\text{m}} \Omega_\star < 0.15 \left(\frac{L_{\text{dust}}}{4\pi D^2} \right) , \quad (21)$$

so that the PAH power in the IRAC $7.9\mu\text{m}$ band would be $>50\%$ of the stellar contribution if $q_{\text{PAH}} = 0.01$. This implies no estimate of q_{PAH} for four galaxies – NGC 1291, NGC 1316, NGC 4125, and NGC 4594 – all galaxies with relatively large bulge/disk ratios. Figure 18 shows the distribution

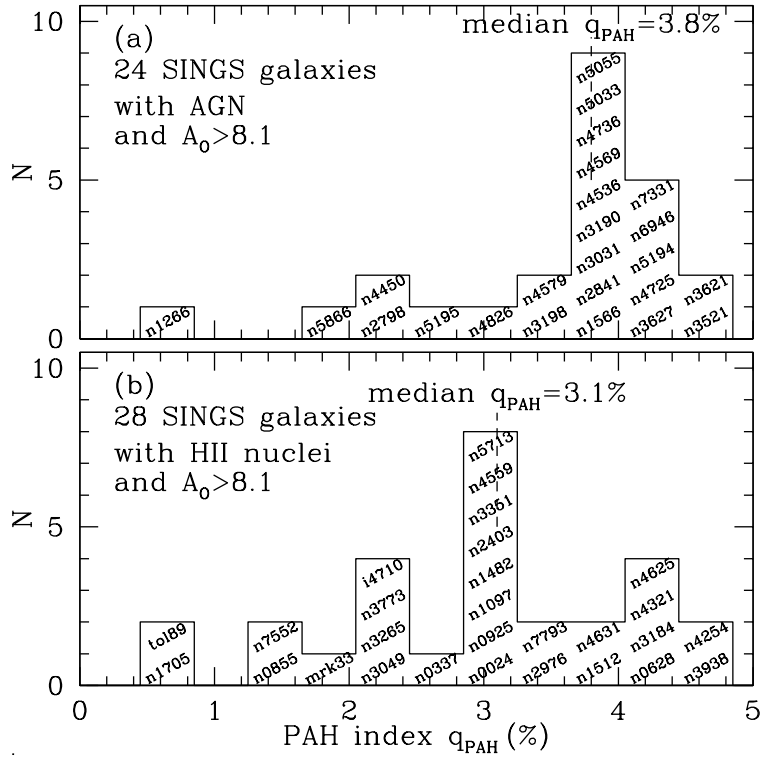


Fig. 19.— Histogram of global q_{PAH} for SINGS galaxies with $A_0 > 8.1$, (a) with, and (b) without an AGN component.

of q_{PAH} for the remaining 61 galaxies for which we have both IRAC and MIPS data. The distribution is broad – 7/61 of the galaxies have $q_{\text{PAH}} < 0.75\%$, while 30/61 of the galaxies have $q_{\text{PAH}} > 3.25\%$.

Roche et al. (1991) noted that the $8\text{--}13\mu\text{m}$ spectra of AGN were often deficient in the PAH emission features commonly seen in H II region galaxies. The spectrum of PAH emission around AGNs has since been found to often exhibit unusual band ratios, with some AGN systems showing extremely low values of $L(7.7\mu\text{m})/L(11.3\mu\text{m})$ (Smith et al. 2007). The suppression of $7.7\mu\text{m}$ emission in AGNs may be attributable to destruction of small PAHs by, e.g., X-rays from the AGN (Voit 1992). Figure 19 shows the distribution of global values of q_{PAH} for SINGS galaxies with

(a) low-luminosity AGN (Seyfert or LINER), or (b) H II nuclei [the AGN/H II nuclear classification is from Moustakas et al. (2007)]. Only galaxies with characteristic metallicities $A_O > 8.1$ are included. The galaxies with AGN tend to have *higher* values of q_{PAH} than the H II galaxies: the global SEDs show no evidence for PAH suppression. This is presumably because the SINGS sample excludes powerful AGN, and low-luminosity AGN have little effect on the global SED. Note that the 5 galaxies in Figure 19b with $q_{\text{PAH}} < 2\%$ include two irregulars (NGC 1705, Mrk 33), one elliptical (NGC 0855), and a dwarf starburst (Tol 89).

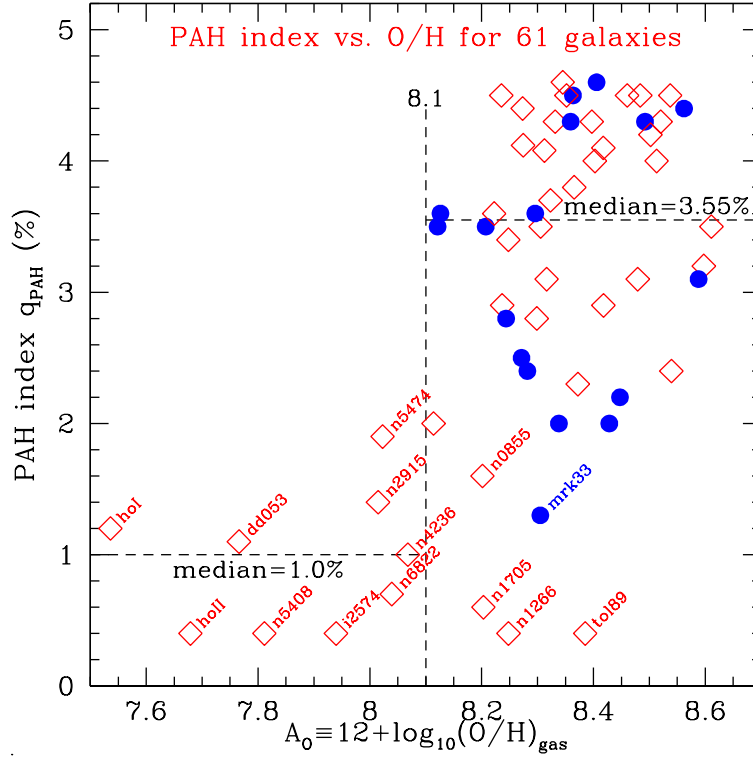


Fig. 20.— PAH index (percentage of dust mass contributed by PAHs with $N_C < 10^3$ C atoms) vs. galaxy metallicity (see text). Low metallicity galaxies always have low PAH index q_{PAH} . Filled circles are SINGS-SCUBA galaxies; diamonds are SINGS galaxies lacking submm data.

Figure 20 shows q_{PAH} versus metallicity for the 61 galaxies in the present study for which q_{PAH} has been determined. We are able to estimate q_{PAH} for galaxies spanning a range of at least 0.9 dex in metallicity, from $A_O = 7.68 \pm 0.03$ (Ho II) to 8.60 ± 0.06 (NGC 3351). [$A_O = 7.54 \pm 0.34$ of Ho I is nominally lower than for Ho II, but is uncertain.] A clear separation is seen: all nine of the galaxies with $A_O < 8.1$ have $q_{\text{PAH}} \leq 1.9\%$, with median $q_{\text{PAH}} = 1.0\%$. When $A_O \gtrsim 8.1$, higher PAH abundances are seen, with median $q_{\text{PAH}} = 3.55\%$ for the 52 galaxies with $A_O > 8.1$, although note that only three of the 52 galaxies with $A_O > 8.1$ have $q_{\text{PAH}} < 1.0\%$ (the median for $A_O < 8.1$). PAH emission strength – as a fraction of total IR emission – therefore appears to always be low for $A_O < 8.1$.

The weakness of PAH emission from low-metallicity galaxies was first noted by Roche et al. (1991) using ground-based spectroscopy, and further investigated with ISO data by Boselli et al. (1998), Sturm et al. (2000), and Madden (2000). The SMC, with $A_O = 8.0$ (Kurt & Dufour 1998; Garnett 1999) falls just below the apparent threshold $A_O = 8.1$ seen in Figure 20. Li & Draine (2002) concluded that the SED of the SMC Bar was consistent with the “SMC” dust model of Weingartner & Draine (2001a), with a PAH index q_{PAH} of only 0.1% ⁷ (see Table 3). ISO observed PAH emission from molecular cloud SMC B1 No. 1 (Reach et al. 2000) outside the SMC bar; Li & Draine showed that the observed emission could be reproduced with a model with only 3% of the SMC carbon in PAHs – corresponding to $q_{\text{PAH}} \approx 0.8\%$. Thus the SMC appears to have $q_{\text{PAH}} < 1\%$.

Hunt et al. (2005) observed PAH emission to be weak in a number of low metallicity blue compact dwarf galaxies. In a photometric study of 34 galaxies spanning two decades in metallicity, Engelbracht et al. (2005) concluded that there was a sharp difference in the ratio of $8\mu\text{m}$ emission from PAHs to $24\mu\text{m}$ emission from warm dust for metallicities above and below a threshold value $A_O \approx 8.2$.⁸ Hogg et al. (2005) compared PAH emission with starlight for a sample of 313 SDSS galaxies, and noted that low-luminosity (presumably low metallicity) star-forming galaxies tended to have low ratios of PAH emission to starlight. Using ISOCAM data, Madden et al. (2006) concluded that PAH abundance, relative to larger grains, was positively correlated with metallicity, and suppressed in systems with hard radiation fields (i.e., high $[\text{Ne III}]/[\text{Ne II}]$ ratio). In a spectroscopic study of blue compact dwarf galaxies, Wu et al. (2006) found that the equivalent width of the PAH 6.2 and $11.2\mu\text{m}$ features appeared to be suppressed for $Z/Z_\odot \lesssim 0.2$, or $A_O \lesssim 7.9$.

The threshold $A_O = 8.1$ found here is close to the value 8.2 found by Engelbracht et al. (2005), and the value 8.0 found by Wu et al. (2006). The reason for the small value of q_{PAH} when $A_O < 8.1$ is not clear at this time. A number of possibilities exist:

- Low A_O might imply more rapid destruction of PAHs by UV radiation in an interstellar medium with reduced shielding by dust.
- Low A_O might imply more effective destruction of PAHs by thermal sputtering in shock-heated gas that cools slowly because of the reduced metallicity.
- Galaxies with low O/H have lower values of C/O (Henry & Worthey 1999); the reduced PAH abundance in these galaxies might be due to a deficiency of PAH-producing carbon stars and C-rich planetary nebulae.

⁷ This result is controversial: for the SMC Bar, Bot et al. (2004) have argued that the PAH abundance as a fraction of the dust mass is similar to the MW value – which we estimate to correspond to $q_{\text{PAH}} \approx 5\%$. Observations of the SMC with *Spitzer* should soon clarify this issue.

⁸Note that the oxygen abundances used by Engelbracht et al. (2005) were based on a heterogeneous compilation of measurements from the literature, whereas the abundances in our study have been derived self-consistently, and placed on a common abundance scale (see Moustakas et al. 2007, in prep., for details)

The distribution of U_{\min} values is shown in Figure 21. The shaded portion of the histogram is contributed by the 17 galaxies for which SCUBA data were available and used in the model-fitting with fixed $U_{\max} = 10^6$; for these galaxies, there was no lower limit imposed on U_{\min} . Two of the 17 galaxies have $U_{\min} = 2.0$, and the other 15 have $U_{\min} \geq 2.5$. The remaining 48 galaxies lack submillimeter data, and for these the restricted fitting procedure allows only $U_{\min} \geq 0.7$. This lower limit on U_{\min} results in a small “pile-up” of five galaxies at $U_{\min} = 0.7$ in Figure 21 – possibly some of these should have smaller values of U_{\min} . What is needed, of course, are submillimeter observations so that the restricted fitting procedure becomes unnecessary.

The form of the starlight distribution function (eq. 6) is based on the expectation that the bulk of the IR luminosity would be radiated by grains in a diffuse interstellar medium with a more-or-less uniform starlight background, with $U \approx U_{\min}$. This assumption appears to be validated by the success of the model in reproducing the observed dust emission extending from $5.7\mu\text{m}$ to $850\mu\text{m}$. It is interesting that the median $U_{\min} = 1.5$ is only slightly more intense than our local interstellar radiation field ($U = 1$), suggesting that interstellar processes (star formation, absorption of starlight by dust) regulate the diffuse starlight intensity to have $U \approx 1.5$ to within a factor of two.

The distribution of mean starlight intensities is shown in Figure 21b. As before, the galaxies with SCUBA data are shaded. The galaxies with SCUBA data and those without SCUBA data both show a tendency to have $\langle U \rangle \approx 2.5$, although about 12% of the sample has $\langle U \rangle > 10$.

The contribution of high intensity regions to the dust heating is shown in Figure 22. In many of the sample galaxies, the observed $24\mu\text{m}$ emission appears to require that a significant fraction of the dust heating take place in regions with high starlight intensities. Figure 22 shows that the median galaxy has $\sim 8\%$ of the total IR power originating from regions with $U > 10^2$, and $\sim 6\%$ of the IR power originating from regions with $U > 10^3$. In most cases these high-intensity regions are probably PDRs bounding dense H II regions. For example, the dust just outside the ionization front in the Orion Bar PDR is heated by starlight with $U \approx 3 \times 10^4$ (Allers et al. 2005), and similar regions should be present in other star-forming galaxies. For steady star formation with the IMF observed in the Milky Way, perhaps $\sim 10\%$ of the bolometric luminosity is contributed by the massive ($M \gtrsim 20M_{\odot}$) stars that tend to spend most of their luminous existences close to their natal clouds, photodissociating and photoionizing the gas, and heating the dust. Therefore the median galaxies in Figure 22 do not seem surprising.

The galaxies with the highest values of $f(U > 10^3)$ are Mrk 33 (Im), Tolo 89 (Im), NGC 5408 (Im), NGC 2798 (Sa), NGC 3049 (Sab), and NGC 7552 (Sab). All of these galaxies appear to be forming stars at a high rate per unit area (see, e.g., discussion of Mrk 33 in §5.6.2), and all have high ratios of $(\nu F_{\nu})_{24\mu\text{m}}/(\nu F_{\nu})_{160\mu\text{m}}$, ranging from 0.52 for Tolo 89 to 1.47 for Mrk 33, indicative of a substantial fraction of the dust power originating in regions where the grains are hot enough to radiate at $24\mu\text{m}$.

DL07 showed that, for their dust models, the fraction of the starlight heating contributed by

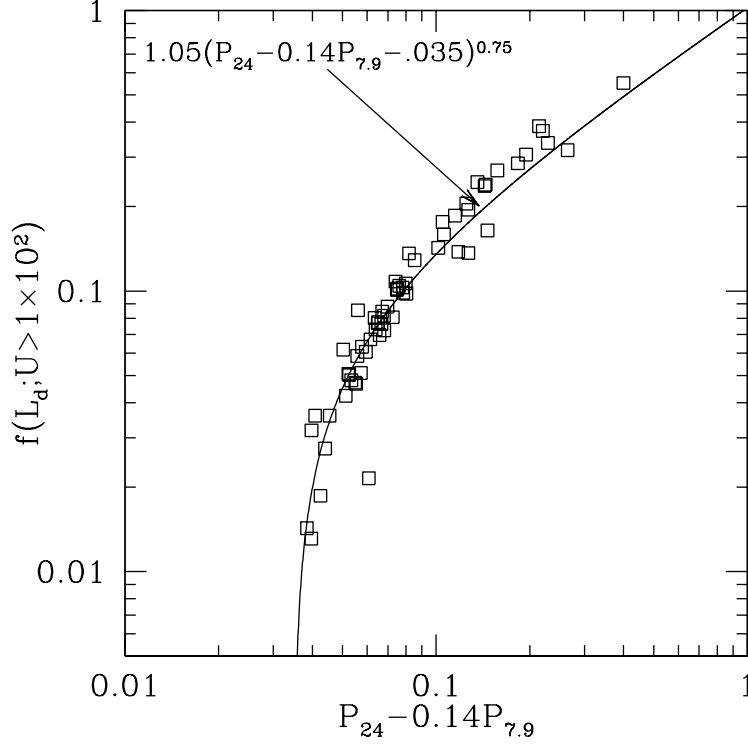


Fig. 23.— Estimated fraction of the dust luminosity contributed by dust in regions with $U > 10^2$ vs. observed value of $P_{24} - 0.14P_{7.9}$ (see text). Also shown is the fitting function proposed by DL07.

9. Discussion

9.1. What About the Dust in Dark Clouds?

The adopted “model” for the distribution of starlight intensities makes no allowance for the possibility of dust in dark clouds, since it assumes that there is no dust heated by starlight intensities below the “diffuse ISM” value U_{\min} . While such dust may not be important as a contributor to the total bolometric luminosity, it would not be surprising if it contained an appreciable fraction of the total dust mass, and it might have been expected to contribute an appreciable fraction of the emission at $850\mu\text{m}$.

However, we have seen that dust with the physical properties adopted by DL07 appears to reproduce the observed SEDs of the 17 SINGS-SCUBA galaxies without a “cold dust” component – indeed, when we fix $U_{\max} = 10^6$, the best-fit models for the 17 SINGS-SCUBA galaxies all have $U_{\min} \geq 2$.

As discussed by DL07, the dust emissivities employed here reproduce the FIR and submm emission from our local diffuse ISM at galactic latitudes $|b| > 7^\circ$ as measured by the FIRAS instru-

ment on COBE (Finkbeiner et al. 1999). To the extent that our models reproduce the observed global FIR and submm emission from other galaxies, it suggests that the dust in dark clouds makes only a minor contribution to the emission. Suppose that a fraction f_{cold} of the dust mass is actually in dark clouds, with dust temperature T_{cold} , and the remainder $(1 - f_{\text{cold}})$ is in diffuse clouds, all at a single dust temperature T_{diff} . Then the fraction p_{cold} of the total emission contributed by the dark cloud dust at wavelength λ is just

$$p_{\text{cold}}(\lambda) = \frac{f_{\text{cold}}/(e^{x_c} - 1)}{f_{\text{cold}}/(e^{x_c} - 1) + (1 - f_{\text{cold}})/(e^{x_d} - 1)} \quad , \quad (24)$$

where $x_c \equiv hc/\lambda k T_{\text{cold}}$ and $x_d \equiv hc/\lambda k T_{\text{diff}}$. If we take $T_{\text{diff}} = 20$ K and $T_{\text{cold}} = 12$ K, for example, then at $850\mu\text{m}$ we have

$$p_{\text{cold}} = \frac{f_{\text{cold}}}{f_{\text{cold}} + 2.33(1 - f_{\text{cold}})} \quad . \quad (25)$$

Hence if, hypothetically, 50% of the dust mass were in the cold clouds ($f_{\text{cold}} = 0.5$), they would contribute only 30% of the total emission at $850\mu\text{m}$; if this hypothetical cold component were left out, the model would fall short at $850\mu\text{m}$ by only 30%, comparable to the existing photometric uncertainties.

Because the model does not include a cold dust component, it would not be surprising if the resulting estimates of the dust mass M_{dust} were low. However, we have seen that if we adopt $X_{\text{CO}} = 4 \times 10^{20} \text{ cm}^{-2} (\text{K km s}^{-1})^{-1}$, we obtain dust-to-gas mass ratios that appear to account for all of the refractory elements in the ISM, as shown in Figure 16. If in fact we have substantially underestimated the dust mass in some of these galaxies, then our adopted gas masses would have to also be increased, by using an even larger value of X_{CO} .

Note that while much of the gas in the Milky Way is molecular, much of this molecular gas is actually in regions with visual extinction $A_V \lesssim 1$, so that it is not “dark”, and the dust grains are heated by diffuse starlight. In dark clouds that are star-forming, such as Orion OMC-1 or M17, much of the dust is actually warm, heated by the embedded stars. It appears most likely that the fraction of the dust mass that is genuinely “cold” is probably relatively small (less than, say, 30%). Although the model omits a “cold dust” component, it appears to recover the majority of the global dust mass in the SINGS galaxies.

9.2. Comparison with Graphical Methods

The model-fitting carried out here has been done by an automated fitting procedure, that includes using interpolated models with values of q_{PAH} intermediate between the seven q_{PAH} values in the Milky Way dust models examined by DL07. DL07 presented a straightforward graphical procedure for estimating q_{PAH} , dust masses and starlight intensities from IRAC and MIPS photometry, and applied it to 5 galaxies as examples. The results of that graphical procedure are compared with the present results in Table 7. For two of the galaxies (Mrk 33 and NGC 3521), the SED model fitting made use of SCUBA data, which is not used in the DL07 graphical procedure.

emission feature near $33\mu\text{m}$, but it is weak,⁹ and narrower than the very broad ($\text{FWHM} \approx 20\mu\text{m}$) peak found in our models. A similar $\sim 1\mu\text{m}$ wide plateau near $33\text{--}34\mu\text{m}$ was also seen in the ISO spectra of bright starburst galaxies (Sturm et al. 2000) and planetary nebulae (Waters et al. 1998), and tentatively attributed to crystalline olivine. If future observations find that the graphite feature is not present with the strength predicted by our model calculations, what would be the implications? First of all, it must be remembered that the present calculations are based on two highly idealized assumptions: (1) the $a > 100 \text{ \AA}$ carbonaceous grains are spherical and composed of single crystals of graphite, and (2) the dielectric tensor in the IR conforms to a simple free-electron model Draine & Lee (1984, 1987). The $33\mu\text{m}$ feature is a consequence of the dielectric function for $\mathbf{E} \parallel c$, which is directly related to the electrical conductivity parallel to the c -axis (i.e., normal to the graphite basal plane). This conductivity is modelled by a free electron gas with a plasma frequency $\omega_p = 1.53 \times 10^{14} \text{ s}^{-1}$, and a damping time $\tau = 1.4 \times 10^{-14} \text{ s}$. The simple free-electron model is not expected to accurately describe the detailed wavelength dependence of this feature (located at $\omega = 2\pi c/33\mu\text{m} = 5.7 \times 10^{13} \text{ s}^{-1}$). Furthermore, even if the model were accurate for ideal graphite, it seems likely that impurities and defects – which might vary from grain to grain in a single region, or from region to region in the galaxy – would have the effect of causing ω_p and τ to vary over the population of emitting grains (and perhaps even within a single grain) resulting in further broadening of this feature. Therefore, failure to observe this feature would probably not rule out graphite as a grain constituent – it would only rule out monocrystalline graphite grains with a dielectric function resembling the simple free-electron model used by Draine & Lee (1984).

Of course, it would not be surprising if the carbonaceous component of the interstellar grain population consisted of something quite different from monocrystalline graphite. “Amorphous carbon”, for instance, refers to a class of materials with widely varying properties: for example, the amorphous carbon materials BE, ACAR, and ACH2 studied by Colangeli et al. (1993, 1995); Mennella et al. (1995) are all insulators, with bandgaps of 0.15 eV, 0.52 eV, and 1.32 eV respectively (Zubko et al. 1996). These carbon solids, each having different properties in the FIR, would not show the $33\mu\text{m}$ feature. It is quite possible that the carbonaceous material in the larger ($a \gtrsim 0.02\mu\text{m}$) interstellar grains may be better approximated by some form of amorphous carbon. However, we have seen that the SINGS photometry appears to also be compatible with graphite.

9.4. The H_2/CO Conversion Factor X_{CO}

To estimate the dust-to-gas mass ratio in §7.1, we need the total hydrogen mass M_{H} , including H_2 . Because H_2 resides primarily in its lowest two rotational states ($J = 0$ and 1), which do not radiate, the $\text{CO } J = 1 \rightarrow 0$ line is routinely employed to trace H_2 . It is usually assumed that the H_2 column density is proportional to the $\text{CO } 1\text{--}0$ surface brightness (see equation 14), with an

⁹ The PAHFIT spectrum decomposition program (Smith et al. 2007) assigns an equivalent width $\sim 0.2\mu\text{m}$ for these galaxies.

empirical conversion factor X_{CO} that is based on some method of estimating the total gas mass. For the Milky Way, virial mass estimates based on giant molecular cloud linewidths give $X_{\text{CO}} = 3.0 \times 10^{20} \text{ cm}^{-2} (\text{K km s}^{-1})^{-1}$ (Young & Scoville 1991). Studies using γ -ray emission as a mass tracer in the Milky Way found $X_{\text{CO}}/[\text{cm}^{-2} (\text{K km s}^{-1})^{-1}] = (1.9 \pm 0.2) \times 10^{20}$ (Strong & Mattox 1996) and $(1.56 \pm 0.05) \times 10^{20}$ (Hunter et al. 1997). Using IR emission from dust as a mass indicator, Dame et al. (2001) found $X_{\text{CO}} = (1.8 \pm 0.3) \times 10^{20} \text{ cm}^{-2} (\text{K km s}^{-1})^{-1}$ for gas at $5^\circ < |b| < 30^\circ$. Because (1) CO 1–0 emission is often optically thick, (2) CO may be subthermally excited in the outer layers of molecular clouds, and (3) photodissociation of CO results in low CO/H₂ ratios in the outer layers of molecular clouds, there is no reason to expect a single value of X_{CO} to apply to all galaxies, or to all regions within a galaxy.

For low-luminosity spiral galaxies in the Virgo cluster, Boselli et al. (2002) estimated values of X_{CO} ranging from $\sim 10^{20} \text{ cm}^{-2} (\text{K km s}^{-1})^{-1}$ for giant spirals to $\sim 10^{21} \text{ cm}^{-2} (\text{K km s}^{-1})^{-1}$ for dwarf irregulars. Based on an extensive study of giant molecular clouds in a number of galaxies in the Local Group, Blitz et al. (2006) conclude that $X_{\text{CO}} = 4 \times 10^{20} \text{ cm}^{-2} (\text{K km s}^{-1})^{-1}$ is a good value to use for most galaxies if the individual GMCs are assumed to be virialized.

The present study has demonstrated that we can use a physical dust model to reproduce observed IR and FIR emission from nearby galaxies, allowing us to estimate the dust mass in these galaxies. Because we have a-priori expectations for the value of the dust-to-gas mass ratio, our determination of M_{dust} therefore allows us to estimate the total gas mass, and thereby estimate X_{CO} for these galaxies.

Figure 15 explores the relationship between dust-to-gas mass ratio and metallicity. Observed values of $M_{\text{dust}}/M_{\text{H}}$ are plotted versus metallicity in Figures 15a and b, showing only galaxies where both H I and CO have been detected, or where the upper limit on either H I or CO shows it to be of minor importance compared to the other gas component. Equation (13) is plotted in Figure 15a,b, where we assume $[A_{\text{O}}]_{\text{MW}} = 8.59$. The figure includes 12 galaxies for which SCUBA data constrains the dust models – these should be the most reliable dust masses. The figure includes an additional 20 galaxies lacking submm data. In Figure 15a the H₂ mass is estimated using $X_{\text{CO}} = 2 \times 10^{20} \text{ cm}^{-2} (\text{K km s}^{-1})^{-1}$, whereas Figure 15b uses $X_{\text{CO}} = 4 \times 10^{20} \text{ cm}^{-2} (\text{K km s}^{-1})^{-1}$.

From comparison of Figures 15a and b, we see that $X_{\text{CO}} = 4 \times 10^{20} \text{ cm}^{-2} (\text{K km s}^{-1})^{-1}$ results in dust-to-gas mass ratios for the SINGS-SCUBA galaxies that are consistent with the amount of material actually available to form silicate and carbonaceous grains, when one considers that the dust mass estimates are uncertain at the factor-of-two level, and the metallicity estimates are also uncertain. There are some cases with mass determinations (not upper limits) that fall well above eq. (13), which was expected to define an upper envelope for $M_{\text{dust}}/M_{\text{H}}$. For all cases where submm data were used in the fitting, the dust mass estimates were expected to have better than factor of two accuracy; if we adopt $X_{\text{CO}} = 4 \times 10^{20} \text{ cm}^{-2} (\text{K km s}^{-1})^{-1}$, none of the galaxies with SCUBA data exceed eq. (13) by more than a factor 2. Conversely, $X_{\text{CO}} = 2 \times 10^{20} \text{ cm}^{-2} (\text{K km s}^{-1})^{-1}$ would imply dust masses for NGC 1482 and NGC 2976 that would be uncomfortably large given their

estimated oxygen abundances. The one galaxy in Figure 15b that falls well above the expected envelope is NGC 4594, the Sombrero galaxy. The interstellar medium in this unusual system merits further study.

The histograms in Figures 15c,d show the distribution of the dust-to-gas mass ratio, normalized to the characteristic oxygen abundance of the Milky Way. Ideally, the distribution would be narrow and peaking at ~ 0.01 , possibly with a tail to low values of $(M_{\text{dust}}/M_{\text{H}})/[(\text{O}/\text{H})/(\text{O}/\text{H})_{\text{MW}}]$ representing galaxies where the grains do not incorporate a large fraction of the refractory elements. For $X_{\text{CO}} = 2 \times 10^{20} \text{ cm}^{-2} (\text{K km s}^{-1})^{-1}$, the median is at 0.016. For $X_{\text{CO}} = 4 \times 10^{20} \text{ cm}^{-2} (\text{K km s}^{-1})^{-1}$, the median shifts to 0.012 – approximately the value expected if grains incorporate most of the refractory elements (as is the case in the Milky Way).

The above considerations suggest that the value $X_{\text{CO}} \approx 4 \times 10^{20} \text{ cm}^{-2} (\text{K km s}^{-1})^{-1}$ recommended by Blitz et al. (2006) for Local Group galaxies is also appropriate for the SINGS galaxy sample. This value of X_{CO} is a factor of ~ 2 larger than the value $(1.8 \pm 0.3) \times 10^{20} \text{ cm}^{-2} (\text{K km s}^{-1})^{-1}$ found recently by Dame et al. (2001) for the local Milky Way.

10. Summary

The principal results of this paper are as follows:

1. A physical dust model consisting of PAHs, carbonaceous grains, and amorphous silicate grains (Draine & Li 2007) heated by starlight, with a distribution of starlight intensities, successfully reproduces the IR and submm emission for a sample of 17 galaxies with IRAC and MIPS photometry plus SCUBA photometry. In particular, the SCUBA photometry does *not* require an additional population of cold dust grains, or grains with enhanced submm emissivities. Cold dust grains in dark clouds appear to contain only a minor fraction ($\lesssim 50\%$) of the total dust mass.
2. The dust model allows the mean starlight intensity scale factor $\langle U \rangle$ and the total dust mass M_{dust} to be estimated for each galaxy. For the 17 galaxies with SCUBA data, $\langle U \rangle$ ranges from 2.2 to 16, with a median of 4.3 (see Fig. 7). For the 12 galaxies with SCUBA data and CO and H I observations, and assuming $X_{\text{CO}} = 4 \times 10^{20} \text{ cm}^{-2} (\text{K km s}^{-1})^{-1}$, the median $M_{\text{dust}}/M_{\text{H}} = 0.0052$ (see Fig. 4) – this is similar to $M_{\text{dust}}/M_{\text{H}} \approx 0.0073$ estimated for the Milky Way based on observed depletions (see Table 2), or the value ~ 0.010 estimated from dust models that reproduce the observed Milky Way extinction (see Table 3).
3. When submm observations are unavailable, the mass of cool dust in a galaxy is poorly constrained. However, we use the model fits for the 17 galaxies where SCUBA data are available to test a “restricted” fitting procedure that can be applied when submm observations are unavailable. For the 17 galaxies where global SCUBA data are available, the restricted fitting procedure recovered the dust mass to within a factor 1.5 in 11/17 cases (see Fig. 12), and to

within a factor 2.2 in every case. This restricted fitting procedure can therefore be used to estimate dust masses and starlight intensities in galaxies with dust emission detected in the three MIPS bands.

4. For the 20 galaxies which lack SCUBA fluxes but for which the gas mass is known, the median $M_{\text{dust}}/M_{\text{H}} \approx 0.0088$ (see Fig. 14).
5. By comparing dust-to-gas mass ratios computed with different assumed values of the CO to molecular mass conversion factor X_{CO} , we find that the dust-to-gas mass ratio normalized to galaxy metallicity gives dust masses consistent with available metal abundances for $X_{\text{CO}} \approx 4 \times 10^{20} \text{ cm}^{-2} (\text{K km s}^{-1})^{-1}$ (see Fig. 15).
6. All 49 galaxies in Figure 16 with $A_{\text{O}} > 8.2$ appear to have dust masses consistent (to within a factor ~ 3) with eq. (13), corresponding to the total mass of dust in the WD01 models for Milky Way dust (see Table 3) scaled by metallicity. This is close to the mass that will be formed if silicates are formed from the bulk of the interstellar Mg, Si, and Fe, and $\sim 50\%$ of the interstellar carbon goes into carbonaceous grains (see Table 2).

All 9 of the galaxies in Fig. 16 with metallicities $A_{\text{O}} < 8.1$ appear to have *global* dust-to-gas ratios that fall below eq. (13), in some cases by large factors: NGC 2915 appears to be at least a factor 40 below eq. (13). However, the dust-to-gas ratio *in the regions where dust emission is detected* appears to be close to eq. (13). The low apparent global dust-to-gas ratios are found in dwarf galaxies with extended H I envelopes. When allowance is made for the lower metallicity and lower starlight intensity in the envelopes, it appears that the dust-to-gas mass ratios may be consistent with eq. (13).

7. We characterize the PAH abundance by a quantitative “PAH index” q_{PAH} , defined to be the fraction of the total dust mass contributed by PAHs containing less than 10^3 C atoms. The 61 galaxies in this sample for which we are able to estimate q_{PAH} span the range of PAH index from 0.4 to 4.7%, with a median $q_{\text{PAH}} = 3.4\%$ (see Fig. 18).
8. The PAH index q_{PAH} is strongly correlated with metallicity (see Fig. 20). The nine galaxies with $A_{\text{O}} < 8.1$ have $q_{\text{PAH}} \leq 2\%$, and median $q_{\text{PAH}} = 1.0\%$, whereas the 52 galaxies with $A_{\text{O}} > 8.1$ have median $q_{\text{PAH}} = 3.55\%$. Metallicity $A_{\text{O}} = 8.1$ appears to mark a transition in the composition of interstellar dust in galaxies, from low-PAH to high-PAH. Possible reasons for the observed variation in q_{PAH} are discussed in §7.4.
9. Except for three starbursting galaxies (Mrk 33, Tolo 89, NGC 3049), the infrared emission from dust is dominated by dust grains exposed to starlight intensities $U \approx U_{\text{min}}$, interpreted here as dust in diffuse regions heated by the general diffuse starlight background (see Fig. 22a). Half of the galaxies have more than 88% of the total dust power provided by this component.
10. The SEDs for the star-forming galaxies in the sample require that a significant fraction of the dust luminosity be produced by warm dust in regions of intense starlight. Half of the

galaxies in the sample have more than 8% of the total dust luminosity originating in regions with $U > 10^2$ (see Fig. 22). This appears to be consistent with the expected heating of dust in PDRs near massive stars.

We thank S. Madden and the anonymous referee for helpful comments. Support for this work, part of the *Spitzer Space Telescope* Legacy Science Program, was provided by NASA through the Jet Propulsion Laboratory under NASA contract 1407. BTB was supported in part by NSF grant AST-0406883.

BTB is grateful to R.H. Lupton for availability of the SM graphics program.

REFERENCES

- Ajhar, E. A., Lauer, T. R., Tonry, J. L., Blakeslee, J. P., Dressler, A., Holtzman, J. A., & Postman, M. 1997, *AJ*, 114, 626
- Allers, K. N., Jaffe, D. T., Lacy, J. H., Draine, B. T., & Richter, M. J. 2005, *ApJ*, 630, 368
- Bajaja, E., Krause, M., Wielebinski, R., & Dettmar, R.-J. 1991, *A&A*, 241, 411
- Bakes, E. L. O., & Tielens, A. G. G. M. 1994, *ApJ*, 427, 822
- Becker, R., Mebold, U., Reif, K., & van Woerden, H. 1988, *A&A*, 203, 21
- Bendo, G., et al. 2006a, *ApJ*, 645, 134
- Bendo, G. J., et al. 2006b, *ApJ*, 652, 283
- Blitz, L., Fukui, Y., Kawamura, A., Leroy, A., Mizuno, N., & Rosolowsky, E. 2006, *astro-ph/0602600*
- Boselli, A., Lequeux, J., & Gavazzi, G. 2002, *A&A*, 384, 33
- Boselli, A., et al. 1998, *A&A*, 335, 53
- Bot, C., Boulanger, F., Lagache, G., Cambr sy, L., & Egret, D. 2004, *A&A*, 423, 567
- Boulanger, F., & Viallefond, F. 1992, *A&A*, 266, 37
- Cannon, J. M., et al. 2006a, *ApJ*, 647, 293
- . 2006b, *ApJ*, 652, 1170
- . 2005, *ApJ*, 630, L37
- Cartledge, S. I. B., Lauroesch, J. T., Meyer, D. M., & Sofia, U. J. 2004, *ApJ*, 613, 1037

- Colangeli, L., Mennella, V., Blanco, A., Fonti, S., Bussoletti, E., Gumlich, H. E., Mertins, H. C., & Jung, C. 1993, *ApJ*, 418, 435
- Colangeli, L., Mennella, V., Palumbo, P., Rotundi, A., & Bussoletti, E. 1995, *A&AS*, 113, 561
- Dale, D. A., et al. 2005, *ApJ*, 633, 857
- . 2007, *ApJ*, accepted, 000, 000
- Dale, D. A., Helou, G., Contursi, A., Silbermann, N. A., & Kolhatkar, S. 2001, *ApJ*, 549, 215
- Dame, T. M., Hartmann, D., & Thaddeus, P. 2001, *ApJ*, 547, 792
- Draine, B. T. 2003, *ARA&A*, 41, 241
- Draine, B. T., & Lee, H. M. 1984, *ApJ*, 285, 89
- . 1987, *ApJ*, 318, 485
- Draine, B. T., & Li, A. 2001, *ApJ*, 551, 807
- . 2007, *ApJ*, 657, 810
- Dumke, M., Krause, M., & Wielebinski, R. 2004, *A&A*, 414, 475
- Dwek, E. 1998, *ApJ*, 501, 643
- Edmunds, M. G. 2001, *MNRAS*, 328, 223
- Engelbracht, C. W., Gordon, K. D., Rieke, G. H., Werner, M. W., Dale, D. A., & Latter, W. B. 2005, *ApJ*, 628, L29
- Fazio, G. G., et al. 2004, *ApJS*, 154, 10
- Ferguson, A. M. N., Gallagher, J. S., & Wyse, R. F. G. 1998, *AJ*, 116, 673
- Finkbeiner, D. P., Davis, M., & Schlegel, D. J. 1999, *ApJ*, 524, 867
- Ford, H. C., Hui, X., Ciardullo, R., Jacoby, G. H., & Freeman, K. C. 1996, *ApJ*, 458, 455
- Förster Schreiber, N. M., Roussel, H., Sauvage, M., & Charmandaris, V. 2004, *A&A*, 419, 501
- Freedman, W. L., et al. 2001, *ApJ*, 553, 47
- Galliano, F., Madden, S. C., Jones, A. P., Wilson, C. D., & Bernard, J.-P. 2005, *A&A*, 434, 867
- Galliano, F., Madden, S. C., Jones, A. P., Wilson, C. D., Bernard, J.-P., & Le Peintre, F. 2003, *A&A*, 407, 159

- Garnett, D. R. 1999, in IAU Symp. 190: New Views of the Magellanic Clouds, ed. Y.-H. Chu, N. Suntzeff, J. Hesser, & D. Bohlender, 266–272
- Grevesse, N., & Sauval, A. J. 1998, *Space Science Reviews*, 85, 161
- Habing, H. J. 1968, *Bull. Astron. Inst. Netherlands*, 19, 421
- Heckman, T. M., Sembach, K. R., Meurer, G. R., Strickland, D. K., Martin, C. L., Calzetti, D., & Leitherer, C. 2001, *ApJ*, 554, 1021
- Helou, G., et al. 2004, *ApJS*, 154, 253
- Henry, R. B. C., & Worthey, G. 1999, *PASP*, 111, 919
- Hirashita, H., Tajiri, Y. Y., & Kamaya, H. 2002, *A&A*, 388, 439
- Hogg, D. W., Tremonti, C. A., Blanton, M. R., Finkbeiner, D. P., Padmanabhan, N., Quintero, A. D., Schlegel, D. J., & Wherry, N. 2005, *ApJ*, 624, 162
- Hony, S., Van Kerckhoven, C., Peeters, E., Tielens, A. G. G. M., Hudgins, D. M., & Allamandola, L. J. 2001, *A&A*, 370, 1030
- Hunt, L., Bianchi, S., & Maiolino, R. 2005, *A&A*, 434, 849
- Hunter, S. D., et al. 1997, *ApJ*, 481, 205
- Izotov, Y. I., & Thuan, T. X. 1998, *ApJ*, 500, 188
- James, A., Dunne, L., Eales, S., & Edmunds, M. G. 2002, *MNRAS*, 335, 753
- Jenkins, E. B. 2004, in *Origin and Evolution of the Elements*, ed. A. McWilliam & M. Rauch, 336–353
- Karachentsev, I. D., et al. 2002a, *A&A*, 383, 125
- . 2002b, *A&A*, 385, 21
- Kennicutt, R. C., et al. 2003, *PASP*, 115, 928
- Kobulnicky, H. A., & Kewley, L. J. 2004, *ApJ*, 617, 240
- Krugel, E., Siebenmorgen, R., Zota, V., & Chini, R. 1998, *A&A*, 331, L9
- Kurt, C. M., & Dufour, R. J. 1998, in *Revista Mexicana de Astronomia y Astrofisica Conference Series*, 202–206
- Leroy, A., Bolatto, A. D., Simon, J. D., & Blitz, L. 2005, *ApJ*, 625, 763
- Li, A., & Draine, B. T. 2001, *ApJ*, 554, 778

- . 2002, *ApJ*, 576, 762
- Lisenfeld, U., & Ferrara, A. 1998, *ApJ*, 496, 145
- Madden, S. C. 2000, *New Astronomy Review*, 44, 249
- Madden, S. C., Galliano, F., Jones, A. P., & Sauvage, M. 2006, *A&A*, 446, 877
- Marconi, A., Testi, L., Natta, A., & Walmsley, C. M. 1998, *A&A*, 330, 696
- Mathis, J. S., Mezger, P. G., & Panagia, N. 1983, *A&A*, 128, 212
- Mennella, V., Colangeli, L., Blanco, A., Bussoletti, E., Fonti, S., Palumbo, P., & Mertins, H. C. 1995, *ApJ*, 444, 288
- Meurer, G. R. 1997, *Publications of the Astronomical Society of Australia*, 14, 77
- Meurer, G. R., Staveley-Smith, L., & Killeen, N. E. B. 1998, *MNRAS*, 300, 705
- Moustakas, J., Kennicutt, R. C., & coauthors. 2007, in preparation
- Pagani, L., Lequeux, J., Cesarsky, D., Donas, J., Milliard, B., Loinard, L., & Sauvage, M. 1999, *A&A*, 351, 447
- Pilyugin, L. S., & Thuan, T. X. 2005, *ApJ*, 631, 231
- Reach, W. T., Boulanger, F., Contursi, A., & Lequeux, J. 2000, *A&A*, 361, 895
- Reach, W. T., et al. 2005, *PASP*, 117, 978
- Rieke, G. H., et al. 2004, *ApJS*, 154, 25
- Roberts, M. S., Hogg, D. E., Bregman, J. N., Forman, W. R., & Jones, C. 1991, *ApJS*, 75, 751
- Roche, P. F., Aitken, D. K., Smith, C. H., & Ward, M. J. 1991, *MNRAS*, 248, 606
- Rots, A. H. 1980, *A&AS*, 41, 189
- Roussel, H., et al. 2006, *ApJ*, 646, 841
- Savage, B. D., & Sembach, K. R. 1996, *ARA&A*, 34, 279
- Sheth, K., Vogel, S. N., Regan, M. W., Thornley, M. D., & Teuben, P. J. 2005, *ApJ*, 632, 217
- Smith, J. D. T., et al. 2007, *ApJ*, 656, 770
- Strong, A. W., & Mattox, J. R. 1996, *A&A*, 308, L21
- Sturm, E., Lutz, D., Tran, D., Feuchtgruber, H., Genzel, R., Kunze, D., Moorwood, A. F. M., & Thornley, M. D. 2000, *A&A*, 358, 481

- Tosi, M., Sabbi, E., Bellazzini, M., Aloisi, A., Greggio, L., Leitherer, C., & Montegriffo, P. 2001, *AJ*, 122, 1271
- Tuffs, R. J., Popescu, C. C., Völk, H. J., Kylafis, N. D., & Dopita, M. A. 2004, *A&A*, 419, 821
- Tüllmann, R., Rosa, M. R., Elwert, T., Bomans, D. J., Ferguson, A. M. N., & Dettmar, R.-J. 2003, *A&A*, 412, 69
- Voit, G. M. 1992, *MNRAS*, 258, 841
- Walter, F. 2005, private communication, 000, 000
- Walter, F., et al. 2007, submitted to *ApJ*, 000, 000
- Waters, L. B. F. M., et al. 1998, *A&A*, 331, L61
- Weingartner, J. C., & Draine, B. T. 2001a, *ApJ*, 548, 296
- . 2001b, *ApJS*, 134, 263
- Werner, M. W., et al. 2004, *ApJS*, 154, 1
- Whittet, D. C. B., Bode, M. F., Longmore, A. J., Adamson, A. J., McFadzean, A. D., Aitken, D. K., & Roche, P. F. 1988, *MNRAS*, 233, 321
- Wu, Y., Charmandaris, V., Hao, L., Brandl, B. R., Bernard-Salas, J., Spoon, H. W. W., & Houck, J. R. 2006, *ApJ*, 639, 157
- Young, J. S., & Scoville, N. Z. 1991, *ARA&A*, 29, 581
- Zubko, V. G., Mennella, V., Colangeli, L., & Bussoletti, E. 1996, *MNRAS*, 282, 1321

A. Spectral Energy Distributions for 48 Galaxies Lacking Submm Data

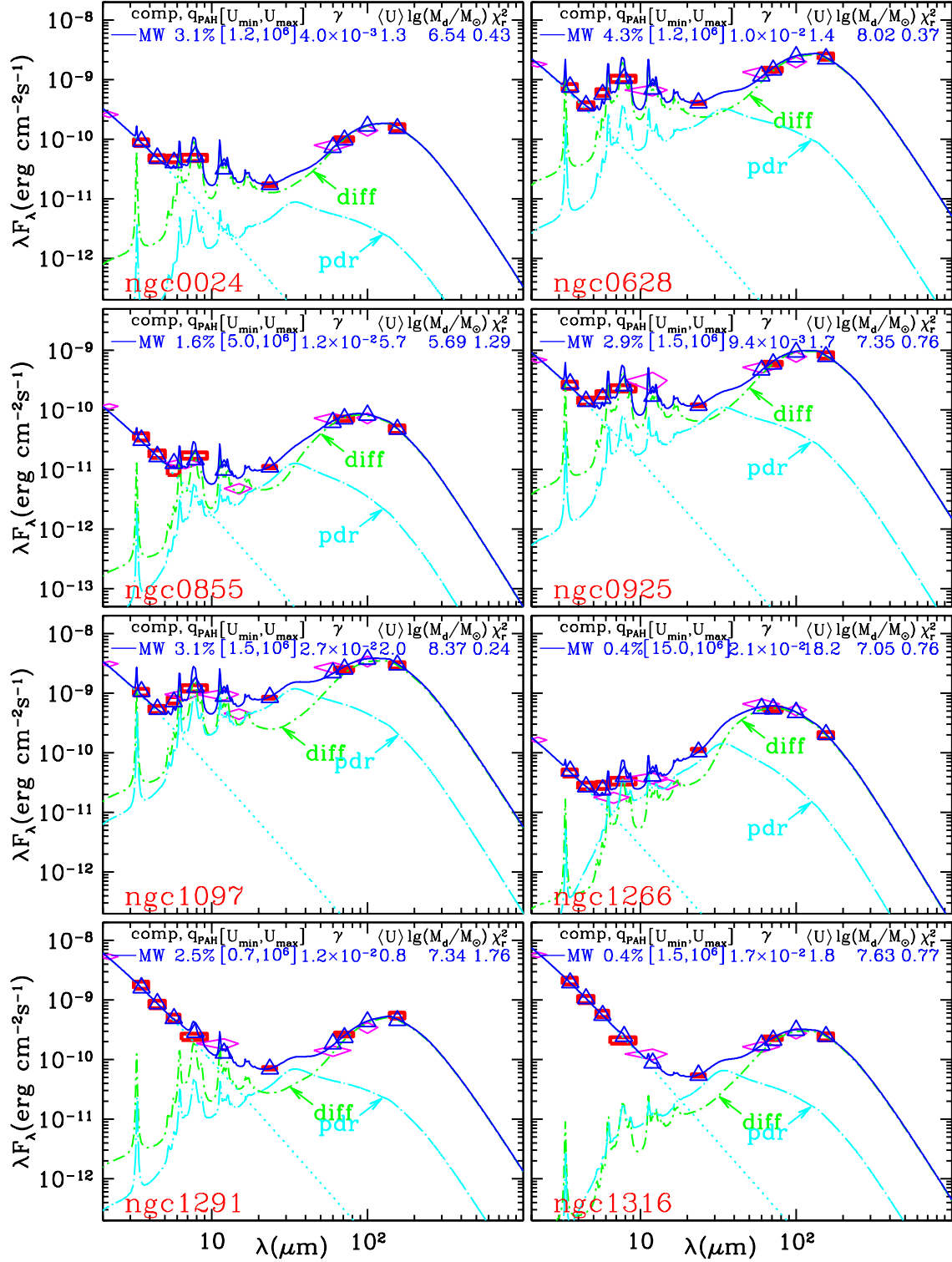


Fig. 24.— Same as Fig. 11, but for galaxies with only IRAC, MIPS, and IRAS data.

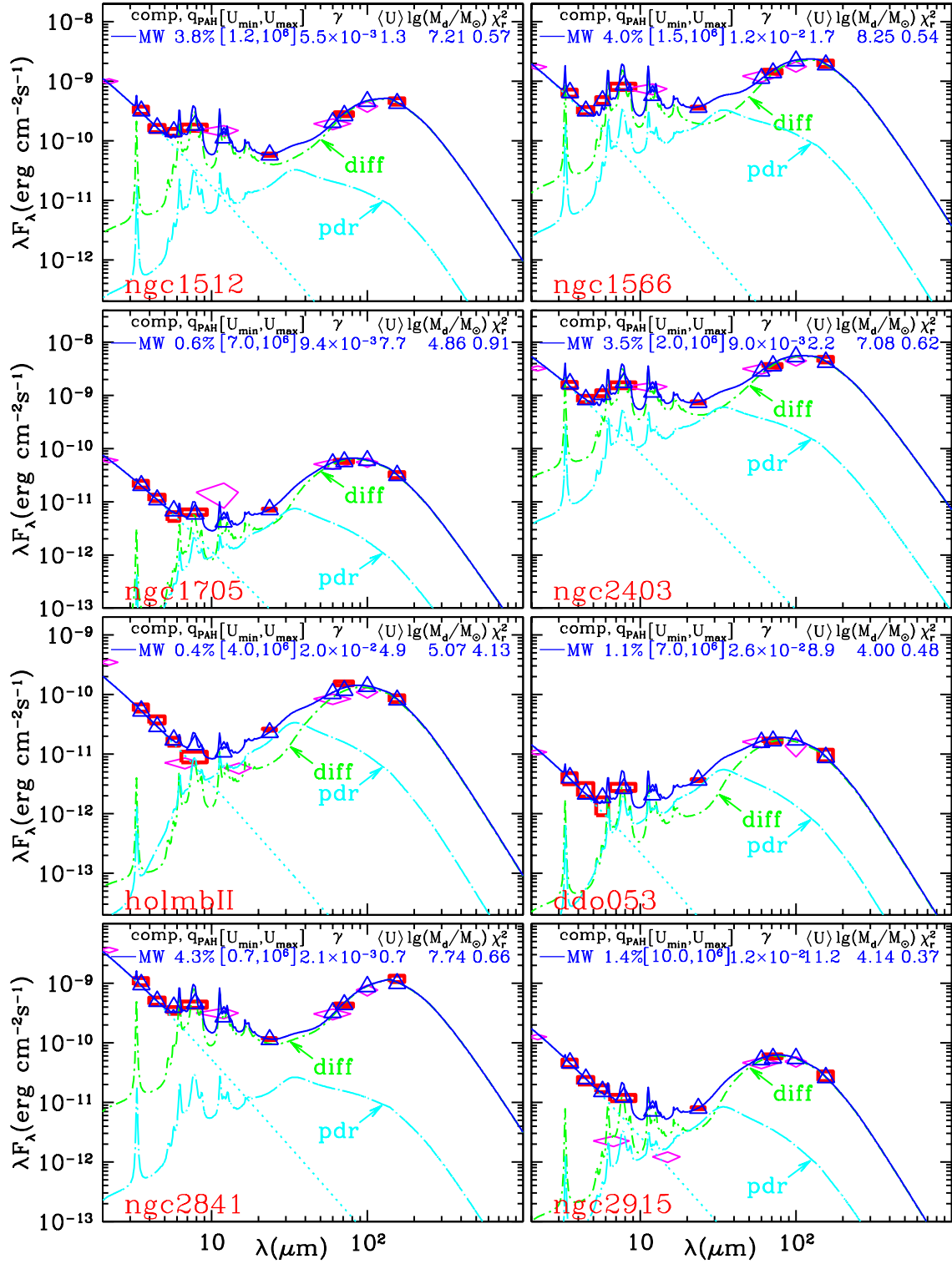


Fig. 24, continued.

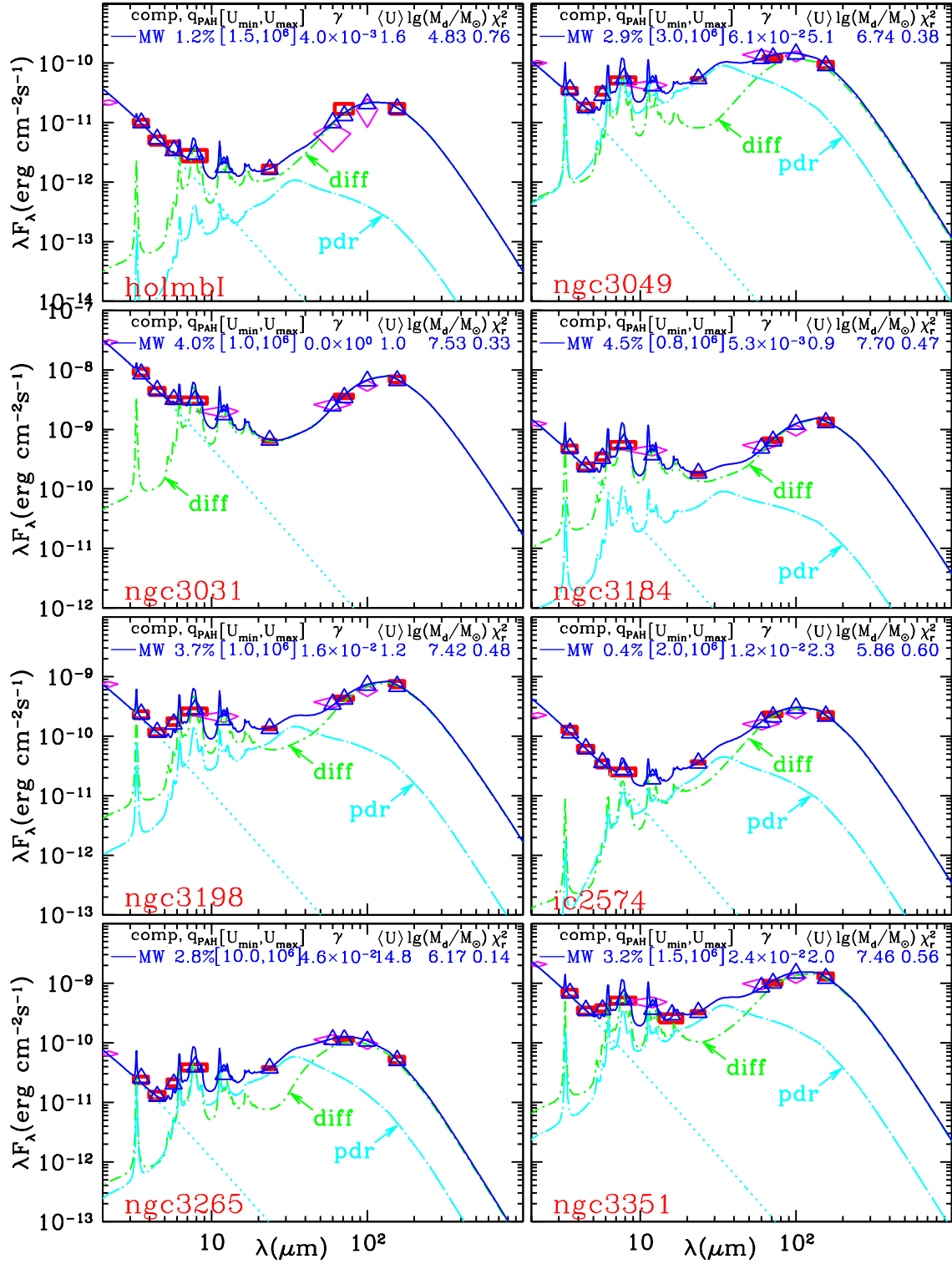


Fig. 24, continued.

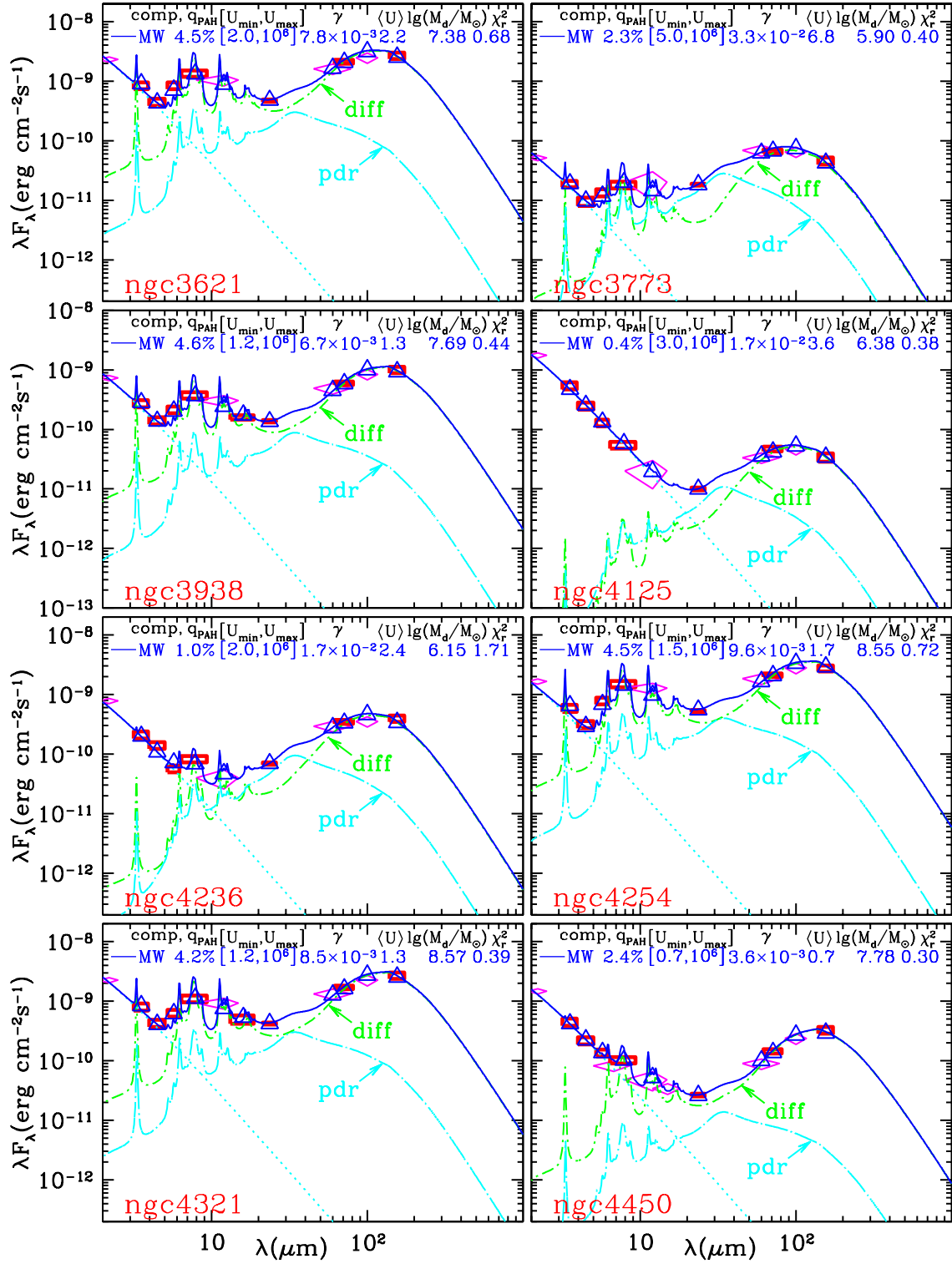


Fig. 24, continued.

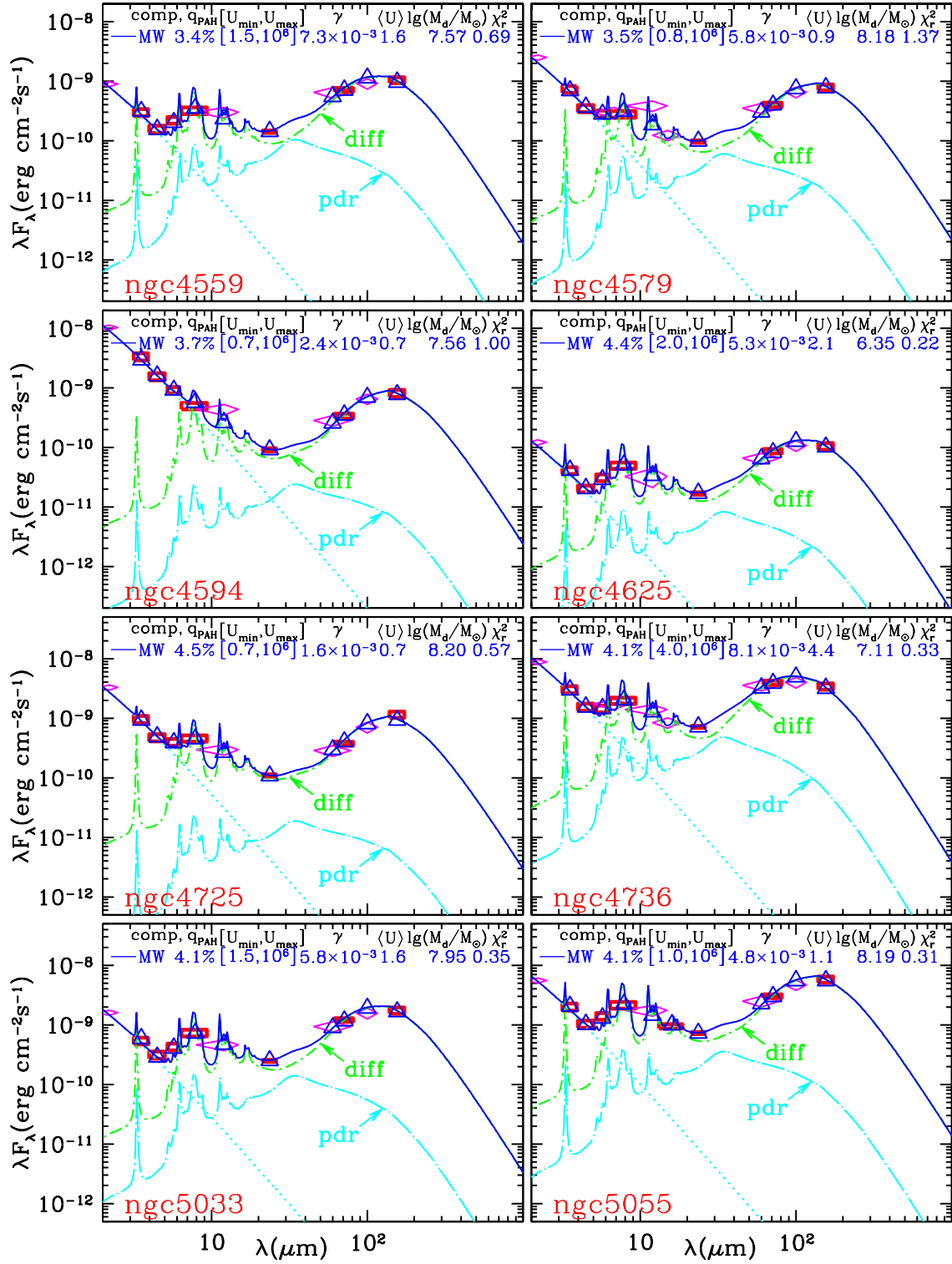


Fig. 24, continued.

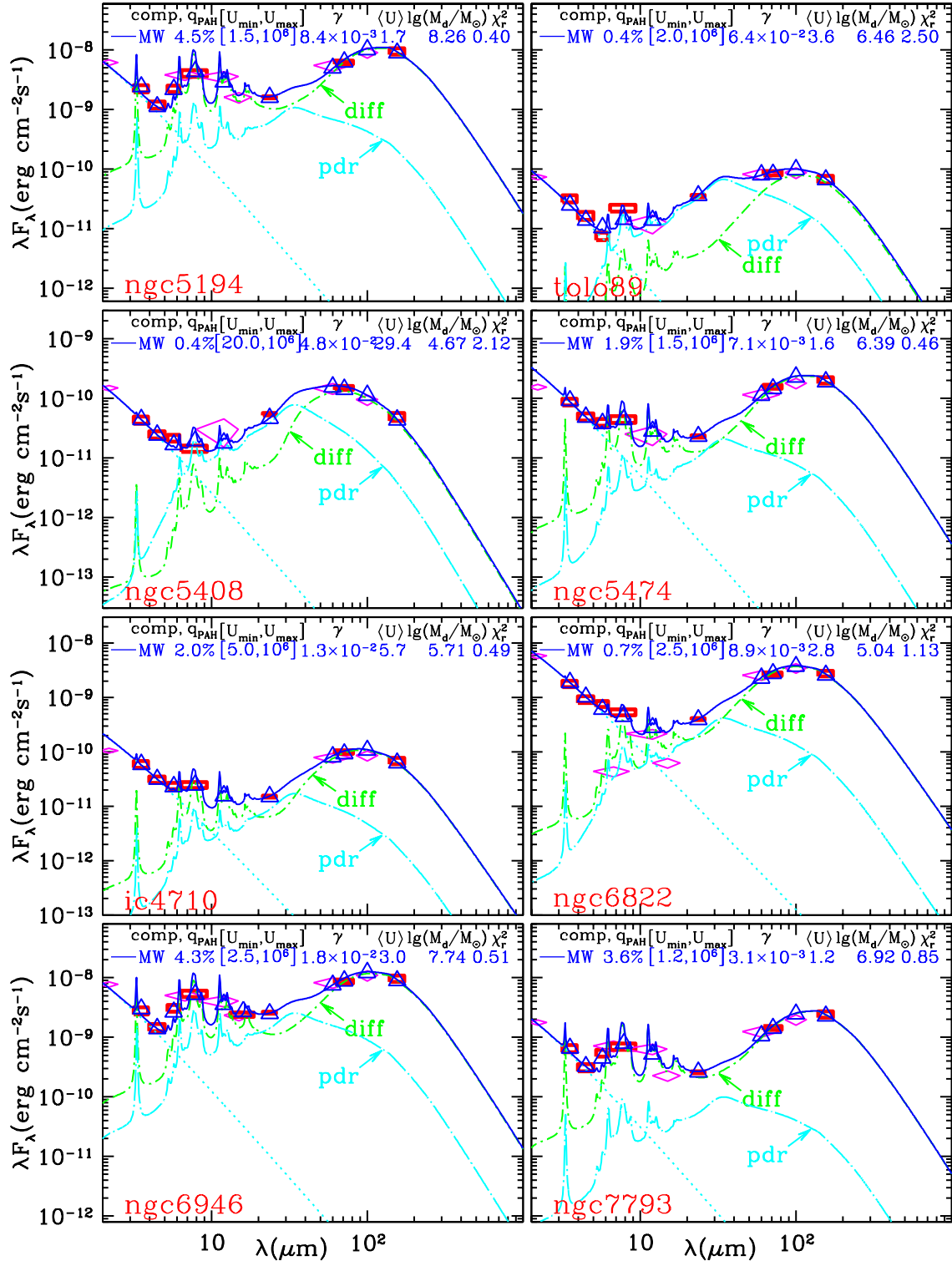


Fig. 24, continued.